Heavy Metal Ion Sensing in Water via Transition Metal Dichalcogenide Functionalized Oxide High Electron Mobility Transistor

Ph.D. Thesis

By
SUMIT CHAUDHARY

DEPARTMENT OF ELECTRICAL ENGINEERING
INDIAN INSTITUTE OF TECHNOLOGY INDORE
DECEMBER 2024

Heavy Metal Ion Sensing in Water via Transition Metal Dichalcogenide Functionalized Oxide High Electron Mobility Transistor

A THESIS

Submitted in partial fulfillment of the
requirements for the award of the degree

of
DOCTOR OF PHILOSOPHY

by
SUMIT CHAUDHARY

DEPARTMENT OF ELECTRICAL ENGINEERING
INDIAN INSTITUTE OF TECHNOLOGY INDORE
DECEMBER 2024

INDIAN INSTITUTE OF TECHNOLOGY INDORE

CANDIDATE'S DECLARATION

I hereby certify that the work which is being presented in the thesis entitled **"Heavy Metal Ion Sensing in Water via Transition Metal Dichalcogenide Functionalized Oxide High Electron Mobility Transistor"** in the partial fulfilment of the requirements for the award of the degree of **Doctor of Philosophy** and submitted in the **Department of Electrical Engineering, Indian Institute of Technology Indore**, is an authentic record of my own work carried out during the time period from **December, 2019** to **December, 2024** under the supervision of **Prof. Shaibal Mukherjee**, Professor, Electrical Engineering, IIT Indore.

The matter presented in this thesis has not been submitted by me for the award of any other degree of this or any other institute.

Sumit.
16/05/2025

Signature of the student with date

SUMIT CHAUDHARY

This is to certify that the above statement made by the candidate is correct to the best of my knowledge.

S. Mukherjee 16/5/2025

Signature of Thesis Supervisor with Date

PROF. SHAIBAL MUKHERJEE

Mr. Sumit Chaudhary has successfully given his Ph.D. Oral Examination held on 13/05/2025.

S. Mukherjee 16/5/2025

Signature of Thesis Supervisor with date

PROF. SHAIBAL MUKHERJEE

ACKNOWLEDGEMENTS

First and foremost, I would like to express my heartfelt gratitude to my thesis supervisor, **Prof. Shaibal Mukherjee**, Department of Electrical Engineering, IIT Indore. Your encouragement during challenging times and your invaluable expertise have not only shaped this research but have also profoundly influenced my growth as a scholar. Thank you for your patience, mentorship, and for inspiring me to strive for excellence throughout this endeavor.

I extend my heartfelt gratitude to my doctoral committee members, **Prof. Mukesh Kumar** and **Dr. Srimanta Pakhira**, for their invaluable advice, and insightful feedback. Your support throughout this journey has been absolutely invaluable, and your encouragement has continually inspired and guided my research at every stage.

I sincerely thank **Prof. Suhas S. Joshi**, Director of IIT Indore, for providing the essential infrastructure and research facilities that were pivotal to this work. I also want to acknowledge the Sophisticated Instrumentation Center (SIC) at IIT Indore for access to the XRD, SEM, RAMAN, and EDX characterization instruments, which transformed my thesis from theoretical concepts into tangible evidence.

I would like to express my gratitude to **Prof. Sharath Sriram**, Professor at the School of Engineering, RMIT University, Melbourne, Australia, for fabricating IDE devices and for offering valuable suggestions to improve the quality of my research. I am also thankful to **Prof. Mahesh Kumar**, IIT Jodhpur, for his support in the fabrication of HMET devices.

I am deeply grateful to the Ministry of Education (MoE), Government of India, for the doctoral fellowship (TA) from December 2019 to January 2022. Additionally, thanks to the Technology Innovation Hub (TIH-IoT) Foundation IIT Bombay, for the Senior Research Fellowship from January 2022 to January 2025 under the TIH-IoT CHANAKYA Fellowship Program.

A heartfelt thank you to my batchmates, **Dr. Chandrabhan Patel**, **Dr. Mayank Dubey,** and **Kumari Jyoti** for your dependable support, engaging discussions, and invaluable assistance throughout my Ph.D. journey. Most importantly, your presence during challenging times has been a tremendous source of support, helping me navigate through difficulties.

To my seniors, **Dr. Pawan Kumar**, **Dr. Gaurav Siddharth**, **Dr. Biswajit Mandal**, **Dr. Md Arif Khan**, **Dr. Mangal Das**, **Dr. Ritesh Bhardwaj**, **Dr. Sanjay Kumar,** and **Dr. Ruchi Singh** – Your technical assistance and moral support have been the driving force propelling me forward.

I am also very thankful to my juniors and future doctoral candidates, **Saurabh**, **Vikash**, **Brahmadutta**, **Ajit**, **Animesh**, **Lokesh, Poonam**, and **Usha**, **Shorinjiryu,** for their valuable support and all the fun times. To the post-graduate juniors, **Ranjan, Shruti**, **Megha**, **Mohit**, **Sourajit**, your assistance was like the much-needed coffee breaks that kept me going.

Finally, to my family: **Shri. Bhoori Singh** (Father), **Smt. Kusama Devi** (Mother), **Amit Kumar** (Brother), and **Amrita Chaudhary** (Sister), **Susheela** (Sister), **Manju** (Sister-in-Law), **Payal** (Niece), **Archit Chaudhary** (Nephew) and **Deepak** (Nephew). Your boundless love, care, and encouragement have shaped me into the person I am today, both personally and professionally. I would have been nothing if you were not there through my journey.

I would like to specially thank my wife **Priyanka** for her love and support and encouraging me at difficult times.

Thank you all!

SUMIT CHAUDHARY

Dedicated to my family

LIST OF PUBLICATIONS

(A) Outcomes from Ph.D. thesis work:

A1. Patents

[1] A Sensor-based System to Detect Heavy Metal Ions in Water Samples Inventors: Shaibal Mukherjee, **Sumit Chaudhary**, Chandrabhan Patel, Brahmadutta Mahapatra, Vikash Kumar Verma, Mayank Dubey, Patent Application No. 202421061032, FILED (August 12, 2024), **PUBLISHED** (August 30, 2024).

A2. In refereed journals:

[1] **Sumit Chaudhary**, Chandrabhan Patel, Brahmadutta Mahapatra, Pawan Kumar, Mayank Dubey, Sharath Sriram, Shaibal Mukherjee, "Ag-Loaded WS_2-Based Pb^{2+} Ion Detection in Water," *IEEE Sensors Journal*, vol. 24, no. 3, pp. 2421-2428, 1 Feb.1, 2024, DOI: 10.1109/JSEN.2023.3341066. (**IF: 4.3**)

[2] **Sumit Chaudhary**, Pawan Kumar, Md Arif Khan, Amitesh Kumar, Shaibal Mukherjee, "Impact of MgO spacer layer on microwave performance of MgZnO/ZnO HEMT", *Eng. Res. Express*, vol. 4, 025007, 2022, DOI: 10.1088/2631-8695/ac6280 (**IF: 1.7**)

[3]**Sumit Chaudhary**, Chandrabhan Patel, Brahmadutta Mahapatra, Mayank Dubey, Vikash Kumar Verma, Pawan Kumar, Rajour Tanyi Ako, Sharath Sriram and Shaibal Mukherjee, "CVD-grown MoS_2 Monolayer based Ultrasensitive Hg^{2+} Ion Sensing in Water", *IEEE Sensors Journal*, Accepted. (**IF: 4.3**)

[4] **Sumit Chaudhary**, Brahmadutta Mahapatra, Vikas Pandey, Chandrabhan Patel, Mayank Dubey, Mahesh Kumar and Shaibal Mukherjee, " Ultrasensitive Detection of Hg^{2+} Ions with CVD Grown MoS_2 Functionalized MgZnO/CdZnO HEMT," *IEEE Sensors Journal*, Accepted. DOI: 10.1109/JSEN.2024.3504842 (**IF: 4.3**)

A3. In refereed conferences:

[1] **Sumit Chaudhary**, Pawan Kumar, Brahamdutta Mahapatra, Chandrabhan Patel, Mayank Dubey, and Shaibal Mukherjee, "Microwave Performance Analysis of MgZnO/CdZnO HEMT", IEEE 23rd International Conference on Nanotechnology (IEEE-NANO), Jeju, Republic of Korea, pp. 471-475, 2023, doi: 10.1109/NANO58406.2023.10231273.

[2] **Sumit Chaudhary**, Chandrabhan Patel, Brahmadutta Mahapatra, Kumari Jyoti, Mayank Dubey, Saurabh Yadav, Shaibal Mukherjee "Ultrasensitive Detection of Pb2+ Ions in Water Using WS2 Nanoflowers," 2024 IEEE 24th International Conference on Nanotechnology (NANO), Gijon, Spain, 2024, pp. 214-218, doi: 10.1109/NANO61778.2024.10628811.

(B) Other outcomes outside of the Ph.D. thesis work:

B1. Patents:

[1] A Method to Control Two-Dimensional Electron Gas Mobility and Carrier Density of Oxide-based Heterostructure, Inventors: Shaibal Mukherjee, **Sumit Chaudhary**, Brahmadutta Mahapatra, Chandrabhan Patel, Mayank Dubey, Pawan Kumar, Patent No. 553899, **GRANTED**, November 05, 2024.

[2] System and Method for Point-of-Care Diagnosis and Monitoring of Uric Acid Levels, Inventors: Shaibal Mukherjee, Jagat R Kanwar, Ajit Yadav, Chandrabhan Patel, Vikash Kumar, **Sumit Chaudhary**, Patent Application No. 202321073582, FILED (October 28, 2023), **PUBLISHED** (December 8, 2023).

[3] System and Method for Monitoring and Detecting Leakage of Toxic Gases to Enable User Alerts, Inventors: Shaibal Mukherjee, Chandrabhan Patel, Vikash Kumar, **Sumit Chaudhary**, Ajit Yadav, Patent No. 532213, **GRANTED**, April 8, 2024.

[4] A Wide Range Variable Resistance Readout Circuit, Inventors: Shaibal Mukherjee, Chandrabhan Patel, Vikash Kumar, **Sumit Chaudhary**, Ranjan Kumar, Patent No. 435803, **GRANTED**, June 27, 2023.

B2. In refereed journals:

[1] Chandrabhan Patel, **Sumit Chaudhary**, Vikash Kumar Verma, Mayank Dubey, Sharath Sriram, and Shaibal Mukherjee, "Photo-activated Pd-loaded WO_3 for Enhanced H_2S Sensing", *IEEE Sensors Journal*, vol. 23, no. 12, pp. 12552-12558, 2023. (**IF: 4.3**)

[2] Mayank Dubey, Sanjay Kumar, Saurabh Yadav, Chandrabhan Patel, **Sumit Chaudhary**, and Shaibal Mukherjee, "A Comprehensive Approach Toward Achieving High-Efficiency CTGSSe-Based Solar Cells", *IEEE Transactions on Electron Devices*, vol. 71, no. 10, pp. 6098-6103, Oct. 2024, DOI: 10.1109/TED.2024.3429082. (**IF: 3.2**)

[3] Pawan Kumar, Brahmadutta Mahapatra, **Sumit Chaudhary**, Rajour Tanyi Ako, Sharath Sriram, and Shaibal Mukherjee, "Effect of Rapid Thermal Annealing on DC Performance of $Mg_{0.3}Zn_{0.7}O/Cd_{0.15}Zn_{0.85}O$ MOSHFET", *Semiconductor Science and Technology*, vol. 39, no. 075012, pp. 1-8, June 2024, DOI: 10.1088/1361-6641/ad503f. (**IF: 1.9**)

[4] Mayank Dubey, **Sumit Chaudhary**, Chandrabhan Patel, Brahmadutta Mahapatra, Sanjay Kumar, Pawan Kumar, Myo Than Htay Yamamoto, and Shaibal Mukherjee, "Realization of High Photovoltaic Efficiency Devices with Sb_2S_3 Absorber Layer", *IEEE Transactions on Electron Devices*, vol. 71, no. 2, pp. 1115-1121, February 2024, DOI: 10.1109/TED.2023.3346852. (**IF: 3.2**)

[5] Chandrabhan Patel, Vikash Kumar Verma, **Sumit Chaudhary**, Ritesh Bhardwaj, and Shaibal Mukherjee, "Synergistic Approach for Controlled Doping in a MoS_2 Monolayer for Enhanced NH_3 Sensing",

ACS Applied Nano Materials, vol. 7, pp. 4546-4554, February 2024, DOI: 10.1021/acsanm.4c00271. (**IF: 5.3**)

[6] Ranjan Kumar, Chandrabhan Patel, **Sumit Chaudhary**, Mayank Dubey, Vikash Kumar Verma, Sharath Sriram, and Shaibal Mukherjee, "Surfactant-Assisted WS_2 Nanostructures for Enhanced NO_2 Sensing Performance", *IEEE Sensors Journal*, vol. 24, no. 5, pp. 5813-5820, March, 2024, DOI: 10.1109/JSEN.2023.3348481. (**IF: 4.3**)

[7] Mohit Kumar Gautam, Sanjay Kumar, **Sumit Chaudhary**, Lokesh Kumar Hindoliya, Dhananjay D. Kumbhar, Jun Hong Park, Myo Than Htay, and Shaibal Mukherjee, "Experimental Validation of Switching Dependence of Nanoscale-Y2O3 Memristor on Electrode Symmetry via Physical Electro-Thermal Modeling", *ACS Applied Electronic Materials,* vol. 5, pp. 3885−3893, July 2023, DOI: 10.1021/acsaelm.3c00598. (**IF: 4.4**)

[8] Pawan Kumar, **Sumit Chaudhary**, Md Arif Khan, Ruchi Singh, Myo Than Htay, Rahul Prajesh, Ajay Agarwal, and Shaibal Mukherjee, "Impact of ZnO Cap Layer on the Performance of MgZnO/CdZnO Heterostructure with Y2O3 Spacer Layer", *IEEE Transactions on Electron Devices*, vol. 69, no. 11, pp. 5991-5995, September 2022, DOI: 10.1109/TED.2022.3206172. (**IF: 3.2**)

[9] Pawan Kumar, **Sumit Chaudhary**, Md Arif Khan, Sanjay Kumar, and Shaibal Mukherjee, "Analytical Study of ZnO-based HEMT for Power Switching", *International Journal of Numerical Modelling: Electronic Networks, Devices and Fields,* vol. e3048, pp. 1-8, July 2022, DOI: 10.21203/rs.3.rs-1140403/v1. (**IF: 1.9**)

B3. In refereed conferences:

[1] Chandrabhan Patel, Mayank Dubey, **Sumit Chaudhary**, Vikash Kumar, Shaibal Mukherjee, "Role of Carrier Gas and its Flow Rate to Produce Uniform, Large-Sized MoS_2 Monolayer via CVD", IEEE 23rd International Conference on Nanotechnology (IEEE-NANO), Jeju, Republic of Korea, pp. 490-493, 2023, doi: 10.1109/NANO58406.2023.10231184.

[2] Mayank Dubey, Chandrabhan Patel, **Sumit Chaudhary**, Myo Than Htay, Shaibal Mukherjee, "Morphological and Quantum Analysis of Cu2SnGe(S,Se)3 Thin Films for Photovoltaic Application", EM-NANO 2023, Kanazawa, Japan, June 5-8, 2023.

TABLE OF CONTENTS

Chapter 1: Introduction and Fundamental Concepts

Chapter 2: Synthesis, Fabrication and Characterization Techniques

Chapter 3: Ag-Loaded WS_2-Based Pb^{2+} Ion Detection in Water

Chapter 4: CVD-grown MoS_2 Monolayer based Ultrasensitive Hg^{2+} Ion Sensing in Water

Chapter 5: Ultrasensitive Detection of Hg^{2+} Ions with CVD Grown MoS_2-Functionalized MgZnO/CdZnO HEMT

Chapter 6: Conclusion and Future Scope

LIST OF FIGURES

LIST OF FIGURES

LIST OF FIGURES

LIST OF FIGURES

LIST OF TABLES

ACRONYMS

HMI	*Heavy Metal Ion*
WHO	*World Health Organization*
BIS	*Bureau of Indian Standards*
AAS	*Atomic Absorption Spectroscopy*
TMD	*Transition Metal Dichalcogenides*
NP	*Nanoparticle*
FET	*Field-effect Transistor*
DI	*De-Ionized*
ISFET	*Ion-selective Field-effect Transistor*
HEMT	*High Electron Mobility Trasnsistor*
LoD	*Limit of Detection*
2DEG	*Two-dimensional Electron Gas*
CVD	*Chemical Vapour Deposition*
MFC	*Mass Flow Controller*
IDE	*Interdigitated Electrode*
DC	*Direct Current*
RT	*Room Temperature*
DIBS	*Dual Ion Beam Sputtering*
IPA	*Iso-Propyl Alcohol*
DPC	*Deposition Chamber*
LLC	*Load Lock Chamber*
PVD	*Physical Vapor Deposition*
Mo	*Molybdenum*
HF	*Hydrofluoric Acid*
FESEM	*Field Emission Scanning Electron Microscopy*
XRD	*X-Ray Diffraction*
FWHM	*Full Width at Half Maximum*
EDX	*Energy Dispersive X-ray Spectroscopic*
AFM	*Atomic Force Microscopy*
Si	*Silicon*

SCCM	*Standard Cubic Centimetres per Minute*
eV	*Electron Volt*
XPS	*X-ray Photoelectron Spectrometer*
PPB	*Parts per Billion*
PPM	*Parts per Million*
PPT	*Parts per Trillion*

NOMENCLATURE

P_s	*Spontaneous Polarization*
P_z	*Piezoelectric Polarization*
μ	*Micro*
Hg	*Mercury*
Pb	*Lead*
Cd	*Cadmium*
eV	*Electron Volts*
a, c	*Lattice Constants*
Ar	*Argon*
V	*Voltage*
I	*Current*
mm	*Milimeter*
^{o}C	*Degree Celcius*
min	*Minute*
s	*Seconds*
sccm	*Standard Cubic Centimeters per Minute*
cm	*Centimeter*
nm	*Nanometer*
E_g	*Energy Bandgap*
σ	*Standard Deviation*
m	*Sensitivity*
V_{th}	*Threshold Voltage*
$g_{m,max}$	*Maximum Transconductance*
I_{ds}	*Drain Current*
W	*Watt*

ABSTRACT

Heavy Metal Ion Sensing in Water via TMD Functionalized Oxide HEMT

by

Sumit Chaudhary

Hybrid Nanodevice Research Group
Department of Electrical Engineering
Indian Institute of Technology Indore
Supervisor: Prof. Shaibal Mukherjee

Heavy metals like mercury (Hg^{2+}), lead (Pb^{2+}), arsenic (As^{3+}), cadmium (Cd^{2+}), and chromium (Cr^{3+}) are pervasive in the environment, exposing humans to risks from these elements. Such exposure can lead to severe health problems, including neurological and respiratory issues, kidney disease, anemia, and various cancers. Diseases like minamata disease, arsenicosis, itai-itai, and lead poisoning are linked to these metals, affecting vital systems such as the nervous, cardiovascular, respiratory, and skeletal systems. Monitoring heavy metal levels in water pollution is essential, as it threatens ecological and human health across India. Traditional detection methods, such as GFAAS, ICP-OES, and ICP-MS, have limitations in portability and response time. Few recent approaches such as fluorescent, colorimetric, and electrochemical sensors have shown promise results but still face challenges like lack of portability, high cost, portable, and lack of user-friendly platform for rapid, real-time heavy metal analysis. Addressing these limitations is crucial for the widespread accessible use of heavy metal ion detectors. Electrochemical sensors are a viable solution for these issues, however one of the key elements for this solution is the sensing material, which affects the efficiency of detecting the targeted analyte and the performance of the electrochemical sensor based heavy metal ion detectors. Numerous nanomaterials, including boron nitrides, carbon-based materials (like graphene and its oxides),

MXenes, and layered double hydroxides, have been explored for HMI detection because of their distinctive properties. Nevertheless, these sensing materials face several drawbacks, such as lower stability, fewer adsorption sites, poor dispersibility, limited biocompatibility, reduced surface area, lower chemical reactivity, small particle size, and substandard durability. This thesis focusses on the synthesis of TMD materials as sensing layer and using these to functionalize the interdigitated device and MgZnO/CdZnO HEMT to enable the sensing of heavy metal ions.

In the initial phase of the thesis, pristine and Ag-loaded tungsten disulfide (WS_2) with 1, 2, and 4 wt% of Ag were synthesized using a hydrothermal method. The synthesized WS_2 was characterized using scanning electron microscopy (SEM), X-ray diffraction (XRD), and X-ray photoelectron spectroscopy (XPS). The WS_2 layer was then deposited onto an interdigitated device via drop casting. The fabricated device was evaluated for heavy metal ion sensing present in water and demonstrated excellent selectivity towards lead (Pb^{2+}) ions. The sensor exhibited remarkable performance, achieving a high sensitivity of 819 µA/ppb, a detection limit of 75 ppt, and a rapid response time of less than 5 seconds.

Further, molybdenum disulfide (MoS_2) monolayer was synthesized on a SiO_2/Si substrate using a chemical vapor deposition (CVD) system. The synthesized MoS_2 was characterized through various techniques, including a digital microscope, atomic force microscopy (AFM), Raman spectroscopy, and X-ray photoelectron spectroscopy (XPS). These characterizations confirmed the successful synthesis of a monolayer MoS_2. Subsequently, the monolayer was transferred onto an interdigitated device using a surface energy-assisted wet transfer method. The fabricated device was evaluated for its heavy metal ion sensing capabilities, demonstrating excellent selectivity towards mercury (Hg^{2+}) ions. This high selectivity is attributed to the high reduction potential of Hg^{2+} ions compared to other heavy metals, leading to the formation of Hg-S complexes and their reduction at the MoS_2 surface. The sensor showcased exceptional performance, with a sensitivity of 957 µA/ppb, a

detection limit of 27.5 ppt, and an impressive response time of under 4 seconds.

In the final part of this thesis, the stability and detection limit for Hg^{2+} ions were enhanced by functionalizing the gate region of an oxide HEMT with MoS2, enabling effective mercury ion sensing. Prior to fabricating the oxide HEMT, various device structures were simulated using Silvaco TCAD. The initial MgZnO/ZnO (MZO) HEMT was simulated and validated against experimental results from the literature. In this structure, a 1 nm MgO layer was sandwiched between the MgZnO and ZnO layers and further the ZnO layer was replaced with CdZnO, leading to the simulation of the MgZnO/CdZnO (MCO) HEMT. This modification enhanced the confinement of the two-dimensional electron gas (2DEG), crucial for sensing applications. The MCO HEMT exhibited superior performance, achieving a saturation drain current of $I_{\mathrm{DS}} = 281$ mA/mm at $V_{\mathrm{GS}} = 1$ V and $V_{\mathrm{DS}} = 5$ V, and a maximum transconductance ($g_{\mathrm{m,max}}$) of 103 mS/mm, due to the increased electron density in the channel because of enhanced polarization charge with the introduction of Cd in ZnO. Based on its improved performance and higher 2DEG density, the MCO HEMT was selected for further heavy metal ion sensing studies. The MCO HEMT was fabricated using optical lithography and a dual ion beam sputtering (DIBS) system, with Si_3N_4 passivating the source and drain contacts. To enable Hg^{2+} ion sensing, a MoS_2 layer was transferred onto the gate region via an energy-assisted wet transfer method. The fabricated sensor demonstrated exceptional performance, achieving a sensitivity of 9.55 µA/ppb, a detection limit of 6.5 ppt, and a rapid response time of under 4 seconds, enabled by the multilayer sensing mechanism for Hg^{2+} ions.

In conclusion, this thesis presents the successful synthesis and characterization of WS_2 and MoS_2 using hydrothermal and CVD methods, respectively, which were utilized as sensing layers on interdigitated devices and MCO HEMTs for Pb^{2+} and Hg^{2+} ions in water. The MCO HEMT-based sensor exhibited exceptional performance, establishing it as a promising candidate for real-world applications in environmental monitoring and the detection of toxic metals in water.

Chapter 1

Introduction and Fundamental Concepts

1.1. Motivation

In many parts of the world, water, which is vital to human existence, is already becoming limited. 2.6 billion people lack proper sanitation, and 1.1 billion people worldwide lack access to safe drinking water (UNICEF/WHO JMP 2004). The water waste released from residential and industrial sources, both organic pollutants (e.g., pathogens, bacteria, toxic and non-toxic organisms) and inorganic pollutants (e.g., heavy metals). Among these, the most harmful substances that can cause cancer and other health issues for people are heavy metal ions (HMIs). This water waste is released mostly without any treatment into the natural water bodies; subsequently, this water is used for irrigation of crops by farmers, which results in the heavy metal build-up in the soil, making it unfit for farming. Soil contamination is a hidden danger that is affecting the ecosystem worldwide.

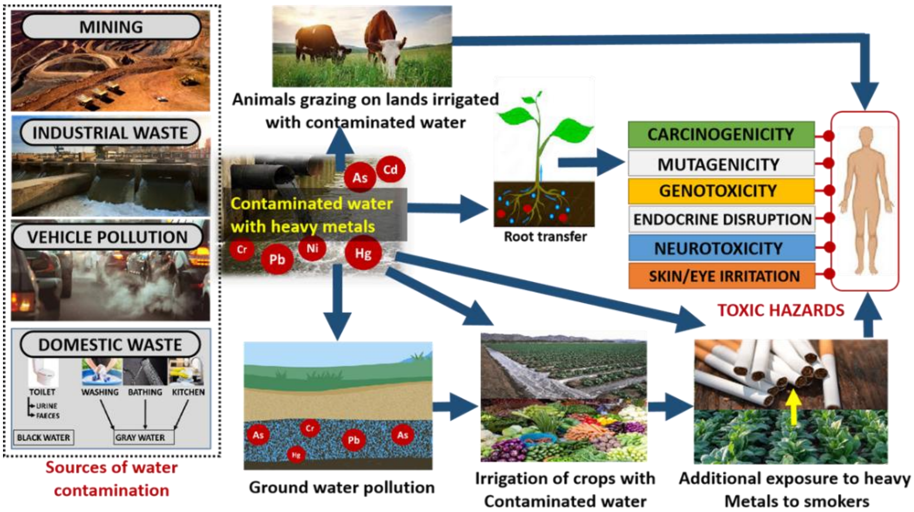

***Figure 1.1:** The heavy metals that are transferred from water to plants and organisms' food to humans.*

The heavy metals are then transferred to the crop from the soil, and heavy metals enter the food chain, and are finally consumed by humans, as shown in figure 1.1. The problem of water shortage will get worse as the amount of pollutants in natural water bodies increases. The issue with hazardous contaminations in water bodies is that they are typically only discovered after they begin to negatively impact the health of a region's broader population. Water pollution is the most dangerous form of pollution affecting our entire ecological system. Water bodies at various parts of India are observed to contain mercury (Hg^{2+}), lead (Pb^{2+}), cadmium (Cd^{2+}), arsenic (As^{3+}), zinc (Zn^{2+}), etc. beyond permissible limits. Excess of these impurities affects humans in various ways. So, there is an urgent need for the sensors which can detect these HMIs at a trace amount in water.

1.2. HMI Pollution and its Damage

Although there isn't a universally recognized definition of heavy metals, density is typically used to identify them. A metal is categorized as heavy if its density is more than 5 g/cm^3 [1]. These metals have the potential to endanger human health and pollute the environment. Table 1.1 [2, 3] provides a summary of the types of HMIs, and their impact on human health, as well as the acceptable levels of HMIs in water provided by Word Health Organization (WHO) and Bureau of Indian Standards (BIS).

Table 1.1: *The effects of HMIs on human health and the acceptable thresholds for them.*

HMIs	Effect on human health	Major Sources	Permissible level (ppm)	
			WHO	BIS
Lead	Acute or chronic nervous system	Burning of coal, paint,	0.01	0.01

	damage, epilepsy, liver, renal, and gastrointestinal damage, congenital paralysis, sensor neural deafness, developmental delay, fatal newborn encephalopathy, and mental retardation in children	smoking, pesticide, emission, automobile mining,		
Mercury	The nerve system, impaired development of the nervous system, impacts on the lungs, kidneys, skin, eyes, immunological system, and digestive system, Acrodynia, minamata, increased salivation, hypotonia, hypertension, and renal issues	Batteries, fisheries, Pesticides, Volcanic emissions, paper industries	0.001	0.001
Arsenic	Dermatitis, bronchitis, poisoning, brown pigmentation, anorexia,	Fungicides, pesticides, metal smelters, industrial wastes	0.01	0.01
Chromium	Reproductive toxicity, teratogenicity,	Mines, electroplating	0.05	0.05

	embryotoxicity, carcinogenicity, mutagenicity, dermatitis, skin ulcers, lung cancer.	, mineral sources leather industry, tanning,		
Copper	kidney and Liver damage, anaemia, intestinal and stomach irritation	Mining, pesticide production, metal piping	2	0.05
Cadmium	Lung cancer, renal dysfunction, bone defects, bronchitis.	Cd and Ni batteries, nuclear fission plant	0.003	0.003

Human health is seriously endangered by heavy metal exposure. It is well recognized that mercury is extremely poisonous and that its buildup in the body can result in deadly conditions such cyanosis syndrome, nephrotic syndrome, minamata disease, and pulmonary edema [4]. In addition to harming the gastrointestinal and neurological systems, it may cause renal and respiratory failure [4]. To regulate the usage of mercury ions, several rules have been created. Nonetheless, it continues to be widely utilized in several commercial and residential applications, including as mining and power plants, insecticides, architecture, cosmetics, and thermometers. They will thus result in the burning of coal at high temperatures, the processing of chlorine alkali for the power plant, and the incineration of garbage containing items connected to mercury. In addition to these human-related sources of mercury, there are also natural sources, such as naturally occurring mercury deposits, volcanic eruption-related leaks, and ocean volatilization [5]. Mercury will enter the atmosphere and/or water sources from all of these sources. The fish will become polluted after the water has been tainted. Therefore, drinking contaminated water or eating infected fish will pose a threat to human life safety, particularly for young children, babies, and fetus.

In addition to mercury, lead are another well-known heavy metals that is extremely harmful to human health. Numerous complaints have surfaced recently regarding lead contamination of water, which seeps from water pipe systems into tap and drinking water [6, 7]. Lead ions from chrome-plated or soldered brass faucets and fittings are the most frequently reported source of lead contamination because water with a high acidity or low mineral content can corrode lead-containing pipes or fixtures. Then, significant amounts of lead could end up in the water, especially hot water [4]. Additionally, homes constructed prior to 1986 are more likely to include lead pipes, fixtures, and solder. Lead poisoning is now a health risk, particularly for young children and newborns. Throughout history, cases of lead poisoning have been documented in ancient Greece, Rome, and India. In animals, excessive lead causes blood and brain issues and harms the central nervous system [8]. Because of the covalent interaction between the Pb^{2+} 6s and filled ligand orbitals (like O 2p), Lead can combine with biological matter ligands that contain oxygen, sulfur, and nitrogen to create complexes. Consequently, bonding and antibonding molecular orbitals (MOs) can be formed by empty 6p orbitals [9]. Moreover, the combination results in hydrogen bond breakage, enzyme inhibition, and modifications to the molecular structure of proteins.

1.3. HMI Sensor

Sensors designed to detect HMIs are a subset of chemical sensors. These sensors translate information about specific HMIs into analytical signals suitable for subsequent processing. As seen in Figure 1.2, the three fundamental components of the HMIs sensor are the transducer, receptor, and signal processing unit.

Receptor

Receptors can also be called functionalizing or recognizing components. It refers to a layer which has the ability to interact with certain ions of heavy metals. Furthermore, it can enhance selectivity for specific HMIs or a group of them. As illustrated in Figure 1.2, various receptors carry out distinct interactions with HMIs, such as redox processes, ion exchange, reduction, oxidation, adsorption, and liquid-solid or liquid-liquid interactions to detect specific HMIs at the receptor/ion interface. The functionalizing element interacts with the heavy metal in the majority of HMI sensing applications to provide the transducer with sufficient information to produce the desired signal.

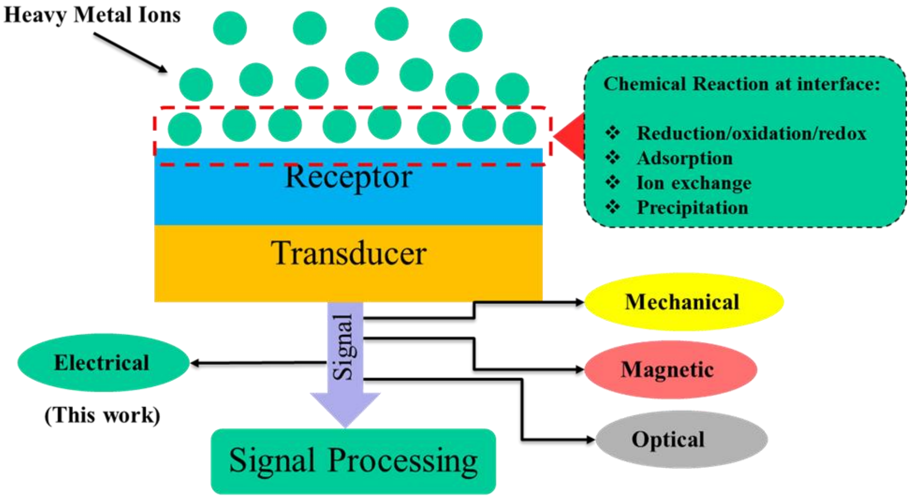

Figure 1.2: *Schematic of a HMI sensor.*

Transducer

The transducer in the HMI sensor converts the acquired data, such as heat or charge, into the desired signal, which could be electrical, mechanical, magnetic, optical or auditory. For HMI sensing applications, an electrical transducer is commonly employed, generating signals in the form of current, resistance, or voltage. This is because the signal produced by the transducer is now used for both signal processing and data storage.

Signal Processing

The apparatus or sensing system used to evaluate, store, and contrast the data obtained from the transducer is referred to as the signal processing system. It may also stand in for the electronic circuits or systems that handle the signal processing of the received signal and carry out various tasks including signal amplification and conversion from analogue to digital, among many others.

1.4. Types of HMI Sensor

Various techniques have been developed to create HMI sensors capable of detecting HMIs at trace and sub-trace concentrations. The wide categorization of several HMI sensor types, including electrochemical, colorimetric, biological, and semiconductor-based, is depicted in Figure 1.3. These sensors have been categorized according to the functionalizing elements, materials, and methodologies that have been applied. Furthermore, a number of spectroscopic methods are used to detect HMIs in aqueous solutions, including inductively coupled plasma mass spectroscopy (ICP-MS), atomic absorption spectroscopy (AAS), and inductively coupled plasma-optical emission spectrometry (ICP-OES). However, these approaches are quite expensive and need skilled personnel to operate their sophisticated machinery. Furthermore, these techniques have a significant risk of error while handling, altering, and storing samples, and they necessitate a complex analytical procedure for sample preparation [10]. To address the requirement for detecting HMIs in aqueous solutions, the sensors listed above and in Figure 1.3 are therefore crucial. The following provides a thorough explanation of various heavy metal sensors:

1.4.1. Electrochemical HMI Sensors

Electrochemical HMI sensors are chemical sensors that utilize electrochemical methods to detect HMIs in aqueous solutions. These sensors are classified based on the various electrical signals—such as current, voltage, impedance, resistance, charge, and electrochemiluminescence—that are generated by the HMIs in the solution. Based on these electrical signals, electrochemical processes such as electro chemiluminescent, amperometry, resistive, voltametric, impedance measurement, and ion sensors can be used for HMI detection [10]. These techniques use either voltage or current as a controlling parameter to see how one changes. Two or three electrodes were employed in the electrochemical sensor to detect HMIs.

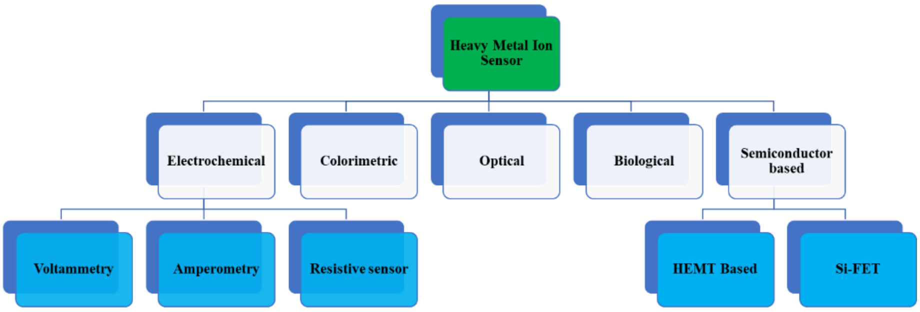

***Figure 1.3**: Types of HMI sensors.*

Amperometry

The electrochemical technique known as amperometry measures the current at a given applied voltage at the working electrode. In this case, a set voltage is supplied between the HMI solution's working and reference electrodes. The change in the measured current reflects the concentration of HMIs in the solution, which is linked to the reaction mechanism taking place at the working electrode. Time is used to measure the reaction in the form of current.

Voltammetry

Due to its great sensitivity and accuracy, voltametric methods are widely used in HMI detection. In contrast to the fixed potential in the amperometry analysis, it is utilized to measure current at different potentials in an I-V.

Resistive Sensor

Semi-conductive materials, primarily metal oxides like WO_3, SnO_2, TiO_2, and MoO_3, as well as two-dimensional transition metal dichalcogenides (TMDs) like MoS_2, WS_2, $MoSe_2$, and WSe_2, are commonly used in the construction of semiconductor HMI sensors. Numerous heavy metals, such as Pb, Hg, Cr, Cd, etc. can be detected by these sensors. When these semiconducting materials are exposed to test heavy metals, their resistance changes, which is how the sensing mechanism works. These test heavy metal molecules usually react with the deposited material layer. The sensing layer resistance either rises or falls depending on the test heavy metals molecule's nature (oxidizing or reducing) and the sensing layer's semiconducting type (n-type or p-type). In order to monitor electrical resistance, these sensors are made by inserting the sensing layer between or on top of two metal electrodes (such as Au or Pt) on an insulating substrate, as shown in Figure 1.4.

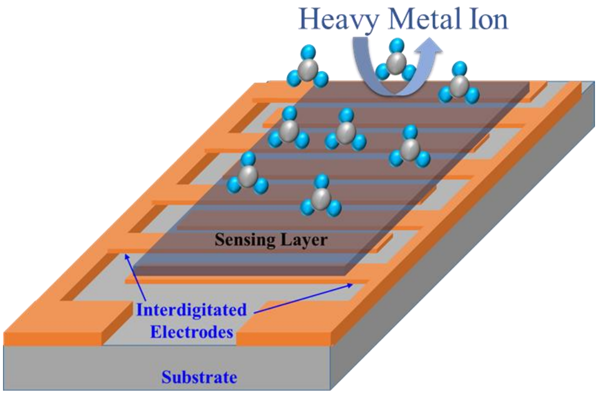

Figure 1.4*: Interdigitated electrode device based resistive HMI sensor.*

1.4.2. Colorimetric HMI Sensors:

Colorimetry is another widely used method for HMI sensing, which identifies color changes resulting from a chemical interaction between the functionalizing element and the HMIs. One advantage of colorimetry-based HMI sensors is their ability to detect multiple HMIs simultaneously in an array [11]. Nowadays, colloidal nanoparticles (NPs) of various HMIs, such as silver and gold, are frequently used for colorimetric detection. Colorimetry based HMI sensors can typically be used only once for detection, as most reactions in colorimetric analysis are irreversible. Consequently, such sensors are unsuitable for consistent and reliable HMI detection.

1.4.3. Optical Sensors for HMI Sensor:

The kind of sensor that recognizes element interaction and identifies optical variations in the stimulus caused by the HMI is called an optical HMI sensor. The amount of HMIs in the water is determined by these changes. Optical HMI sensors offer several advantages, including the need for compact equipment, sensitivity to electromagnetic interference, and straightforward construction. Based on the underlying mechanism, these sensors are divided into three categories: luminescence-based, fluorescence-based, and absorption-based ion sensors [12].

1.4.4. Biosensors for HMI Detection

A simple, quick, and accurate method of identifying various HMIs in water is to use biosensors. Small and capable of in-situ applications, these devices are preferable to costly and time-consuming laboratory studies. Biosensors indicate the biological impacts of HMIs, such as toxicity, and identify their presence and precise quantities in water. Generally speaking, biosensors use biological components like enzymes and DNA (deoxyribonucleic acid) to detect HMIs [13].

1.4.5. Semiconductor based HMI Sensors

Ion-selective field-effect transistors (ISFETs) are a specialized sensor that integrates electronic devices with electrochemical principles for detecting HMIs. In these sensors, the gate terminal's surface is functionalized to detect target molecules. Field-effect transistors (FETs) are commonly used in semiconductor-based HMI sensors for sensing applications. An external electric field supplied to the gate terminal of a field-effect transistor (FET) controls the current flow between the source and drain terminals. ISFET sensors are widely employed in a variety of chemical and environmental sensing applications due to its electrical and chemical properties. Contemporary ISFET sensors have reduced the size of the entire sensor, creating the possibility of integration into the electronic world [14]. Due to their compact size, these devices are well-suited for portable sensing applications. In the initial phases, ISFETs garnered considerable research interest, as reflected in the volume of publications [15]. Si-FETs have matured in terms of ISFETs, which are utilized in biological and other environmental applications in addition to HMI sensing applications. Moreover, Si-ISFETs have enhanced the affordable large-scale production of HMI sensors; however, they require proper insulation and face challenges with long-term chemical stability in aqueous solutions [16].

As was already noted, cutting-edge devices like HEMT are used in the development of ISFETs today for next-generation sensing applications. Because of their special characteristics, these HEMT-based HMI sensors offer improved stability in addition to quick and accurate ion detection.

1.5. HMI Sensing Terminology

Numerous parameters, such as selectivity, sensitivity, response and recovery time, repeatability and reproducibility, limit of detection, and long-term stability as shown in Figure 1.5 are used to characterize and evaluate the performance of HMI sensors. The sensor's distinctiveness and usefulness for various applications are also determined by these parameters.

Sensitivity

One important HMI sensor statistic is sensitivity, which is the proportionate change in the recorded signal for each unit concentration of the HMIs. Stated differently, it can also be referred to as a calibration curve's slope. To detect HMIs, a sensor has to have a high sensitivity.

Limit of Detection

The limit of detection (LoD) refers to the smallest concentration of HMIs in a solution that a sensor can detect using a specific analytical technique. "The limit of detection, expressed as a concentration, is derived from the smallest measure that can be detected with reasonable certainty for a given analytical procedure," according to a 1975 definition of the term by the International Union of Pure and Applied Chemistry (IUPAC) [17].

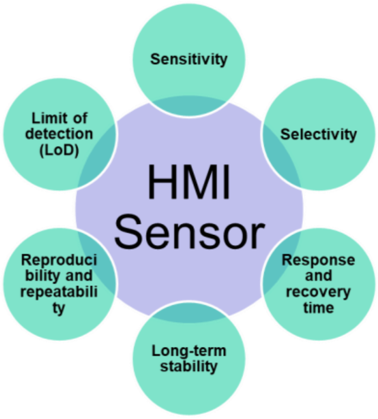

Figure 1.5: *Characteristics of HMI sensor.*

Selectivity

The capacity of a sensor to distinguish one HMI from a mixture of HMIs is known as selectivity. By comparing the measured sensor response for every test HMI, it may be ascertained.

Response and Recovery Time

A HMI sensor's response time is the amount of time needed to increase the sensor's response from 10% to 90% following a concertation modification. One important metric that demonstrates the sensor's efficacy in terms of quick detection is response time. Recovery time refers to the duration it takes for the sensor to return to its baseline response (measured in the blank solution) after administering the solution, typically ranging from 90% to 10%. A highly effective HMI sensor should have the shortest response and recovery time feasible.

Long-term Stability

Long-term stability is the capacity of a sensor to sustain a constant response or other sensing properties over a prolonged duration.

Repeatability and Reproducibility

Reproducibility and repeatability are ways to assess an ion sensor's accuracy. By doing the sensing operation under identical operating circumstances, the sensor's repeatability was noticed. Reproducibility, on the other hand, is the consistency of the sensing responses recorded on several samples and under various operating situations.

1.6. Transition Metal Dichalcogenides (TMD)

The performance and efficiency of electrochemical sensors in accumulating target analytes largely depend on the selection of appropriate sensing materials. Several nanomaterials, including carbon-based materials (e.g., graphene oxide), boron nitride materials (BNMs), layered double hydroxides (LDHs), and MXenes, have been investigated for HMI sensing due to their distinct properties. However, these materials face challenges such as low colloidal stability, limited adsorption sites, poor dispersibility, low chemical reactivity, low surface area, small particle size, poor durability, and limited biocompatibility [18-23]. As a result, there is a pressing need for the development of an effective electrochemical sensing interface capable of detecting HMIs with high sensitivity.

Recent research has shown considerable interest in transition metal dichalcogenides (TMDs), owing to their exceptional properties, including a high surface-to-volume ratio, tunable bandgap, and excellent catalytic behavior [24, 25]. These layered materials, with a structure denoted as MX_2, consist of transition metals such as Ti, Mo, and W ("M") and chalcogen elements from group VI-A, such as S, Se, and Te ("X") [26, 27]. The range of properties these materials offer spans from insulating to metallic characteristics. Within the layers, strong covalent bonds hold the structure together, while relatively weak Van der Waals forces between layers allow for easy transitions [24, 25]. Among semiconducting TMDs, MoS_2 and WS_2 have garnered significant attention due to their high surface area, exceptional electronic properties, superior catalytic behaviour, and enhanced stability [27-29]. Consequently, this thesis uses MoS_2 and WS_2 as sensing layers for detecting Hg^{2+} and Pb^{2+} ions in water.

1.7. Oxide HEMT

Mimura et al. demonstrated the first HEMT ever fabricated using a GaAs material system in 1979, and it became commercially accessible in 1985 [30, 31]. This HEMT seems intriguing for high-power high-frequency applications because of its larger bandgap (1.4 eV) and electron mobility (5000 cm^2/Vs) in comparison to Si MOSFETs, which had a bandgap of 1.1 eV and an electron mobility of 1400 cm^2/Vs. First created by Khan et al. [32] in 1993, GaN material system-based HEMTs have higher bandgaps (3.4 eV), breakdown voltages (3 MV/cm), and electron saturation velocities (2×10^7 cm/s) than GaAs. However, the lack of native GaN substrates drives up manufacturing costs, rendering them unsuitable for large-scale HEMT manufacture.

ZnO provides a more cost-effective and efficient material system than GaN. ZnO-based HFETs can tolerate high radio frequency (RF) power because of their broad bandgap (3.43 eV), strong breakdown field (3 MV/cm), considerable conduction band offset, and high saturation velocity (3×10^7 cm/s) [33, 34]. Koike et al. demonstrated the first

MgZnO/ZnO-based HFET via MBE in 2005 [35], while the first 2DEG demonstration in a MgZnO/ZnO heterostructure was documented in 2004 [36]. In 2010, Chin et al. [37] reported the first 2DEG for the first time in a MgZnO/ZnO heterostructure by using sputtering. Singh et al. [38], reported 2DEG in a MgZnO/ZnO heterostructure using dual ion beam sputtering (DIBS). It should be noted that sputtering is a low-cost, large-area compatible growth technique that allowed for the production of low-cost HEMTs.

MgZnO/ZnO heterostructures may create high two-dimensional electron gas (2DEG) sheet density (n_s) (~10^{13} cm^{-2}) at ambient temperature, as demonstrated by Tampo et al. [39]. In order to achieve such high n_s, up to 0.6, barrier layer MgZnO needs a high Mg concentration and is difficult to build without phase separation [40]. This implies that with lower Mg content in the barrier layer, it is very difficult to attain a greater 2DEG density in a MgZnO/ZnO heterostructure. In order to overcome this limitation, Benharrats et al. [41] have shown that 2DEG may be increased by using a CdZnO/ZnO heterostructure. Although employing a CdZnO/ZnO heterostructure is beneficial for increasing 2DEG density compared to that in MgZnO/ZnO, the primary drawback of all these structures is that the polarization in ZnO buffer does not significantly increase. Consequently, the polarization of the barrier layer is the only element affecting any increase in 2DEG density. In 2018, Khan et al. [41] addressed this restriction by substituting the ZnO with the CdZnO as buffer layer. This makes it possible to get increased n_s, which was previously only possible with the barrier layer, by altering the polarization components of the barrier and buffer layers. Therefore, in this work MgZnO/CdZnO HEMT has been fabricated and used for HMI detection due to its high 2DEG density which plays an important role in sensing.

1.7.1. Heterostructure

A heterostructure is produced when two different materials are stacked on top of each other while maintaining their own characteristics. When a large band gap difference is present, the energy band spectrum at the interface of such heterostructures produces an energy discontinuity. In centrally band aligned heterostructures with either undoped or n-type doped material, the energy discontinuity causes the energy band to bend, creating a valley in the valence band and a notch in the conduction band at the interface. These features are both produced in the smaller band gap material. Figure 1.6 displays a band diagram illustrating the band gap discontinuities in heterostructure materials both before and during junction formation. In the case when the notch formation in the conduction band is situated below the fermi energy level, the energy levels below the fermi energy level can absorb electrons without the influence of the lattice atoms of either material, creating a quantum potential well. These energy levels are called two-dimensional energy states (2DES) because of their capacity to take in two-dimensional electron gas (2DEG). Therefore, the heterostructure's tolerance to 2DEG is determined by the depth of this notch. The depth of the notch is determined by the conduction band discontinuity (ΔE_c) or conduction band offset, which is based on the bandgap discontinuity (ΔE_g), which is the difference in the band gaps of two materials.

An example is a ZnO-based heterostructure in which ZnO is the low band gap material (buffer layer) and MgZnO is the high band gap material (barrier layer). The quantity of magnesium in the barrier layer determines the bandgap of MgZnO. The formula for determining ΔE_c in the context of the MgZnO/ZnO heterostructure is $\Delta E_c = 0.9\times \Delta E_g$.

1.7.2. Polarization in Heterostructures for 2DEG Formation

In compound materials with asymmetric lattice structures that have covalent bonding (like GaN and GaAs) or borderline iconicity between covalent and ionic (like ZnO), the electronegativity of the different elements in the lattice results in a dipole-like electron cloud distribution at every bonding pair. The vector summing of all such dipoles over the unit lattice structure generates spontaneous polarization (P_s) in the compound when there is no external electric field present. The relative locations of the lattice's constituent parts are altered when such lattices are mechanically stretched or compressed. The shift between two polarities of the dipole moment at the bonding pairs alters the compound's polarization. The mechanical stress-induced polarization is referred to as piezoelectric polarization (P_z).

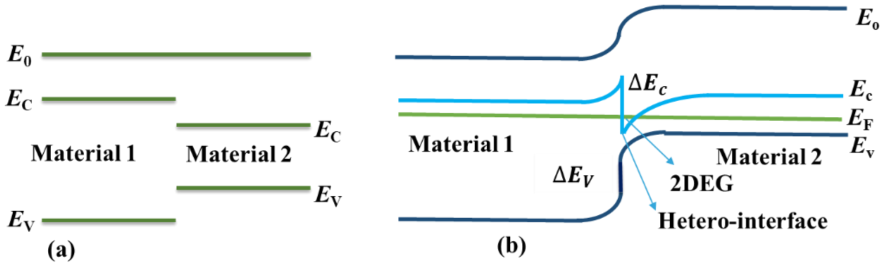

Figure 1.6: *Energy Band diagram of heterostructure, (a) before junction formation and (b) after junction formation at thermo-dynamic equilibrium.*

In a heterostructure with polarization in both layers, a polarization difference may occur at the interface between the heterostructures if the polarization in one layer is greater than the polarization of the other layer. This causes this heterostructure stack's net electric neutrality to fall out of balance. An electric field created by this net polarization difference at the heterostructure's interface has the ability to sweep free charges with opposing polarities within the heterostructure. The electrostatic attraction of the localized net polarization difference causes these free charges to accumulate at the interface of the heterostructure. The overall electric field is zero near the interface because the opposite polarity free charge carriers accumulate and balance out the net polarization difference. These free charge carriers gathered at the interface can be either holes or electrons, depending on the polarity (positive or negative) of the net polarization formed at the heterostructure stack interface, as shown in figure 1.7. The polarity of polarization of the material at the contact is usually determined by the growth face of the crystal. In ZnO-based devices, the direction of P_s is determined by the growing face of the crystal (Zn or O at the surface). The P_z component in ZnO buffer is negligible because the ZnO buffer layer is usually strain-relaxed due to its thickness of 1 μm [37, 42]. However, strain is always present because of the thickness of the MgZnO barrier layer. Consequently, in addition to P_s, the MgZnO barrier layer also contains P_z. At the interface of a MgZnO/ZnO heterostructure, a net polarization difference charge forms, the polarity of which is determined by the face of the crystal growth. Any positive charge polarization difference at the MgZnO/ZnO heterostructure interface is balanced by the equal negative charge (free electrons swept by electric field).

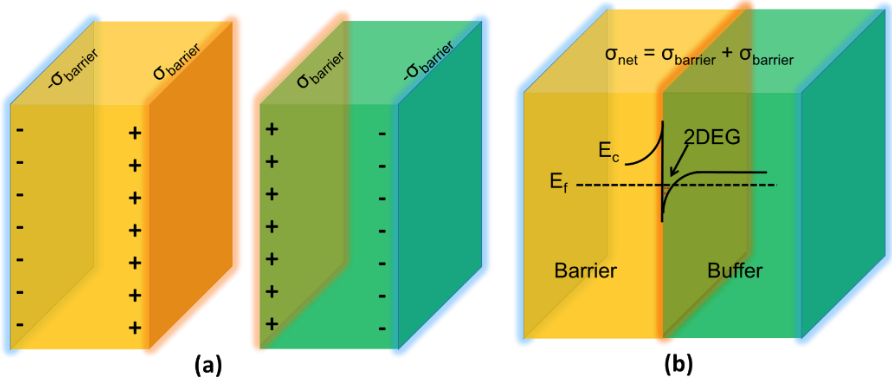

Figure 1.7: *Polarization charge in 2DEG at heterointerface, (a) Polarization charge in barrier layer ($\sigma_{barrier}$) and buffer layer (σ_{buffer}), (b) A net positive charge (σ_{net}) is produced at the contact when all the polarizations are added together.*

When these electrons congregate at the interface under the electrostatic force of positive net polarization difference, a 2DEG is created because of the conduction band notch below the fermi energy level at the MgZnO/ZnO heterojunction.

1.7.3. Alloys of ZnO: CdZnO and MgZnO

Structural Properties:

Under typical ambient conditions, the two lattice forms of ZnO that are most thermodynamically stable are the hexagonal wurtzite lattice [43] and the cubic zinc blende lattice [44]. Its iconicity, which lies between covalent and ionic materials, is the cause of this. At room temperature (RT), the lattice parameters of the hexagonal wurtzite ZnO are a = 3.25 and c = 5.20 [45]. On the other hand, the rocksalt structure of MgO and CdO is thermodynamically stable, with lattice parameters a = 4.216 and 4.689, respectively. Figure 1.8 illustrates how alloying MgO and CdO over 35% in ZnO causes phase segregation in MgZnO and CdZnO [46, 47].

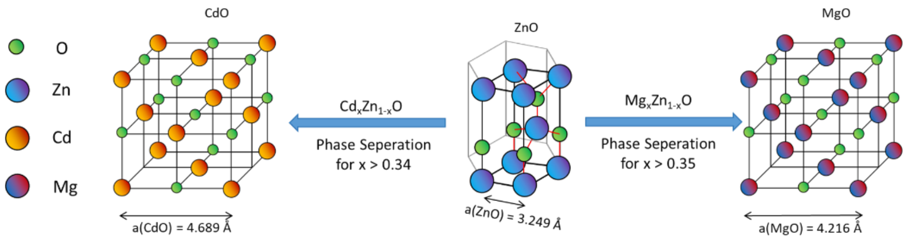

Figure 1.8: *Schematic illustration of ZnO, MgO, and CdO lattice structures with* $Cd_xZn_{1-x}O$ *and* $Mg_xZn_{1-x}O$ *phase segregation limits.*

The alloying of MgO and CdO in ZnO results in an increase in the lattice constant of the alloyed $Mg_xZn_{1-x}O$ (a = 3.248 (at x = 0.05) to 3.261 (at x = 0.3)) [47, 48] and $Cd_xZn_{1-x}O$ (a = 3.271 (at x = 0.05) to 3.378 (at x = 0.3)) [41, 47]. Because the lattice parameter of CdZnO rises more quickly than that of MgZnO, the straining of the MgZnO barrier layer in the MgZnO/CdZnO heterostructure is tensile rather than compressive, as in the MgZnO/ZnO heterostructure. This phenomenon increases the net polarization in the MgZnO barrier layer by causing the orientation of the P_s of the MgZnO layer to add up with the P_z due to tensile straining. As a result, the MgZnO/CdZnO heterointerface's 2DEG density rises in comparison to the

MgZnO/ZnO heterostructure's, increasing the net polarization difference.

Electrical Properties:

At room temperature, ZnO has a straight band gap of 3.43 eV [42], making it one of the materials with a large bandgap. High frequency and high-power applications are consequently allocated. ZnO's bandgap may be changed by alloying it with MgO and CdO. A reduction in the energy bandgap of the resulting $Cd_xZn_{1-x}O$ alloy ($3.37 - 2.28x + 0.95x^2$) [49] and an increase in the energy bandgap (E_g) of the resulting $Mg_xZn_{1-x}O$ alloy ($3.37 + 2.145x$) [50] are the results of alloying CdO in ZnO. After achieving the maximum Mg concentration, the buffer layer's CdZnO provides the ability to increase the ΔE_c value without generating phase segregation in the barrier layers of MgZnO, as the ΔE_c value is directly impacted by the difference between the energy bandgaps of the barrier and buffer layers. Compared to the MgZnO/ZnO heterostructure, the MgZnO/CdZnO heterostructure offers the possibility of achieving larger n_s values since an increase in ΔE_c is directly related to an increase in n_s.

1.7.4. MgZnO/CdZnO HEMT as HMI Sensors:

The gate terminal voltage modulates the connection between the source and drain terminals of the 2DEG channel in MgZnO/CdZnO-based HMI sensors. The gate is exposed to the analyte for sensing applications; that is, the reaction takes place at the gate area resulting in charges variation, which causes 2DEG to modulate. This method is simple, fast, and accurate for detecting HMIs. In contrast to the fluorescent sensing procedure, which requires human inspection and makes it difficult to accurately identify, store, or communicate the sensing data, the observed sensing response may also be readily measured, sent, and saved [51]. The lack of selectivity towards certain

HMIs is the sole disadvantage of MgZnO/CdZnO HEMT sensors; this may be addressed by functionalizing the target HMI to modify the surface at the gate area.

1.8. Aim and Objectives

The primary objective of this thesis research is to enhance the sensitivity and selectivity of pristine and metal-functionalized WS_2 and CVD-grown 2D MoS_2 materials towards Pb^{2+} and Hg^{2+} ions. To achieve this overarching goal, the following specific objectives are pursued in this thesis work:

- Preparation of the active/sensing layer of the sensor, tailored materials consisting of hydrothermally grown WS_2 and CVD-grown MoS_2. Subsequently, the fabrication of the interdigitated electrode device and material functionalization for sensing of HMIs using TMD material as the active layer.
- Investigation of morphological and structural properties of the grown material/active layer using different characterization techniques such as field emission scanning electron microscopy (FESEM), energy dispersive X-ray (EDX), X-ray photoelectron spectroscopy (XPS), X-ray diffraction (XRD), Raman, atomic force microscopy (AFM), etc.
- Study of the sensing characteristics using the indigenously developed sensing setup. The repeatability, selectivity, and long-term stability study of the sensors are undertaken.
- Simulation of the MgZnO/CdZnO (MCO) HEMT using Silvaco-TCAD, and model validation against existing literature. The simulation used heterostructure parameters developed with a dual ion beam sputtering (DIBS) system. Subsequently, the fabrication of MCO HEMT using DIBS system will be performed.
- Finally, to improve detection limits and stability, the functionalization of the gate region of the fabricated MCO HEMT

with a 2D-TMD material will be performed to enable sensing of HMIs and sensing performance will be evaluated.

1.9. Organization of the Thesis

Chapter 1 encompasses a concise review of the current literature, providing insights into the motivation behind the research and an exploration of existing HMI sensors along with their operational principles. Furthermore, this chapter delves into a detailed discussion of the inherent properties of WS_2, MoS_2 materials, and MgZnO/CdZnO HEMT assessing their applicability in HMI sensing applications.

Chapter 2 describes an extensive discussion on sensor fabrication, characterization and the investigation of sensing performance. Starting with the substrate selection, this chapter provides a thorough discussion on the deposition techniques utilized for WS_2, 2D MoS_2 sensing layer formation and to fabricate MCO HEMT. The chapter also discusses various characterization techniques, involving analyses of crystallinity, surface morphology, topology and other properties of the sensing layer.

Chapter 3 presents a simple hydrothermal approach for synthesizing silver (Ag)-loaded WS_2 nanorods. The WS_2 nanorods were incorporated with varying weight percentages of Ag (1%, 2%, and 4%). A detailed investigation is carried out on both pristine WS_2 and Ag-loaded WS_2 with different weight percentages to evaluate their performance in sensing Pb^{2+} ions. Additionally, comprehensive analyses are provided on the structural, morphological, and elemental properties of both pristine and Ag-loaded WS_2 samples.

Chapter 4 presented a method to synthesize the uniform, large-sized and highly crystalline MoS_2 monolayer deposition via CVD on Si/SiO_2 substrate. In addition, this chapter also discusses the surface energy assisted wet transfer method which is suitable for 2D monolayer transfer without any cracks and defects with ease in handling. Moreover, this chapter also elaborates on the ultrasensitive nature of MoS_2 monolayer for Hg^{2+} ions.

Chapter 5 discusses MCO HEMT simulation using Silvaco-TCAD and its validation against established literature. An oxide-based high electron mobility transistor sensor is fabricated using optical lithography and a dual ion beam sputtering (DIBS) system, designed to detect trace amount of Hg^{2+} ions in water. MoS_2, synthesized via chemical vapor deposition, was transferred to the MCO HEMT gate using an energy-assisted wet transfer method, functionalizing the gate region specifically for Hg^{2+} ion detection.

Chapter 6 encapsulates a concise summary of the research conducted in the thesis and outlines potential avenues, and suggesting directions for continued research in this field.

1.10. References

[1] B. Radisavljevic, A. Radenovic, J. Brivio, V. Giacometti, A. Kis, “Single-layer MoS_2 transistors”, *Nature nanotechnology*, vol. 6, 147, 2011.

[2] L. Järup, “Hazards of heavy metal contamination” *British Medical Bulletin*, vol. 68, pp. 167-182, 2003.

[3] R. Singh, N. Gautam, A. Mishra, R. Gupta, “Heavy metals and living systems: An overview”, *Indian Journal of Pharmacology* vol. 43, pp. 246-253, 2011.

[4] A. Nigam, N. Sharma, S. Tripathy, M. Kumar, “Development of semiconductor based heavy metal ion sensors for water analysis: A review”, *Sensors and Actuators A: Physical*, vol. 330, 112879, 2021.

[5] D.P.R. Krabbenhoft, A. David, “Mercury Contamination of Aquatic Ecosystems”, *U.S. GEOLOGICAL SURVEY Fact Sheet* Version 1.0 (216), 95, 2013.

[6] C. E. Halim, J. A. Scott, H. Natawardaya, R. Amal, D. Beydoun, G. Low, “Comparison between acetic acid and landfill leachates for the leaching of Pb(II), Cd(II), As(V), and Cr(VI) from cementitious wastes”, *Environmental science & technology*, vol. 38, pp. 3977-83, 2004.

[7] S. E. Mason, T. P. Trainor, A. M. Chaka, “Hybridization-reactivity relationship in Pb(II) adsorption on α-Al_2O_3-water interfaces: A DFT Study”, *The Journal of Physical Chemistry C*, vol. 115, pp. 4008-4021, 2011.

[8] G.S. Shukla, R. L. Singhal, “The present status of biological effects of toxic metals in the environment: lead, cadmium, and manganese”, *Canadian journal of physiology and pharmacology*, vol. 62, pp. 1015-31, 1984.

[9] A. Walsh, G. W. Watson, “The origin of the stereochemically active Pb(II) lone pair: DFT calculations on PbO and PbS”, *Journal of Solid State Chemistry*, vol. 178, pp. 1422-1428, 2005.

[10] B. Bansod, T. Kumar, R. Thakur, S. Rana, and I. Singh, “A review on various electrochemical techniques for heavy metal ions detection with different sensing platforms”, *Biosensors and Bioelectronics*, vol. 94, pp. 443-455, 2017.

[11] C. Lin, et al., “Gradient-Based Colorimetric Sensors for Continuous Gas Monitoring”, *Analytical Chemistry*, vol. 90, pp. 5375-5380, 2018.

[12] A. Odobašić, I. Šestan, and S. Begić, “Biosensors for Determination of Heavy Metals in Waters”, *Intechopen*, 2019.

[13] M. B. Gumpu, S. Sethuraman, U. M. Krishnan, and J. B. B. Rayappan, “A review on detection of heavy metal ions in water – An electrochemical approach”, *Sensors and Actuators B: Chemical*, vol. 213, pp. 515-533, 2015.

[14] M. Asadnia, et al., “Mercury(II) selective sensors based on AlGaN/GaN transistors”, *Analytica Chimica Acta*, vol. 943, pp. 1-7, 2016.

[15] P. Bergveld, “Thirty years of ISFETOLOGY: What happened in the past 30 years and what may happen in the next 30 years”, *Sensors and Actuators B: Chemical*, vol. 88, pp. 1-20, 2003.

[16] M. J. Schöning, D. Tsarouchas, L. Beckers, J. Schubert, W. Zander, P. Kordoš, H. Lüth, “A highly long-term stable silicon-based pH sensor fabricated by pulsed laser deposition technique”, *Sensors and Actuators B: Chemical*, vol. 35, pp. 228-233, 1996.

[17] G. L. Long, and J. D. Winefordner, “Limit of Detection: A Closer Look at the IUPAC Definition”, *Analytical Chemistry*, vol. 55, pp. 712-718, 1983.

[18] U. Chadha, et al., “A review of the function of using carbon nanomaterials in membrane filtration for contaminant removal from wastewater”, *Materials Research Express.*, vol. 9, pp. 012003, 2022.

[19] S. Avasarala, S. Bose, “2D nanochannels and huge specific surface area offer unique ways for water remediation and adsorption: assessing the strengths of hexagonal boron nitride in separation technology”, *Functional Composite Mater*, vol. 4, pp.1, 2023.

[20] H. Shin, J. Guan, M.Z. Zgierski, K.S. Kim, C.T. Kingston, B. Simard, “Covalent functionalization of boron nitride nanotubes via reduction chemistry”, *ACS Nano*, vol. 9, pp. 12573-12582, 2015.

[21] Z. Tang, Z. Qiu, S. Lu, X. Shi, “Functionalized layered double hydroxideapplied to heavy metal ions absorption: A review”, *Nanotechnology Reviews*, vol. 9, pp. 800-819, 2015.

[22] R. Soltani, et al., “Novel bimodal micro-mesoporous Ni50Co50-LDH/UiO-66-NH2nanocomposite for Tl (I) adsorption,” *Arabian Journal of Chemistry*, vol. 14, pp.103058, 2021.

[23] Y. Ibrahim, A. Kassab, K. Eid, A.M. Abdullah, K.I. Ozoemena, A. Elzatahry, “Unveiling fabrication and environmental remediation of MXene-based nanoarchitectures in toxic metals removal from wastewater: Strategy and mechanism”, *Nanomaterials*, vol. 10, pp. 885, 2020.

[24] S. Chaiyo, E. Mehmeti, K. Žagar, W. Siangproh, O. Chailapakul, K. Kalcher, “Electrochemical sensors for the simultaneous determination of zinc, cadmium and lead using a Nafion/ionic liquid/graphene composite modified screen-printed carbon electrode”, *Analytica Chimica Acta*, vol. 918, pp. 26-34, 2016.

[25] Y. Teng, C. K. Singh, O. Sadak, N. Ahmad, S. Gunasekaran, “Electrochemical detection of mobile zinc ions for early diagnosis of prostate cancer”, *Journal of Electroanalytical Chemistry,* vol. 833, pp. 269-274, 2019.

[26] N. Huo, S. Yang, Z. Wei, et al., “Photoresponsive and Gas Sensing Field-Effect Transistors based on Multilayer WS_2 Nanoflakes,” *Sci Rep.*, vol. 4, pp. 5209, 2014.

[27] Jonathan N. Coleman et al., “Two-Dimensional Nanosheets Produced by Liquid Exfoliation of Layered Materials”, *Science*, vol. 331, pp. 568-571, 2011.

[28] M. Chhowalla, et al., “The chemistry of two-dimensional layered transition metal dichalcogenide nanosheets”, *Nature Chem*, vol. 5, pp. 263–275, 2013.

[29] C. Zhu, Z. Zeng, H. Li, F. Li, C. Fan, H. Zhang, “Single-Layer MoS2-Based Nanoprobes for Homogeneous Detection of Biomolecules”, *J. Am. Chem. Soc.,* vol. 135, pp. 5998-6001, 2013.

[30] T. Mimura, S. Hiyamizu, T. Fujii, and K. Nanbu, "A new field-effect transistor with selectively doped GaAs/n-AlxGa1-xAs heterojunctions," *Japa. J. Appl. Phy*., vol. 19, pp. L225, 1980.

[31] T. Mimura, "Development of high electron mobility transistor," *J. J. Appl. Phys.,* vol. 44, pp. 8263, 2005.

[32] M. A. Khan, J. Kuznia, J. Van Hove, N. Pan, and J. Carter, "Observation of a two-dimensional electron gas in low pressure metalorganic chemical vapor deposited GaN/AlxGa1−xN heterojunctions," *Appl. Phys. Lett.,* vol. 60, pp. 3027-3029, 1992.

[33] K. Ding, A. Vitaliy, I. Natalia, O. Ümit, M. Hadis, S. Emilis, and M. Arvydas, "High-Performance BeMgZnO/ZnO Heterostructure

Field-Effect Transistors," *Phys. Status Solidi RRL*, vol. 14, pp. 2000371, 2020.

[34] H. Tampo, K. Matsubara, A. Yamada, H. Shibata, P. Fons, M. Yamagata, H. Kanie, S. Niki, "High electron mobility Zn polar ZnMgO/ZnO heterostructures grown by molecular beam epitaxy," *J. Crystal Growth,* vol. 301, pp. 358-361, 2007.

[35] K. Koike, *et. al.,* "Piezoelectric carrier confinement by lattice mismatch at ZnO/Zn0.6Mg0.4O heterointerface," *J. J. Appl. Phys.,* vol. 43, p. L1372, 2004.

[36] K. Koike, *et al.,* "Ion-sensitive characteristics of an electrolyte-solution-gate ZnO/ZnMgO heterojunction field-effect transistor as a biosensing transducer," *J. J. Appl. Phy.,* vol. 46, p. L865, 2007.

[37] H.-A. Chin, *et al.,* "Two-dimensional electron gases in polycrystalline MgZnO/ZnO heterostructures grown by rf-sputtering process," *J. Appl. Phy.,* vol. 108, p. 054503, 2010.

[38] R. Singh, M. A. Khan, P. Sharma, M. T. Htay, A. Kranti and S. Mukherjee, "Two-dimensional electron gases in MgZnO/ZnO and ZnO/MgZnO/ZnO heterostructures grown by dual ion beam sputtering," *J. Phys. D: Appl. Phys.,* vol. 51, pp. 13LT02, 2018.

[39] H. Tampo, *et al.,* “Polarization-induced two-dimensional electron gases in ZnMgO/ZnO heterostructures,” *Appl. Phys. Lett.,* vol. 93, pp. 202104, 2008.

[40] J. Huso, H. Che, D. Thapa, A. Canul, M. McCluskey, and L. Bergman, "Phonon dynamics and Urbach energy studies of MgZnO alloys," *J. Appl. Phys.,* vol. 117, p. 125702, 2015.

[41] F. Benharrats, K. Zitouni, A. Kadri, and B. Gil, “Determination of piezoelectric and spontaneous polarization fields in quantum wells grown along the polar <0001> direction”, *Superlattices and Microstructures,* vol. 47, pp. 592-596, 2010.

[42] R. Singh, M. A. Khan, S. Mukherjee, and A. Kranti, “Role of Surface States and Interface Charges in 2DEG in Sputtered ZnO

Heterostructures”, *IEEE Trans. Electron Devices*, vol. 65, pp. 2850-2854, 2018.

[43] S. K. Pandey, S. K. Pandey, V. Awasthi, M. Gupta, U. P. Deshpande, and S. Mukherjee, “Influence of in-situ annealing ambient on p-type conduction in dual ion beam sputtered Sb-doped ZnO thin films”, *Appl. Phys. Lett.*, vol. 103, p. 072109, 2013.

[44] G. Lee, T. Kawazoe, and M. Ohtsu, “Room temperature near-field photoluminescence of zinc-blend and wurtzite ZnO structures”, *Appl. Surface Science,* vol. 239, pp. 394-397, 2005.

[45] H. Tampo, et al., “Determination of crystallographic polarity of ZnO layers”, *Appl. Phys. Lett.*, vol. 87, p. 141904, 2005.

[46] I. Takeuchi, W. Yang, K. Chang, M. Aronova, T. Venkatesan, R. Vispute, L. A. Bendersky, “Monolithic multichannel ultraviolet detector arrays and continuous phase evolution in MgxZn1-xO composition spreads”, *J. Appl. Phys*., vol. 94, pp. 7336-7340, 2003.

[47] Y. Zhu, G. Chen, H. Ye, A. Walsh, C. Moon, and S.-H. Wei, “Electronic structure and phase stability of MgO, ZnO, CdO, and related ternary alloys”, *Phys. Rev. B*, vol. 77, p. 245209, 2008.

[48] T. Makino, Y. Segawa, M. Kawasaki, A. Ohtomo, R. Shiroki, K. Tamura, T. Yasuda, H. Koinuma, “Band gap engineering based on MgxZn1− xO and CdyZn1− yO ternary alloy films”, *Appl. Phys. Lett.*, vol. 78, pp. 1237-1239, 2001.

[49] X. Wang, et al., “Band gap properties of $Zn_{1-x}Cd_xO$ alloys grown by molecular-beam epitaxy”, *Appl. Phys. Lett.,* vol. 89, 2006.

[50] J. Ye, S. Pannirselvam, S. Lim, J. Bi, X. Sun, G. Lo, K. L. Teo, “Two-dimensional electron gas in Zn-polar ZnMgO/ZnO heterostructure grown by metal-organic vapor phase epitaxy”, *Appl. Phys. Lett.,* vol. 97, p. 1908, 2010.

[51] F. Ren, S. J. Pearton, B. S. Kang, and B. H. Chu, B. H., “AlGaN/GaN High Electron Mobility Transistor Based Sensors for Bio-Applications”, *Biosensors for Health, Environment and Biosecurity,* Edited by P. P. A. Serra, InTech, pp. 540, 2011.

Chapter 2

Synthesis, Fabrication and Characterization Techniques

2.1. Introduction

The requirement for thin films has gained a lot of attention as a result of the reduction in the size of semiconductor devices [1]. Additionally, thin films have a wide range of uses in solar cells, sensors, photodiodes, and memristors, among other fields [2]. In particular, the remarkable functional characteristics of nanostructured thin films—which are closely related to their distinct morphology and surface chemistry—have made them significant. Both physical and chemical deposition techniques, each with unique benefits and drawbacks, can be widely used to manufacture nanostructured thin films. In this thesis, nanostructured sensing materials are deposited using chemical deposition methods (chemical vapor deposition and hydrothermal deposition), whereas metal electrodes and oxide deposition are deposited using physical deposition methods (DIBS and E-beam evaporation technique). In addition, this chapter also covers the various characterization tools employed for investigating sensing material surface morphology, crystal structure orientation, elemental analysis, porosity, and surface area calculation. Surface morphology analysis is conducted using optical microscopy, field emission scanning electron microscopy (FESEM), Crystal structural orientation is determined using techniques like X-ray diffraction (XRD), and elemental analysis is carried out through methods such as energy dispersive X-ray (EDX) or X-ray photoelectron spectroscopy (XPS) analysis. The hydrothermally and CVD-grown sensing layer is deposited onto interdigitated electrodes and gate region of oxide HEMT device employing a drop-casting and wet transfer method respectively. And the MgZnO/CdZnO HEMT has been fabricated by DIBS system. Subsequently, the sensor's performance is assessed. The subsequent sections will provide a detailed discussion of substrate selection and preparation, deposition methods, characterization tools, the process of transferring the sensing layer, and the evaluation of sensor performance.

2.2. Substrate Selection and Cleaning Process

Although the deposition process has a significant influence on the quality of the deposited thin-film, the substrate surface's composition and state are crucial for achieving better thin-film growth [3, 4]. Low surface roughness, low chemical reactivity, and strong mechanical strength are among the desired characteristics of the substrate.

A number of variables, including the type of application, cost, procedure, and device packaging, affect the substrate selection [5]. Silicon is employed for thin film deposition in this thesis. Before the film is deposited, the substrate must be thoroughly cleaned because contaminants on its surface can compromise the film's purity and adherence. The kind of substrate and the pollutants present determine the cleaning process.

2.2.1. Silicon (Si) Substrate Cleaning Procedure

The following steps outline the cleaning procedure for silicon substrates used in this thesis work:

1. Use a pipette blower to remove surface dust before starting the cleaning process.
2. Perform ultrasonic cleaning in diluted HF solution to eliminate native silicon dioxide from the wafer surface.
3. Rinse thoroughly with DI water to remove residual HF.
4. Conduct ultrasonic cleaning in diluted TCE solution to remove fingerprints or heavy residues from the wafer.
5. Rinse with DI water to ensure no TCE residues remain.

6. Use ultrasonic cleaning in acetone to eliminate organic contaminants on the wafer surface.
7. Rinse with DI water to wash away any acetone residues.
8. Perform ultrasonic cleaning in diluted isopropanol solution to dissolve any non-polar contaminants left on the wafer.
9. Rinse with DI water to remove isopropanol residues.
10. Dry the substrate by purging with high-purity nitrogen gas to eliminate any remaining water.

2.3. Synthesis and Deposition Tools

In this thesis, chemical deposition methods, including hydrothermal and chemical vapor deposition (CVD), are used to deposit the sensing layer. The facile hydrothermal method is employed for the synthesis of WS_2 nanostructures, while CVD technique is opted for the deposition of the MoS_2 mono/multilayer. While physical vapor deposition means are employed for both thin film deposition and contact formation. A dual ion beam sputtering (DIBS) system is utilized for depositing the oxide thin films for MgZnO/CdZnO HEMT fabrication. The details of these deposition systems and processes are discussed in the following subsections.

2.3.1. Hydrothermal Synthesis

Sir Roderick Murchison coined the word "hydrothermal" in the 19th century to refer to the process of rocks and minerals forming beneath the Earth's crust under high pressure and temperature in an aqueous environment [6]. In 1946, a huge single crystal of quartz was successfully deposited using the hydrothermal technique for the first time [7]. Since then, the hydrothermal process has developed into a practical and affordable way to produce a variety of nanostructures with distinct functions.

2.3.1.1. Principle

The hydrothermal process is a physical-chemical reaction that crystallizes water at temperatures and pressures more than 100 °C and

0.1 MPa, respectively. The hydrothermal approach makes use of water's basic characteristics, which change with temperature and pressure, including conductivity, density, and dielectric constant. Consequently, this action also modifies the solvent characteristics of water. Water's dielectric constant of 78 under ambient settings enables it to dissolve polar and ionic molecules. Water's dielectric constant, on the other hand, drastically drops with temperature, changing its solubility properties toward organic and non-polar species.

The two primary processes of the hydrothermal process are typically crystal nucleation and growth. The nucleation reaction rate is stronger at higher temperatures because supersaturated solutions occur, which encourages the creation of nuclei, according to the electrostatics theory. The degree of super-saturation in the solution has an inverse relationship with the nuclei's radius. The "Ostwald ripening" method provides a clear understanding of the crystal development process. High temperatures give the thermal energy or external energy needed to break beyond the nucleation barrier.

2.3.1.2. Instrumentation

High temperatures and pressures are critical factors in hydrothermal growth, requiring the reaction chamber or vessel to withstand these demanding conditions without experiencing structural or compositional changes. This specialized reaction vessel, commonly referred to as an "autoclave," operates under pressure levels determined by the temperature and degree of filling. Autoclaves are typically constructed from stainless steel due to their excellent mechanical strength and resistance to corrosion. Inside the stainless-steel autoclave, Teflon beakers are used to contain solvents and reagents, offering the advantage of a non-corrosive environment.

An ideal autoclave should possess the following characteristics:

- It must be chemically inert, resistant to acids, bases, and oxidizing agents.

- It should remain leak-proof during operation and withstand high temperatures and pressures.
- It should allow for easy mechanical handling and straightforward operation.
- It should have an appropriate shape and size, ensuring a uniform temperature gradient throughout.

2.3.1.3. Operations

In this thesis, a Teflon-lined stainless-steel autoclave was utilized for synthesizing various nanostructures via the hydrothermal method. The process begins by dissolving reagents and precursors in a specified amount of deionized (DI) water under continuous magnetic stirring. A measured quantity of either a salt solution or a surfactant is then added to the mixture. The prepared solution is transferred into the Teflon-lined stainless-steel autoclave, which is carefully sealed to ensure no leakage. The autoclave is subsequently heated to temperatures of 100°C or higher in a hot air oven for a predetermined duration, tailored to the specific application. After the reaction, the autoclave is allowed to cool naturally to room temperature. The resulting product is then centrifuged and thoroughly washed multiple times with DI water and ethanol to remove impurities and contaminants. Finally, the samples are calcined at a specific temperature for a set period to achieve the desired properties.

2.3.1.4. Applications

In recent years, the hydrothermal method has garnered significant attention for its versatility in synthesizing advanced materials with distinctive morphologies. Some notable applications include:

- Growth of single crystals.
- Fabrication of metal oxide nanostructures with tailored surface morphologies.
- Synthesis of novel compounds and carbon-based nanostructures.

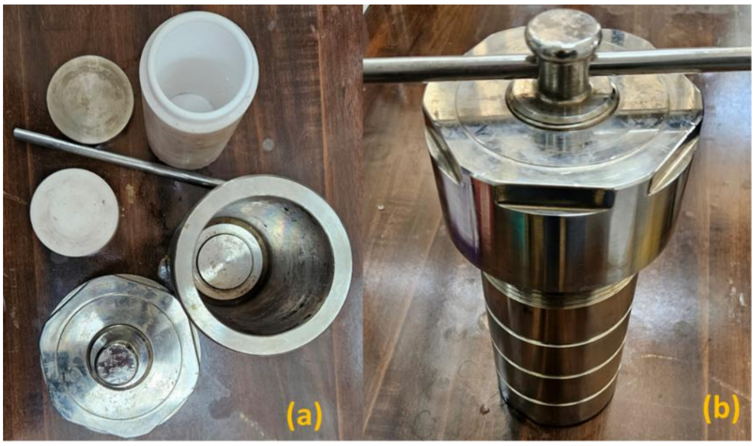

Figure 2.1: *Camera Image of (a) parts and (b) assembled Teflon lined Autoclave.*

2.3.2. Chemical Vapor Deposition

The Chemical Vapor Deposition (CVD) method originated in 1855 when tungsten (W) was first deposited by decomposing WCl_6 using H_2 as a carrier gas [8]. The first patent for the CVD process, designed to coat incandescent lamp filaments with carbon or metal for added strength, was filed in 1880. By 1890, the CVD method was utilized in the renowned Mond process to deposit pure nickel through the carbonyl process [9]. Today, the CVD process has evolved into a widely used technique for depositing industrial-grade thin films and finds extensive applications in electronics, optoelectronics, and biomedical fields.

2.3.2.1. Principle

The Chemical Vapor Deposition (CVD) process is a high-temperature synthesis technique in which chemical constituents react in the vapor phase. These reactions occur near or on a heated substrate within a quartz tube, leading to the deposition of a solid thin film. The fundamental steps of the CVD process include:

- Evaporation or sublimation of solid reactants and precursors.
- Transport of gaseous reactants to the heated substrate surface using an inert carrier gas.

- Adsorption of reactants onto the heated substrate surface at the gas-solid interface.
- Nucleation and crystallization through surface chemical reactions.
- Removal of gaseous byproducts via diffusion and convection.

2.3.2.2. Instrumentation

In this thesis, a QRYSTAL-1100-ATMOS chemical vapor deposition (CVD) system, procured from Quazar Technologies Pvt. Ltd., New Delhi, was used for depositing MoS_2 monolayers, as shown in Figure 2.2. This system operates on a single-phase power supply with specifications of 220 VAC, 40A, and 50 Hz. The outer framework, constructed from aluminium, provides the system with mechanical strength and rigidity. The furnace features a transparent quartz tube measuring 1160 mm in length, with outer and inner diameters of 48 mm and 45 mm, respectively. The system is capable of achieving a maximum temperature of 1150 °C. It incorporates twelve independently controlled heating zones, each 75 mm long, ensuring precise temperature control. Kanthal-A1 is used as the heating element, while N-type thermocouples serve as temperature sensors. The temperature ramp rates during growth are as follows: 100 °C/min up to 300 °C, 50 °C/min up to 600 °C, and 10 °C/min up to 900 °C. Cooling fans are installed at the back of the furnace to facilitate proper cooling. The system also includes a furnace stand and panel box, providing space for various controller assemblies and the CPU. The quartz tube can operate at a maximum temperature of 1100 °C, with a ramp rate of 5 °C/min at peak temperature. Four mass flow controllers (MFCs) are integrated into the system to precisely control the flow of inert gases (nitrogen, argon, hydrogen, helium) and oxygen within a range of 0–1000 sccm. These MFCs, regulated by pneumatic valves, ensure precise gas flow and system safety. A two-stage rotary pump is incorporated to create a vacuum inside the quartz tube, achieving a range of 10^{-2} mbar. A Pirani gauge is used to measure vacuum levels within the quartz tube, covering a range of 10^{-3} to 0.5 mbar. The system includes multiple safety features, such as purge and manual valves, alarmed pop-ups, and an auto-shutdown mechanism for the temperature controller if the pressure within the quartz tube exceeds safe limits or the lid is open. The CVD system is equipped with embedded control software, offering precise control over zone temperatures, process tube pressure (measured by Pirani and gauge sensors), MFC inlet pressure, gas flow setpoints, and actual flow rates. Additional features include real-time plotting, flush and flow shut-off status, pump and purge control, as well as recipe management for loading, editing, saving, and executing processes.

Figure 2.2: *Camera Image of Crystal CVD 1100-4 System.*

2.3.2.3. Application

Chemical vapor deposition (CVD) techniques offer several advantages, including:

- CVD is an effective method for depositing high-quality 2D transition metal dichalcogenides (TMDs) with precise control over size and thickness.
- It is also suitable for depositing various thin-film dielectrics, passivation layers, conductive oxides, and heat-resistant coatings.

- The CVD technique is utilized in the production of solar cells and high-temperature fiber composites.
- CVD provides a controlled approach for sulfurizing pre-deposited metals.
- It is widely used in device fabrication at the wafer scale.

2.3.3. Dual Ion Beam Sputtering (DIBS) System

The Dual Ion Beam Sputtering (DIBS) system is used to deposit semiconductor thin film stacks for creating MgZnO/CdZnO heterostructures [10]. The actual image of DIBS is shown in Figure 2.3 It is a physical vapor deposition technique commonly applied in the fabrication of electronic and optoelectronic devices, such as HEMT, LEDs, photodetectors, and photovoltaics, under ultrahigh vacuum conditions [10, 11]. The DIBS system is known for its ability to deposit high-quality thin films with precise elemental composition, strong adhesion to the substrate, reduced surface roughness, and the capacity to pre-clean substrates in situ before deposition. Additionally, it enables uniform deposition over large areas, making it ideal for large-scale photovoltaic cell production [12]. The DIBS system is equipped with two ion sources:

1) a ‘*primary ion*’ source for deposition and
2) a ‘*secondary ion*’ source for assisting.

The primary ion source sputters material from a target onto the substrate, enabling thin film deposition. The system allows mounting up to four different targets on a rotating, water-cooled target assembly, providing flexibility in material selection. The secondary ion source is utilized for pre-cleaning the substrate surface and minimizing island formation during deposition. The target assembly and primary ion source are aligned at a 45° angle, while the substrate holder and assist ion source are positioned at a 60° angle.

The DIBS system comprises two chambers: the deposition chamber (DPC) and the load-lock chamber (LLC). Deposition takes place in the DPC, whereas the LLC facilitates sample loading and unloading without disrupting the vacuum in the DPC. A gate valve separates the chambers, with two turbo pumps, supported by rotary pumps, maintaining the vacuum in both. Vacuum gauges monitor the pressure, which is maintained at approximately ~10^{-8} mbar. The DPC is constructed from stainless steel or Pyrex glass, chosen for their non-magnetic, corrosion-resistant, durable, and repairable properties.

The substrate holder is situated beneath the heater assembly, enabling temperature control from room temperature to 1000°C during annealing and deposition processes.

Figure 2.3: *Actual image of Dual Ion Beam Sputtering (DIBS) system, for high crystalline-quality deposition of semiconductors and dielectrics.*

A water chiller cools the deposition chamber, vacuum pumps, and target assembly to maintain optimal operating conditions. Deposition parameters, including gas pressure, composition, temperature, and RF (Radio Frequency) power, are automatically regulated for precision. In the DIBS system, plasma consisting of Ar^+ ions and electrons is generated using Kauffman Robinson ion sources. The primary ion source comprises a discharge chamber, grids, and a hollow-cathode neutralizer. Argon gas is ionized through inductive coupling within an RF-powered alumina or quartz chamber. Voltages applied to the three grids expel and focus Ar^+ ions, while the neutralizer ensures the ion beam remains neutral.

The assist ion source features an auto controller, power supplies (for keeper, emission, and discharge), and a hollow-cathode neutralizer. The keeper power supply initiates and heats the hollow cathode, enabling thermionic electron emission. The emission voltage adjusts the electron current from the cathode, while the discharge power supply provides the necessary voltage and current to generate the Ar^+ ion beam.

2.4. Characterization Tools

The instruments used for characterizing thin films and devices in this research are briefly defined in the subsequent sections.

2.4.1. X-Ray Diffraction Instrument

X-Ray diffraction (XRD) is a crucial technique for analysing the crystallinity, various phases, insights about strain, and preferred orientation of the crystal. In XRD, a parallelled beam of X-rays is directed at a sample which then diffracted by the crystalline phases within the sample according to Bragg’s Law, which is expressed as:

$$n\lambda = 2dsin\theta$$

here:

- **λ**: The wavelength of the incident X-ray beam.
- The interplanar spacing between atomic planes in the crystalline material.
- **θ**: The angle between the atomic planes and the incident X-ray beam.
- **n**: An integer denoting the order of interference.

Figure 2.4: *Camera image of Rigaku SmartLab automated multipurpose X-ray diffractometer.*

The intensity of the diffracted X-rays is measured as a function of the diffraction angle 2θ, and the resulting diffraction pattern is used to determine the crystal orientation of the sample. In a pure solid, atoms are arranged in a regular, periodic structure called a lattice. The specific interatomic distances and interactions within any crystalline lattice produce a characteristic XRD pattern, which can be used to identify the material's crystal structure [13]. These XRD patterns, comprising peak positions and diffracted beam intensities, offer detailed insights into the structural properties of the sample.

2.4.2. Field Emission Scanning Electron Microscopy (FESEM) and Energy Dispersive X-ray (EDX) Spectroscopy

2.4.2.1 FESEM

Field Emission Scanning Electron Microscopy (FESEM) is an advanced technique used to obtain highly detailed micrographs of a solid sample's surface by scanning it with high-energy electron beams [14]. The primary components of a FESEM system include a field emission electron gun, a lens system, electron detectors, and display systems such as cathode-ray tubes (CRTs). The electron gun generates electrons via field emission, which are then focused and accelerated toward the sample's surface using multiple electromagnetic lenses, all within a high-vacuum chamber. These energized electrons, typically ranging from 0.5 to 30 keV, interact with the sample surface, causing various electronic excitations. These interactions result in several signals, including backscattered electrons, secondary electrons, X-rays, photons, Auger electrons, cathodoluminescence, elastically and inelastically scattered electrons, unshattered electrons, and heat. Of these, secondary electrons and backscattered electrons are primarily used to create detailed FESEM images.

Figure 2.5: *Photographic image of ZEISS Supra55 field emission scanning electron microscope system.*

Secondary Electrons are emitted from the near-surface region of the sample (within 0–10 nm) and have low binding energy to the nucleus. These electrons originate from the outer shell of the sample and escape due to energy transferred by the incident high-energy electrons. Typically, they possess energies ranging from 0–50 eV, with most falling between 3–5 eV. Secondary electrons are key to generating high-resolution images, offering detailed insights into the surface morphology and fine structural details of the sample.

FESEM is widely employed for examining the morphological characteristics of samples and is regarded as a highly advanced microscopic technique, capable of magnifying images up to 100,000 times.

The key components of an FESEM system include:

1. **Electron Source (Electron Gun):** Produces the electron beam.
2. **Electron Condenser Lens:** Regulates the size and focus of the electron beam.
3. **XY Deflection Coils:** Precisely directs the electron beam over the sample surface.
4. **Electron Detectors:** Capture secondary and backscattered electrons to generate images.

These components are enclosed in a chamber maintained under ultra-high vacuum conditions. Unlike conventional electron sources, FESEM employs a Field Emission Gun (FEG) to achieve exceptionally high magnification.

Figure 2.6: *Representative camera image of ZEISS Supra55 Energy-dispersive X-ray spectroscopy (EDX) panel.*

The FEG uses a strong electric field, rather than thermal energy, to extract electrons from a sharp tungsten crystal or comparable material. In this study, a ZEISS Supra55 FESEM system was used to analyze the surface morphology of chalcogenide thin films. This system delivered high-resolution images that were essential for understanding the structural and morphological characteristics of the thin films, providing valuable insights for the research.

2.4.2.2 Energy-Dispersive X-Ray Spectroscopy (EDX)

Energy-dispersive X-ray spectroscopy (EDX), also known as Energy Dispersive X-ray Analysis (EDXA), is a powerful chemical microanalysis technique frequently used alongside Scanning Electron Microscopy (SEM). It enables the identification and quantification of the elemental composition in small regions of a sample, even as small as 1 micrometer (μm). The process works as follows:

1. **Electron Beam Bombardment**: A focused high-energy electron beam from the SEM is directed at the sample’s surface.
2. **X-Ray Emission**: When the electron beam interacts with the sample, it can eject electrons from the inner electron shells of the atoms. An outer-shell electron then fills the vacancy, emitting energy in the form of an X-ray.
3. **Characteristic X-rays**: The energy of the emitted X-ray is specific to the element it originated from. Each element has a unique atomic structure that produces a distinct X-ray "fingerprint."
4. **X-ray Detection and Analysis**: The EDX detector of the SEM system collects the X-rays and converts them into electrical signals. These signals are processed by a pulse processor and analyzer to determine the energy of each X-ray.

The key components of an EDX system include:

- **Electron Beam Source**: Produces the electron beam that interacts with the sample.
- **X-ray Detector**: Converts X-rays into electrical signals (commonly using a lithium-drifted silicon detector).
- **Pulse Processor**: Amplifies and processes the electrical signals from the detector.
- **Analyzer**: Analyzes the energy of each X-ray based on the processed signals.

By examining the spectrum of X-ray energy and the number of X-rays detected (counts), EDX software can identify and calculate the elements present in the sample. The relative abundance of each element is determined by the number of X-rays detected at its specific energy level. This data offers valuable insights into the elemental composition of the sample, making EDX an essential tool for fields such as material science, chemistry, biology, and forensics.

In this study, EDX (Zeiss Supra 55) was used to analyze the elemental composition of various elements within chalcogenide-based thin films.

2.4.3. Raman Spectroscopy Instrument

Raman spectroscopy is a commonly used technique for studying phonons, vibrational modes, low-frequency modes, and rotational modes. It is especially effective for molecular identification, as each molecule exhibits distinct chemical bonding and symmetry, producing unique Raman signatures. The technique is based on the phenomenon of Raman scattering.

When a material is exposed to light, the photons from the incident light interact with the material's molecular vibrations, resulting in both elastic and inelastic scattering. These interactions involve the transfer of energy between the incident photons and the atomic vibrations. The basic operation of Raman spectroscopy involves directing a laser beam onto the sample. Both Rayleigh and Raman scattered light are then collected from the illuminated area. The collected light is focused through an objective lens and passed through a monochromator to separate it into different wavelengths. A Notch filter is used to isolate the Raman scattered light and remove the elastic Rayleigh scattering. The Raman scattered light is carefully focused through a pinhole to ensure high signal quality and minimize background noise. The focused light is then sent into a spectrometer where the spectral components are optimized to enhance the signal, which is then detected by charge-coupled devices (CCD).

Figure 2.7: *Digital image of confocal raman microscope: LabRAM HR system.*

Raman spectroscopy is especially valuable for analyzing chalcogenide-based thin films. These materials, due to their unique bonding and structural characteristics, produce distinct Raman signatures that can be used to identify and characterize their composition, crystallinity, and phase transitions. Raman spectroscopy provides valuable insights into the quality and uniformity of chalcogenide thin films, helps detect structural defects or impurities, and monitors material changes during processes like annealing or sulfurization. This makes Raman spectroscopy an essential tool for the development and optimization of chalcogenide-based electronic and optoelectronic devices.

2.4.4. Atomic Force Microscopy Instrument

Atomic Force Microscopy (AFM) is an essential technique for characterizing chalcogenide-based thin films, providing crucial information about their morphology, thickness, and surface roughness. In this thesis, a Bruker Multimode 8-HR AFM was used to obtain high-resolution images of these thin films.

An AFM system utilizes several key components:

- **Laser Source:** Illuminates a microcantilever, with the reflected beam used for measurements.
- **Microcantilever:** A spring-mounted miniature arm with a sharp tip that interacts with the sample surface.
- **Piezoelectric Scanner:** Enables precise positioning of the cantilever in three dimensions (x, y, and z).
- **Photodetector:** A four-section device that monitors the reflected laser beam and detects its deflection.

AFM offers three primary operating modes, each suited for specific applications:

1. **Contact Mode:** The tip physically touches the sample surface, providing high-resolution imaging but potentially damaging delicate chalcogenide films.

   Tapping Mode (Preferred for Chalcogenides): The microcantilever oscillates near its resonance frequency while intermittently contacting the surface. This minimizes tip-sample interaction, making it ideal for studying soft materials like chalcogenides (This was the mode used in the thesis work).

2. **Non-Contact Mode:** The tip never physically touches the sample, but instead senses the short-range repulsive forces. This mode is suitable for ultra-soft materials.

In tapping mode, the AFM monitors the oscillation amplitude of the tip. As the tip interacts with the chalcogenide film, energy dissipation leads to a reduction in amplitude. To map the surface topography with minimal disturbance to the film, a feedback loop adjusts the tip-sample distance to maintain a consistent oscillation amplitude.

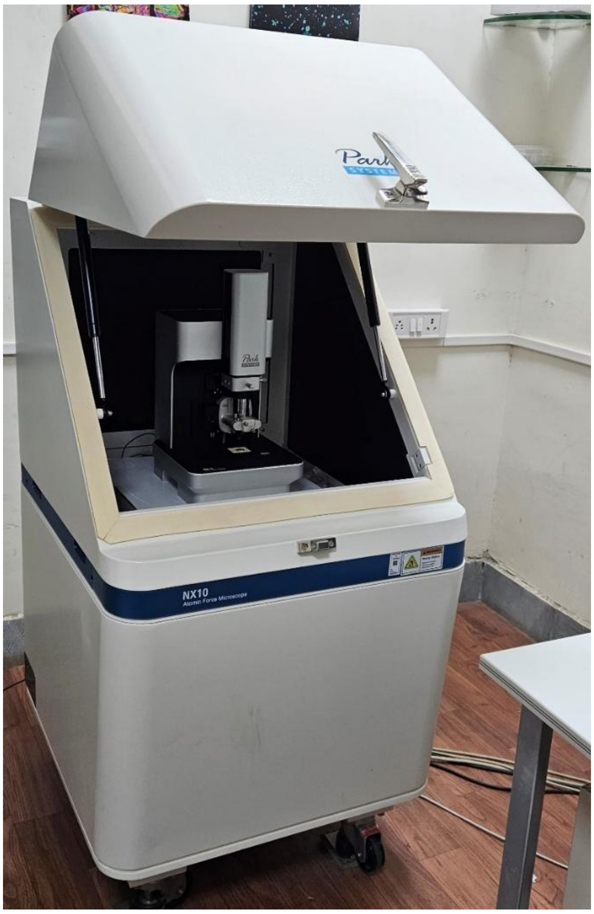

Figure 2.8: *Image of Park Systems NX10 atomic force microscopy.*

AFM's capabilities extend beyond just imaging. It allows researchers to probe various properties of chalcogenide thin films, including:

- **Surface Roughness:** AFM quantifies the variations in height across the film's surface, crucial for understanding its optical and electrical properties.
- **Grain Size and Morphology:** AFM images reveal the size and distribution of individual crystal grains within the film, influencing its overall performance.

- **Step Heights and Thickness Variations:** AFM measurements can determine the thickness of the entire film or identify variations in thickness across its surface.

This information is vital for optimizing the growth process of chalcogenide thin films and tailoring their properties for specific applications in photonics, electronics, and photovoltaics.

2.4.5. Optical Microscopy Instrument

In this thesis, a Leica upright metallurgical microscope (DM2700M) is used to examine the surface morphology of the deposited MoS_2 triangles via CVD, both before and after their transfer onto the interdigitated electrode device. This microscope offers versatile functionality, allowing for easy switching between universal white light (4500 K) LED illumination, brightfield, darkfield, differential contrast, and polarized light modes. It also provides a range of magnification options, including 5x, 10x, 20x, 50x, and 100x. Additionally, it features a robust incident light axis with a 4-position reflector turret, enabling a variety of observations such as brightfield, darkfield, differential contrast, and polarized light. The camera image from the microscope is shown in Figure 2.4.

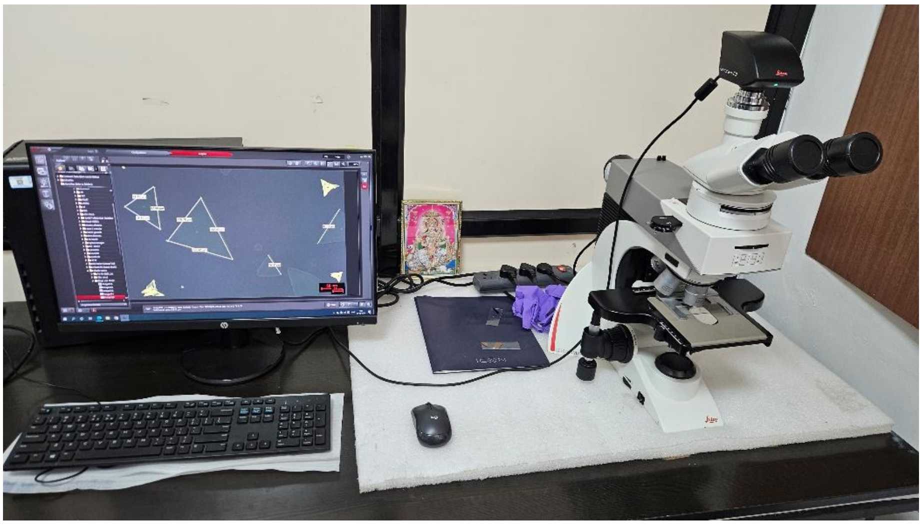

Figure 2.9: *Image of Leica upright metallurgical microscope (DM2700M).*

2.4.6. X-Ray Photoelectron Spectroscopy (XPS)

X-ray photoelectron spectroscopy (XPS) is a spectroscopic technique employed to determine the elemental composition, electronic, and chemical states of a material's surface, typically within a range of 1 to 10 nanometers. The fundamental principle of XPS is based on the photoelectric effect. When a solid material is irradiated with photons, in the case of XPS, monochromatic X-rays, under high vacuum conditions, the material's surface emits electrons (in XPS, these are core electrons of atoms) with specific kinetic energies.

The key components of XPS technology include a monochromatic X-ray source, an electron analyzer, and a high vacuum chamber. Figure 2.17 illustrates the fundamental operation of XPS.

The operation of the XPS technique involves several major steps:

- X-rays are generated by high-energy electrons colliding with a metal. These X-rays are then monochromatized through optics to produce photons with a consistent wavelength or energy.
- When monochromatic X-rays irradiate the sample surface, core electrons are emitted. Only those core electrons are emitted whose binding energy is less than the energy of the incident photons.
- The hemispherical energy analyzer comprises an outer sphere with a positive bias and an inner sphere with a negative bias. These are guided by two magnetic shields. This analyzer selectively allows photoelectrons with specific energy to pass through.
- Lenses are used to guide the photoelectrons into the hemispherical energy analyzer and apply voltage to control their velocity, allowing them to be transported to the detector through the analyzer.

- The detector quantifies the quantity of electrons that traverse the hemispherical energy analyzer and captures their respective energies to generate a spectrum.

In this thesis work, the Thermo Scientific K-Alpha instrument is employed to conduct XPS analyses of the samples.

2.5. References

[1] L. Risch, “The end of the CMOS roadmap new landscape beyond”, *Mater. Sci. Eng. C .*, vol.19, pp. 363-368, 2002.

[2] Y. Taga, “Recent progress of nanotechnologies of thin films for industrial applications”, *Mater. Sci. Eng. C .*, vol.15, pp.231-235, 2001.

[3] P. Panjan, A. Drnovšek, P. Gselman, M. Čekada, and M. Panjan, “Review of growth defects in thin films prepared by PVD techniques,” *Coatings*, vol. 10, no. 5, pp. 447, 2020.

[4] S. A. Chambers, “Epitaxial growth and properties of thin film oxides,” *Surface science reports*, vol. 39, no. 5-6, pp. 105-180, 2000.

[5] J. G. Ekerdt, Y. M. Sun, A. Szabo, G. J. Szulczewski, and J. White, “Role of surface chemistry in semiconductor thin film processing,” *Chemical reviews*, vol. 96, no. 4, pp. 1499-1518, 1996.

[6] A. Kopp Alves, C.P. Bergmann, F.A. Berutti, A. Kopp Alves, C.P. Bergmann, and F.A. Berutti, “Hydrothermal Synthesis”, *Novel Synthesis and Characterization of Nanostructured Materials*, pp.61-76, 2013.

[7] A.C.Walker, “Hydrothermal synthesis of quartz crystals”, *Journal of the American Ceramic Society*, vol.36, pp. 250-256, 1953.

[8] A.C. Jones, and M.L. Hitchman, “Overview of chemical vapour deposition”, *Chemical Vapour Deposition: Precursors, Processes and Applications*, vol. 1, pp. 1-36, 2009.

[9] D.M. Mattox, “Deposition processes”, *In The Foundations of Vacuum Coating Technology*, pp. 11-33, 2003.

[10] V. Awasthi, S. K. Pandey, S. Kumar, C. Mukherjee, M. Gupta, and S. Mukherjee, “Evaluation of band alignment and valence plasmonic features of DIBS grown Ga-doped $Mg_{0.05}Zn_{0.95}O$/CIGSe heterojunction by photoelectron spectroscopy”, *Journal of Physics D: Applied Physics*, vol. 48, no. 485305, pp. 1-12, 2015.

[11] P. Sharma, Aaryashree, V. Garg, and S. Mukherjee, “Optoelectronic properties of phosphorus doped p-type ZnO films grown by dual ion beam sputtering,” *Journal of Applied Physics*, vol. 121, no. 225306, pp. 1-9, 2017.

[12] B. S. Sengar, V. Garg, A. Kumar, S. Kumar, and S. Mukherjee, “Surface layer investigation of dual ion beam sputtered $Cu_2ZnSn(S,Se)_4$ thin film for open circuit voltage improvement,” *Journal of Physics D: Applied Physics*, vol. 51, no. 31LT01, pp. 18, 2018.

[13] M. Lee, “X-Ray diffraction for materials research: from fundamentals to applications,” *CRC Press*, 2017.

[14] K. Akhtar, S. A. Khan, S. B. Khan, and A. M. Asiri, “Scanning electron microscopy: Principle and applications in nanomaterials characterization,” *Springer International Publishing*, pp. 113-145, 2018.

Chapter 3

Ag-Loaded WS_2-Based Pb^{2+} Ion Detection in Water

3.1 Introduction

Heavy metal ions (HMIs) such as mercury (Hg^{2+}), lead (Pb^{2+}), manganese (Mn^{2+}), cobalt (Co^{2+}), zinc (Zn^{2+}), chromium (Cr^{3+}), cadmium (Cd^{2+}) contamination in water bodies has emerged as a severe environmental issue [1], as living organisms are exposed to these toxic elements in direct and indirect ways. The non-biodegradability and toxic characteristics of HMIs give rise to significant risks, particularly concerning human wellbeing [2-4]. In order to mitigate the adverse impacts of HMIs, it is vital to continuously monitor their presence across different sources of exposure such as water pollution, soil contamination, packaged food, air pollution, etc. Among these sources, water pollution stands out as a major threat to our ecosystem. For instance, elevated concentrations of HMIs and halide (F^-, Cl^-, and I^-) beyond permissible limits were reported in various underground and surface water bodies across different regions of India [5, 6]. Detecting and monitoring these toxic HMIs within water bodies are of utmost importance due to their swift accumulation and potential toxicity within the human body through drinking water and can cause severe diseases, such as carcinogenic effects, which can affect the central nervous system (CNS), kidneys, liver, skin, bones, and teeth [7-10]. Particularly, lead ion (Pb^{2+}*)* can enter water bodies from reservoirs that contain HMIs [11], and it is important to note that internal sources (service lines or valves) within drinking water distribution systems could also be found in older buildings with outdated plumbing systems. This situation can lead to the gradual release of Pb^{2+} without users being aware of the contamination [12]. Pb^{2+} is infamous for its adverse effects particularly on the children's behavior, growth, and cognitive functions [13, 14] In addition, it also causes severe damage to the human brain, immune system, liver, kidneys, and CNS [15, 16]. In order to safeguard public health from Pb^{2+} exposure through drinking water, the Word Health Organization (WHO) and Environmental Protection Agency (EPA) have established maximum permissible limits of Pb^{2+} at 10 ppb and 15 ppb, respectively [17].

Conventional techniques, such as atomic absorption spectroscopy (AAS) and inductively coupled plasma mass spectrometry (ICP-MS) [18, 19] are used to measure the Pb^{2+} concentration in the water bodies, which necessitate expensive laboratory procedures, utilizing sizable equipment and requiring extended processing durations. Therefore, demand for alternative, cost-effective, faster, and more readily available testing approaches is imperative to effectively tackle these aforementioned concerns.

The efficiency of accumulating target analytes and the overall performance of electrochemical sensors depend significantly on the choice of sensing materials. Various nano- materials, such as carbon-based materials (such as graphene oxides), boron nitride materials (BNMs), layered double hydroxides (LDHs), and MXenes, were explored for HMIs sensing applications due to their unique properties. However, these materials encountered various challenges, including low colloidal stability, limited sorption sites, poor dispensability, low chemical reactivity, low surface area, small particle size, inferior durability, and limited biocompatibility [20-25] Consequently, there is an urgent requirement for the development of an effective electrochemical sensing interface capable of detecting Pb^{2+} ions with high sensitivity.

The research community has recently displayed significant enthusiasm for transition metal dichalcogenides (TMDs) due to their extraordinary properties, which encompass a substantial surface-to-volume ratio, an adjustable bandgap, and exceptional catalytic behavior [26, 27]. These layered materials adopt a structure known as MX_2, in which “M” stands for transition metals, such as Ti, Mo, and W, whereas “X” comprises chalcogen elements from group VI- A, which encompass S, Se, and Te [28, 29]. This results in a range of material properties, spanning from insulator to metal. Within the layers, robust covalent bonds maintain cohesion, while between layers relatively weak van der Waals (vdW) forces facilitate effortless transitions [26, 27]. Among semiconducting TMDs, WS_2 captured notable interest due to its distinct properties. These encompass high surface area, remarkable electronic characteristics, excellent catalytic behavior, and enhanced stability [28-31].

In this chapter, we have employed a facile hydrothermal method to synthesize silver (Ag)-loaded WS_2 nanorods. These WS_2 nanorods were loaded with varying weight percentages (1%, 2%, and 4%) of Ag. Furthermore, we systematically investigated both pristine WS_2 and Ag-loaded WS_2 with different weight percentages for their capability in sensing Pb^{2+} ions. Additionally, thorough analyses of the structural, morphological, and elemental characteristics of both pristine and Ag-loaded WS_2 samples were conducted.

3.2. Experimental

3.2.1. Materials

All the chemicals and precursors are purchased from Sigma-Aldrich Chemical Pvt. Ltd., ensuring a purity level of 99.999%. These materials are used without further modification for the synthesis process. The materials employed in this study include sodium tungstate dihydrate ($Na_2WO_4.2H_2O$) and thiourea (CH_4N_2S) for the hydrothermal synthesis of WS_2. Sodium dihydrogen phosphate (NaH_2PO_4) and disodium hydrogen phosphate (Na_2HPO_4) are used to prepare the phosphate buffer solution (PBS). Additionally, other reagents, such as $Hg(NO_3)_2.H_2O$, $Cr(NO_3)_3.9H_2O$, $CuSO_4$, $Cd(NO_3)_2.4H_2O$, $Zn(NO_3)_2.6H_2O$, and $Pb(NO_3)_2$, are employed to prepare the ionic solutions containing respective metals for the purpose of sensing analysis. Moreover, silver chloride ($AgCl_2$) is used as a precursor for Ag loading on WS_2 nanostructures.

3.2.2. Synthesis of Sensing Material

The pristine and Ag-loaded WS_2 are synthesized via a facile hydrothermal process, as depicted in figure 3.1. Initially, 2.79 g of $Na_2WO_4.2H_2O$ is dissolved in 50 mL deionized (DI) water with a resistivity of 18 MΩ.cm, and no additional surfactants are introduced during the synthesis. Subsequently, 2.54 g of CH_4N_2S is introduced under a constant stirring. The resulting solution is then transferred into the teflon-lined stainless-steel autoclave (capacity, 100 mL). After sealing, the autoclave is placed inside a hot air oven and heated to 180 ºC, for 24 h, followed by natural cooling to room temperature. Following this, the precipitate undergoes centrifugation and is repeatedly washed with DI water. The resultant material is then dried at 80 ºC for 10 h. The whole process is repeated three times by adding different weight percentage (1, 2 and 4%) of $AgCl_2$. Finally, a small quantity of the acquired powder is mixed with 5 mL of ethanol. This blend is carefully deposited onto an interdigitated electrode (IDE). This entire procedure is replicated three times, with each iteration incorporating material fabricated at different weight percentage (1, 2 and 4%) of $AgCl_2$.

3.2.3. Sensing Material Characterization

Prior to investigating the structural, morphological, and elemental characteristics, the synthesized samples are preserved in a high vacuum desiccator containing silica gel. The crystalline phase composition of pure and Ag-loaded WS_2 is assessed through X-ray diffraction (XRD) analysis. This analysis employs a Rigaku Smart Lab Automated X-ray diffractometer, operated at 30 kV and 15 mA, utilizing Cu-Kα X-rays (λ = 1.54 Å) and a scanning rate of 2°/min. The morphology analysis is performed on a Sigma Supra 55 Carl Zeiss field emission scanning electron microscopy (FESEM) instrument. Furthermore, elemental analysis is conducted using X-ray photoelectron spectroscopy (XPS) with a ULVAC-PHI Quantra II system equipped with an AlKα source working at 1486.6 eV.

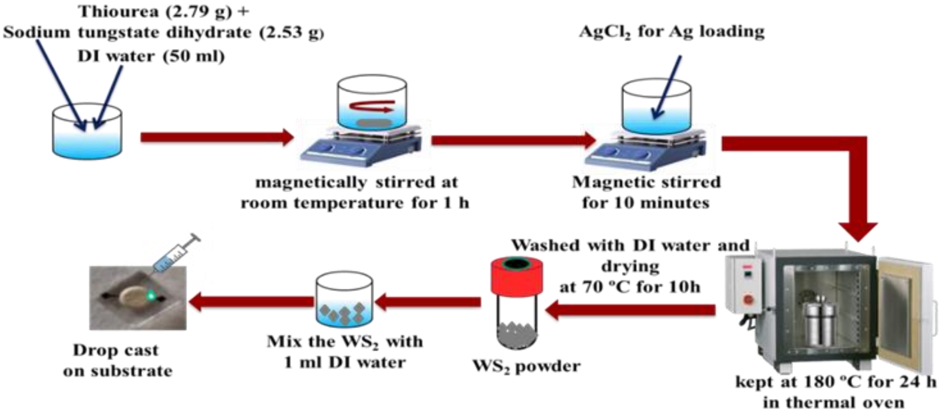

Figure 3.1: *Schematic of the hydrothermal synthesis process of the Ag-loaded WS_2 sensor.*

3.2.4. Device Fabrication and Water Sensing Measurement

The device consists of a glass substrate with a dimension of (7 mm × 7 mm × 2 mm) and a pair of interdigitated Ti/Pt (20/10 nm) electrodes on top of the glass substrate housing the sensing layer. The width of the electrodes and inter-electrode spacing are 50 and 25 µm, respectively. Each Pt electrode is connected to a contact pad (1 mm × 1 mm). The contact pads of the fabricated device are connected to the Keithley 2450 source meter, which is directly interfaced with a computer system for monitoring the electrical current of the sensing layer. The fabricated pristine and (1%, 2%, and 4%) Ag-loaded WS_2 nano-materials are used as a sensing layer. To measure the sensor current, +5 V bias voltage is applied across the contact pad via

Keithley 2450. Sensor response is measured by monitoring the change in the current voltage (*I–V)* characteristics, after WS_2 functionalization on the interdigitated electrodes by submerging the fabricated sensor in different heavy metal ion concentration solutions. To further validate the reproducibility of the sensor response, four samples were made for each sensing material, and the average response of these samples is reported in this work.

3.3. Results and Discussion

3.3.1. Surface Morphological Analysis

FESEM micrographs of pristine and Ag-loaded WS_2 reveal nanorods-like morphologies, as depicted in figure 3.2 (a-d). Interestingly, no major alteration is observed in the surface morphology of pristine WS_2 and WS_2 nanorods after Ag loading [33].

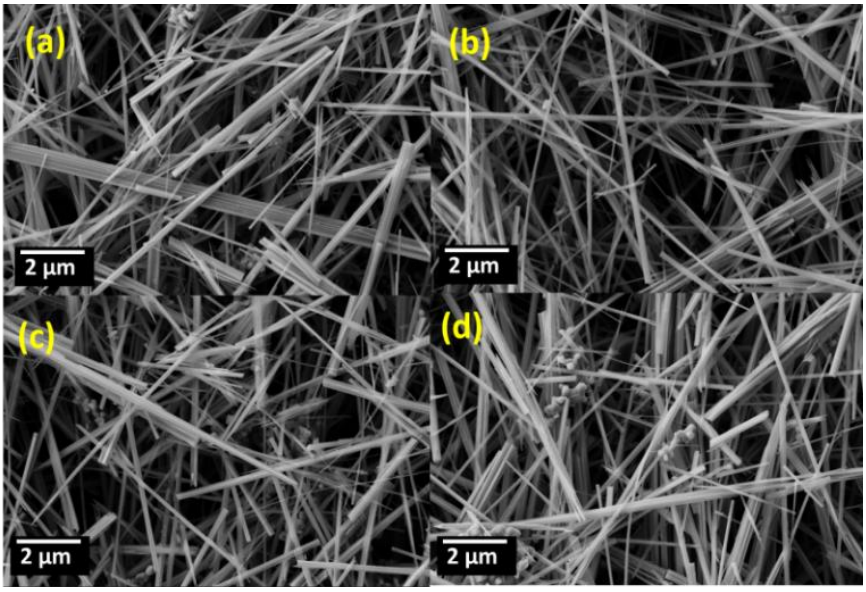

Figure 3.2: *FESEM image of (a) pristine and Ag-loaded WS_2 nanorods with varying Ag loading of (b) 1%, (c) 2%, and (d) 4%.*

3.3.2. XRD and Energy Dispersive X-ray (EDX) Analysis

The XRD spectra of the pristine, and Ag-loaded WS_2 are shown in figure 3.3 (a). The diffracted peaks of pristine WS_2 spectra are well matched with the expected crystalline hexagonal structure. All the diffraction peaks can be indexed to the WS_2 (P63/mmc space group, JCPDS no. 08-0237, 2H-WS_2) without any additional peaks which highlights the purity and crystallinity of the synthesized pristine and Ag-loaded WS_2 nanostructures, as illustrated in figure 3.3 (a) [34]. The XRD spectra show no key difference between the XRD patterns of pure WS_2 and Ag-doped WS_2; however, the Ag-loaded WS_2 samples exhibited reduced peak intensity compared to pristine WS_2. The peak intensity decreased with the increase in the Ag loading concentration, and it indicates the Ag substitution in WS_2 host lattice sites [35, 36].

XPS spectra of 2% Ag-loaded WS_2 nanorods are recorded for the investigation of the elemental composition and associated constituent element chemical states in the material. Figure 3.3 (b) shows the W $4f_{7/2}$ and W $4f_{5/2}$ peaks at 33.2 eV, and 35.2 eV corresponding to the W^{4+} oxidation state in WS_2 [37]. The S $2p_{3/2}$ and S $2p_{1/2}$ components of S 2p doublet are observed at 162.5 and 163.7 eV, respectively, and they are attributed to S^{2-} ions, as shown in figure 3.3 (c) [38, 39]. The binding energies of the element levels are consistent with W^{4+} and S^{2-} determined in WS_2 [37], further confirming the formation of the WS_2 phase. In addition, figure 3.3 (d) shows the Ag $3d_{5/2}$ and Ag $3d_{3/2}$ peaks at 366.2 and 373.2 eV, respectively, and it further confirms the Ag loading on the WS_2 surface [40]. It is noteworthy to mention that XPS is suitable for detecting the presence of Ag atoms on the WS_2 surface while it is challenging to predict the actual content of Ag atoms on the WS_2 surface.

3.3.3. Sensing Performance Analysis

To enable the detection of Pb^{2+} ions at various concentrations, a 100 parts per million (ppm) stock solution of Pb^{2+} ions was formulated by dissolving 2.39 mg of $Pb(NO_3)_2$ in 15 mL of PBS. The PBS is used, because it is non-toxic, has a pK_a value of 7.19, so have a high buffering capacity at 7 pH, and has very less variation with respect to temperature [41] compared to other buffers, such as *N* -(2-Acetamido)-2-aminoethanesulfonic acid buffer (ACES), phosphate buffer, tris (hydroxymethyl) aminomethane buffer, acetate buffer, and citrate buffer. The pH of the solutions was kept constant at 7 during the measurement.

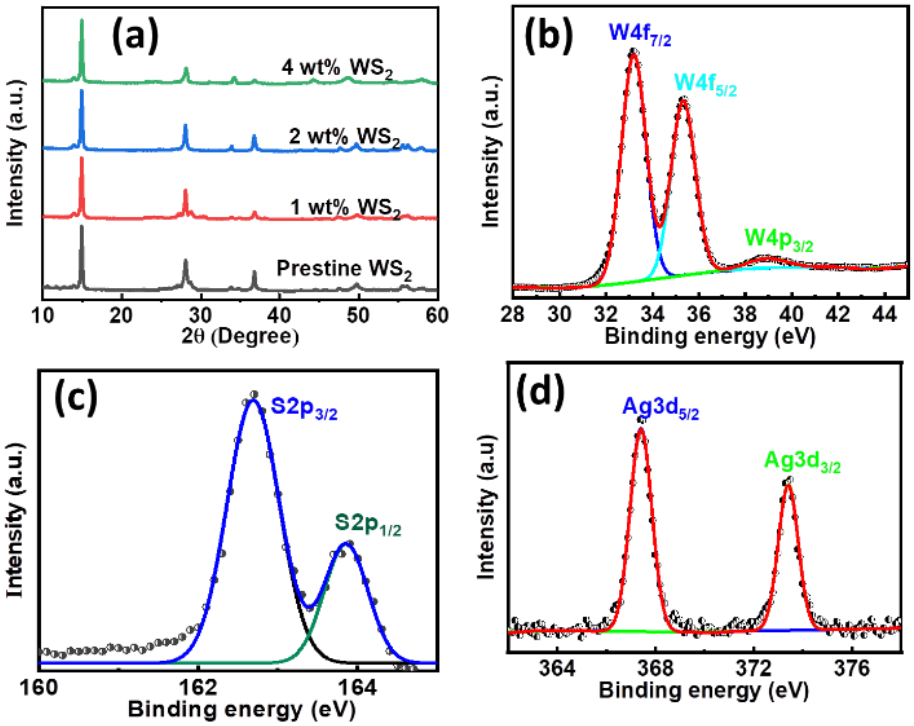

Figure 3.3: *(a) XRD spectra of pristine WS_2 with varying Ag wt%. High-resolution XPS spectra of (b) W 4f, (c) S 2p, and (d) Ag 3d for the 2 wt% Ag-loaded WS_2 nanorods.*

The subsequent solutions with lower Pb concentrations were obtained through dilution of the stock solution, following the solution dilution equation (1):

$$M_1V_1 = M_2V_2 \quad \ldots\ldots\ldots\ldots\ldots\ldots \text{(1)}$$

In this equation, M_1 and V_1 denote the concentration and volume of the stock solution, while M_2 and V_2 indicate the target concentration and volume of the solution needed. This formula helps calculate the volume of the stock solution or a higher concentration solution required to attain the desired Pb^{2+} ion concentration. By utilizing equation 1, solutions with varying Pb^{2+} ion concentrations, spanning from 10 ppm down to 1 parts per trillion (ppt), are prepared for sensing. The heavy metal ion sensing performance of pristine WS_2 and Ag-loaded WS_2 toward a 10-ppb Pb^{2+}ion concentration is examined. The sensing response of WS_2 sensors to 10-ppb Pb^{2+} ion exposure at room temperature is presented in figure 3.4 (a-d).

Notably, Ag-loaded WS_2 sensors exhibit higher sensing response values (2.48, 3.76, and 1.87 mA) compared to that by the pristine WS_2 (1.31 mA) due to the loading of Ag-adatoms on the WS_2 surface. The loaded Ag adatoms provide an additional active surface area on the WS_2 sensor sur- face, which enhances sensing performance. Interestingly, for 1 and 2-wt% loading of Ag adatoms on the WS_2 surface, the sensing response significantly increases from 2.48 to 3.76 mA, as shown in figure 3.4(b, c). However, further enhancement of Ag loading on the WS_2 surface reduces the sensing response to 1.87 mA, as it is evident in figure 3.4(d). This reduction may be due to a decrease in the catalytic efficiency of Ag atoms on the WS_2 surface [33].

The real-time sensing response of Pb^{2+} ions on the WS_2 functionalized IDEs is shown in figure 3.5(a). During the sensing process, the Pb^{2+} ion solution is introduced to the WS_2 functionalized surface, with the concentration of the ionic solution varying from 1 ppt to 100 ppm. At different concentrations of Pb^{2+} ions, the sensing response is observed for 60 s for each Pb^{2+} ion concentration, and a noticeable change in current is observed, indicating the successful detection of Pb^{2+} ions. The current increases significantly when the Pb^{2+} concentration is increased. The enhanced current upon metal ion addition is attributed to charge transfer, occurring through two primary mechanisms. First, ligand-to-metal charge transfer involves WS_2 as the ligand and heavy metal ions as metals. Second, WS_2 undergoes oxidation in the presence of a metal ion-containing solution.

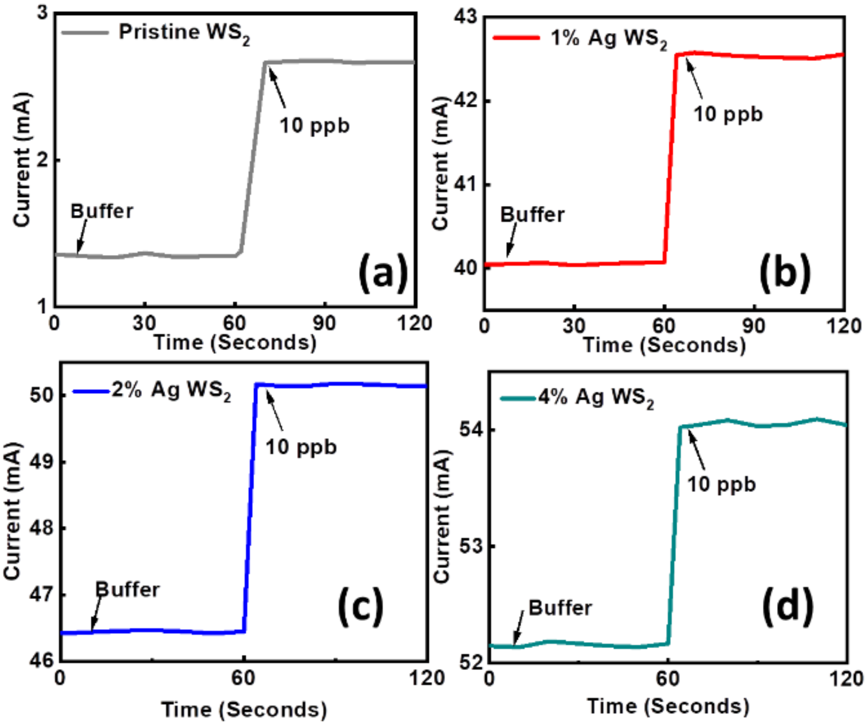

Figure 3.4: *Sensing performance of (a) pristine WS_2, (b) 1%, (c) 2% and (d) 4% Ag-loaded WS_2 for 10 ppb Pb^{2+} ions exposure.*

Sulfur's electronic configuration is $1s^22s^22p^63s^23p^4$, with valence electrons represented by $3s^23p^4$. Figure 3.5 illustrates the energy representation of valence electrons, showing a lone pair (LP) in the first p orbital. Transition metal chalcogenides exhibit sp^3 hybridization of chalcogens [42], and the electronic states post hybridization is shown in figure 3.5(b). In WS_2, tungsten forms a sixfold coordination with sulfur, creating a trigonal prismatic molecular bonding geometry. The metal contributes four electrons to bonding states, while sp^3 hybridized chalcogen provides two unpaired electrons and one LP for bonding, as shown in figure 3.5(b).

Consequently, formal charges of +4 and -2 are assigned to the transition metal and chalcogen, respectively [43]. Charge Density Difference (CDD) is surfaces, derived from DFT simulations [42], indicate that LP electrons extend toward the van der Waals (vdW) gap and terminate at the surface. Hence, upon drop-casting heavy metal ions onto WS_2 nanorods, WS_2 acts as a Lewis base (due to LP presence), and metal ions act as Lewis acids, forming $[A^{m+}n(WS_2)]B^{-}$ mn complexes. Here, A denotes the metal ion with an oxidation number of m, B is the anion associated with the AB salt, and n represents the stoichiometry. The creation of these complexes results in an increase in the system's current, as previously documented by [43] for various Lewis's acid-base complexes.

To assess the selectivity of WS_2 functionalized IDE towards Pb^{2+} ions and other heavy metal ions, the separate solution method is employed [44], and the results are shown in figure 3.5(c). In this method, the selectivity coefficient for separate solution approach (also termed as response ratio) $R_{Pb^{2+}, j}$ can be given by equation (2) [44]:

$$R_{Pb^{2+},j} = \frac{(|I_b - I_j|)C_{Pb^{2+}}}{(|I_b - I_{Pb^{2+}}|)C_j} \; .... \; (2)$$

where, I_b is the current when sensor is dipped in buffer solution, I_j is the current of interfering metal ions at concentration C_j, and $I_{Pb^{2+}}$ is the current at concentration $C_{Pb^{2+}}$.

Here, the sensing responses to interfering heavy metal ions and Pb^{2+} ions are measured at an identical concentration of 100 ppm. The calculated response ratio from equation (2) at 100 ppm concentration is presented in figure 3.5(c). It should be noted that a lower value of $R_{Pb^{2+}, j}$ indicates higher selectivity and less interference of other ions. figure 3.5(c) confirms that the sensor exhibits very high selectivity towards Pb^{2+} ions. This high selectivity can be primarily attributed to the strong interactions between Pb^{2+} and sulphur ions, as Pb^{2+} ions have a stronger affinity for sulfur. There is only slight interference observed from Hg^{2+} ions and Cu^{2+} ions.

The sensing parameters, such as the limit of detection (LoD) and sensitivity, are calculated by observing the current (I) vs. Pb^{2+} ion concentration plot, as presented in figure 3.6(a). The LoD is determined using the standard 3-sigma approach and calculated using the equation (3) [45]:

$$LoD = \frac{3\sigma}{m} \ldots\ldots\ldots\ldots\ldots\ldots\ldots\ (3)$$

where σ and m are the standard deviation (SD) of the least concentration of the Pb^{2+} ions and the sensitivity of the sensor, respectively. The sensitivity (m) of the sensor is calculated as the slope of the fitting curve, and it is equal to 819 μA/ppb.

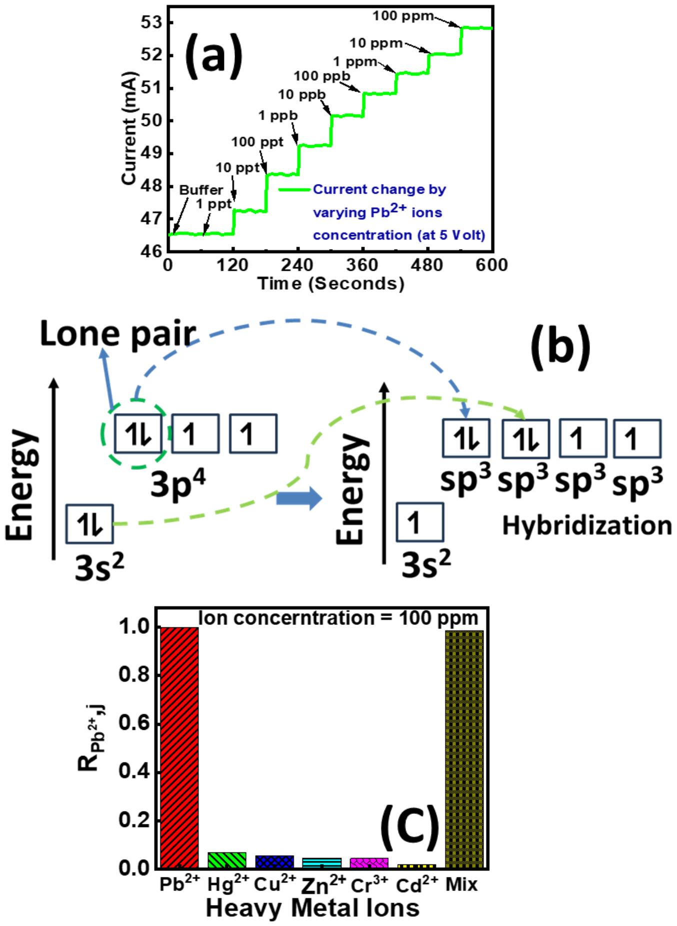

Figure 3.5: *(a) Real-time Pb^{2+} ion sensing, (b) The energy representation of valence electrons and, electronic states after hybridization of sulfur in WS_2, (c) Response ratio of the sensor for Pb^{2+} ions and other interfering heavy metal ions for selectivity analysis.*

The values of parameters such as σ and linear regression coefficient are derived from figure 3.6(a) as 0.0205 and 0.9997, respectively, and hence the LoD is determined from equation (3) as 75 ppt. The obtained LoD for Pb^{2+} ions on the WS_2 functionalized sensor is significantly lower than the standard limit set by WHO for drinking water standards for Pb^{2+} ions.

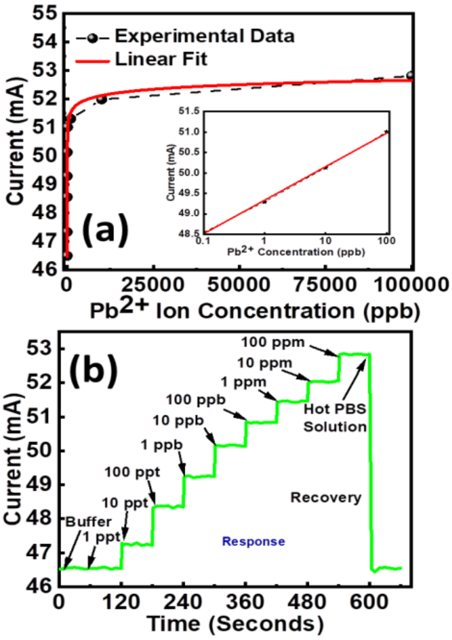

Figure 3.6: *(a) Sensor response and calibration curve for Pb^{2+} ion detection; and (b) response and recovery of the sensor.*

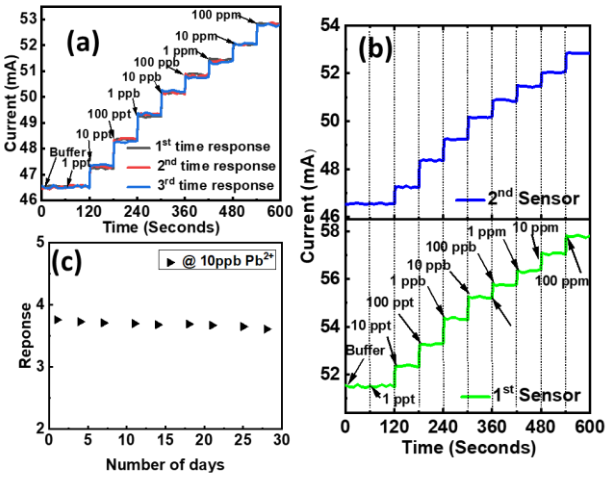

Figure 3.7: *(a) Repeatability, (b) Reproducibility, and (c) Long term stability of Pb^{2+} sensor.*

Then, the response and recovery of the sensor are shown in figure 3.6(b). In the sensing process, the Pb^{2+} ions are chemically adsorbed on the WS_2 surface by strong Pb-S bonding. Thus, in order to remove adsorbed Pb^{2+} ions from the surface of WS_2, more activation energy is required [46, 47]. Hence, the PBS is heated at 150 °C and applied to the sensor for rinsing. The developed sensor is rinsed in a hot PBS buffer for 100 s to recover from the bounded Pb^{2+} ions. In this process, the recovery is achieved at as high level as 99.35%.

Table 3.1: *Comparison of different sensing techniques for* Pb^{2+} *ions.*

S. No	Functionalized Material	Process	Sensitivity (µA/ppb)	LoD (ppb)	Response time	Ref.
1.	DMTD	SV	-	20.7	-	[48, 49]
2.	DMTD	SFM, SPM	-	0.5, 20	240 s	[48, 50]
3.	Bi/Graphite	ASV	0.0354	0.084	240 s	[51]
4.	Cu/Nafion/ Bi	DPV	0.2031	0.62	300 s	[52]
5.	Au NP	Colorimetry	-	30	-	[53]
6.	Hydrogel	LC resonator	-	0.0207	< 20 min	[54]
7.	**2 wt% Ag-WS_2**	**Electrochemical**	**819**	**0.075**	**< 5 s**	**Our work**

Glossary: SV- Stripping Voltammetry, ASV- Anodic Stripping Voltammetry, SFM - Spectrofluorometric, SPM – Spectrophotometry, DPV- Differential Pulse Voltammetry.

Subsequently, the repeatability, reproducibility and, long term stability of the interdigitated Pb^{2+} sensor based on WS_2 were also investigated. We observed a remarkably consistent sensing response from the sensors under identical operating conditions, as depicted in figure

3.7(a), The reproducibility of the developed sensor was further confirmed by creating an additional device, the sensing was performed under the same operating conditions, as shown in figure 3.7(b), The slight variation in response observed in the new sensor may be attributed to the internal resistance of the device. These results show that the sensor indicate excellent reproducibility. The long-term response of the fabricated sensor is extremely stable is shown in the figure 3.7(c), confirm that the sensor is an extremely promising candidate for a continuous real-time monitoring system.

The performance of the proposed WS_2-based sensor is compared with previously reported Pb^{2+} ion sensors and the results are shown in Table 3.1. The comparative analysis is conducted in terms of LoD, sensitivity and response time for Pb^{2+} ion detection in the sensors. It was observed that the WS_2 functionalized interdigitated sensor exhibited an excellent detection limit with high sensitivity and rapid response time compared to previously reported Pb^{2+} ion sensors.

3.4. Conclusion

In this chapter, the fabrication of pristine WS_2 and Ag-loaded WS_2 sensors using a facile hydrothermal method to enhance Pb^{2+} ion detection in water was carried out. The introduction of 2-wt% Ag adatoms on the WS_2 nanorods surface substantially enhances the sensing response, achieving approximately 2.8 times greater sensitivity compared to pris- tine WS_2. Notably, the device showed a rapid response time of <5 s and an excellent detection limit of 75 ppt. The proposed sensor demonstrates excellent selectivity toward Pb^{2+} ions. Moreover, the outstanding sensitivity observed in this sensor can be attributed to the formation of Pb–S complexes. The functionalization of WS_2 with Ag proved to be a pivotal factor influencing the sensor’s performance, with an optimal loading percentage of 2% yielding the highest sensitivity and selectivity. Overall, the exceptional performance of the sensor makes it a potential candidate for practical applications in environmental quality monitoring and toxic metal detection in water.

3.5. References

[1] Singh, R. K. Sharma, M. Agrawal, and F. M. Marshall, “Health risk assessment of heavy metals via dietary intake of foodstuffs from the wastewater irrigated site of a dry tropical area of India,” Food Chem. Toxicol., vol. 48, no. 2, pp. 611–619, Feb. 2010.

[2] H.-Y. Chang et al., “High-performance, highly bendable MoS2 transis- tors with high-K dielectrics for flexible low-power systems,” ACS Nano, vol. 7, no. 6, pp. 5446–5452, Jun. 2013.

[3] V. V. Atuchin, L. K. Asyakina, Y. R. Serazetdinova, A. S. Frolova, N. S. Velichkovich, and A. Y. Prosekov, “Microorganisms for biore- mediation of soils contaminated with heavy metals,” Microorganisms, vol. 11, no. 4, p. 864, Mar. 2023.

[4] I. Massas, O. Kairis, D. Gasparatos, D. Ioannou, D. Vatougios, and I. Zafeiriou, “Impaired soil health in agricultural areas close to Fe-Ni mines on Euboea Island, Greece, caused by increased concentrations of potentially toxic elements, and the associated impacts on human health,” Environments, vol. 10, no. 9, p. 150, Aug. 2023.

[5] S. Yu et al., “Rational design of carbonaceous nanofiber/Ni-Al layered double hydroxide nanocomposites for high-efficiency removal of heavy metals from aqueous solutions,” Environ. Pollut., vol. 242, pp. 1–11, Nov. 2018.

[6] Q. Wang, L. Peng, Y. Gong, F. Jia, S. Song, and Y. Li, “Mussel- inspired Fe3O4@Polydopamine(PDA)-MoS2 core–shell nanosphere asa promising adsorbent for removal of Pb^{2+} from water,” J. Mol. Liquids, vol. 282, pp. 598–605, May 2019.

[7] J. Deng et al., “Competitive adsorption of Pb(II), Cd(II) and Cu(II) onto chitosan-pyromellitic dianhydride modified biochar,” J. Colloid Interface Sci., vol. 506, pp. 355–364, Nov. 2017.

[8] S. Yu et al., “Boron nitride-based materials for the removal of pollutants from aqueous solutions: A review,” Chem. Eng. J., vol. 333, pp. 343–360, Feb. 2018.

[9] S. Yu et al., “Constructing sphere-like cobalt-molybdenum-nickel ternary hydroxide and calcined ternary oxide nanocomposites for efficient removal of U(VI) from aqueous solutions,” Chem. Eng. J., vol. 352, pp. 360–370, Nov. 2018.

[10] Y. Wu et al., “Environmental remediation of heavy metal ions by novel-nanomaterials: A review,” Environ. Pollut., vol. 246, pp. 608–620, Mar. 2019.

[11] S. Li, Z. Xu, X. Cheng, and Q. Zhang, “Dissolved trace elements and heavy metals in the Danjiangkou reservoir, China,” Environ. Geol., vol. 55, no. 5, pp. 977–983, Sep. 2008.

[12] X. Ma et al., “In situ monitoring of Pb^{2+} leaching from the galvanic joint surface in a prepared chlorinated drinking water,” Environ. Sci. Technol., vol. 52, no. 4, pp. 2126–2133, Feb. 2018.

[13] V. K. Gupta, I. Ali, T. A. Saleh, A. Nayak, and S. Agarwal, “Chemical treatment technologies for waste-water recycling—An overview,” RSC Adv., vol. 2, no. 16, pp. 3688–6380, 2012.

[14] L. Kong, L. Yan, Z. Qu, N. Yan, and L. Li, “β-cyclodextrin stabilized magnetic Fe3S4 nanoparticles for efficient removal of Pb(II),” J. Mater. Chem. A, vol. 3, no. 30, pp. 15755–15763, 2015.

[15] S. Bian et al., “One-pot synthesis of sulfur-doped graphene quantum dots as a novel fluorescent probe for highly selective and sensitive detection of lead(ii),” RSC Adv., vol. 6, no. 74, pp. 69977–69983, 2016.

[16] B. Zhang et al., “Facile and green fabrication of size-controlled AuNPs/CNFs hybrids for the highly sensitive simultaneous detection of heavy metal ions,” Electrochimica Acta, vol. 196, pp. 422–430, Apr. 2016.

[17] A. Nigam, V. S. Bhati, T. N. Bhat, S. B. Dolmanan, S. Tripathy, and M. Kumar, “Sensitive and selective detection of Pb2+ ions using 2,5-dimercapto-1,3,4-thiadiazole functionalized AlGaN/GaN high elec- tron mobility transistor,” IEEE Electron Device Lett., vol. 40, no. 12, pp. 1976–1979, Dec. 2019.

[18] M. T. Rahman et al., “Graphene oxide-silver nanowire nanocomposites for enhanced sensing of Hg2+,” ACS Appl. Nano Mater., vol. 2, pp. 4842–4851, Jul. 2019.

[19] M. Hu, H. Tian, and J. He, “Unprecedented selectivity and rapid uptake of CuS nanostructures toward Hg(II) ions,” ACS Appl. Mater. Interfaces, vol. 11, no. 21, pp. 19200–19206, May 2019.

[20] U. Chadha et al., “A review of the function of using carbon nanomaterials in membrane filtration for contaminant removal from wastewater,” Mater. Res. Exp., vol. 9, Jan. 2022, Art. no. 012003.

[21] S. Avasarala and S. Bose, “2D nanochannels and huge specific surface area offer unique ways for water remediation and adsorption: Assessing the strengths of hexagonal boron nitride in separation technology,” Funct. Compos. Mater., vol. 4, no. 1, p. 5, Apr. 2023.

[22] H. Shin, J. Guan, M. Z. Zgierski, K. S. Kim, C. T. Kingston, and B. Simard, “Covalent functionalization of boron nitride nanotubes via reduction chemistry,” ACS Nano, vol. 9, no. 12, pp. 12573–12582, Dec. 2015.

[23] Z. Tang, Z. Qiu, S. Lu, and X. Shi, “Functionalized layered double hydroxide applied to heavy metal ions absorption: A review,” Nanotech- nol. Rev., vol. 9, no. 1, pp. 800–819, Sep. 2020.

[24] R. Soltani et al., “Novel bimodal micro-mesoporous Ni50Co50- LDH/UiO-66-NH2 nanocomposite for Tl(I) adsorption,” Arabian J. Chem., vol. 14, no. 4, Apr. 2021, Art. no. 103058.

[25] Y. Ibrahim, A. Kassab, K. Eid, A. M. Abdullah, K. I. Ozoemena, and A. Elzatahry, “Unveiling fabrication and environmental remediation of MXene-based nanoarchitectures in toxic metals removal from wastew- ater: Strategy and mechanism,” Nanomaterials, vol. 10, no. 5, p. 885, May 2020.

[26] S. Chaiyo, E. Mehmeti, K. Žagar, W. Siangproh, O. Chailapakul, and K. Kalcher, “Electrochemical sensors for the simultaneous determina- tion of zinc, cadmium and lead using a Nafion/ionic liquid/graphene composite modified screen-printed carbon electrode,” Analytica Chim. Acta, vol. 918, pp. 26–34, Apr. 2016.

[27] Y. Teng, C. K. Singh, O. Sadak, N. Ahmad, and S. Gunasekaran, “Elec- trochemical detection of mobile zinc ions for early diagnosis of prostate cancer,” J. Electroanal. Chem., vol. 833, pp. 269–274, Jan. 2019.

[28] N. Huo, S. Yang, Z. Wei, S.-S. Li, J.-B. Xia, and J. Li, “Photorespon- sive and gas sensing field-effect transistors based on multilayer WS2 nanoflakes,” Sci. Rep., vol. 4, no. 1, p. 5209, Jun. 2014.

[29] J. N. Coleman et al., “Two-dimensional nanosheets produced by liquid exfoliation of layered materials,” Science, vol. 331, pp. 568–571, Feb. 2011.

[30] M. Chhowalla, H. S. Shin, G. Eda, L.-J. Li, K. P. Loh, and H. Zhang, “The chemistry of two-dimensional layered transition metal dichalcogenide nanosheets,” Nature Chem., vol. 5, no. 4, pp. 263–275, Apr. 2013.

[31] C. Zhu, Z. Zeng, H. Li, F. Li, C. Fan, and H. Zhang, “Single-layer MoS2-based nanoprobes for homogeneous detection of biomolecules,” J. Amer. Chem. Soc., vol. 135, no. 16, pp. 5998–6001, Apr. 2013.

[32] C. Patel et al., “S, N co-doped carbon dot-functionalized WO3 nanos- tructures for NO2 and H2S detection,” ACS Appl. Nano Mater., vol. 5, no. 2, pp. 2492–2500, Jan. 2022.

[33] C. Patel, S. Chaudhary, V. K. Verma, M. Dubey, S. Sriram, and S. Mukherjee, “Photoactivated Pd-loaded WO3 for enhanced H2S sensing,” IEEE Sensors J., vol. 23, no. 12, pp. 12552–12558, Jun. 2023.

[34] W. Yang et al., “[001] preferentially-oriented 2D tungsten disulfide nanosheets as anode materials for superior lithium storage,” J. Mater. Chem. A, vol. 3, no. 34, pp. 17811–17819, 2015.

[35] R. S. Zeferino, M. B. Flores, and U. Pal, “Photoluminescence and Raman scattering in Ag-doped ZnO nanoparticles,” J. Appl. Phys., vol. 109, no. 1, Jan. 2011, Art. no. 014308.

[36] S. Mohammed Harshulkhan, K. Janaki, G. Velraj, R. S. Ganapathy, and S. Krishnaraj, “Structural and optical properties of Ag doped tungsten oxide (WO_3) by microwave-assisted chemical route,” J. Mater. Sci., Mater. Electron., vol. 27, no. 4, pp. 3158–3163, Apr. 2016.

[37] R. Jha and P. K. Guha, “An effective liquid-phase exfoliation approach to fabricate tungsten disulfide into ultrathin two-dimensional semicon- ducting nanosheets,” J. Mater. Sci., vol. 52, no. 12, pp. 7256–7268, Jun. 2017.

[38] V. V. Atuchin, V. G. Kesler, V. V. Ursaki, and V. E. Tezlevan, “Elec- tronic structure of HgGa2S4,” Solid State Commun., vol. 138, no. 5, pp. 250–254, May 2006.

[39] V. V. Atuchin, L. I. Isaenko, V. G. Kesler, and S. I. Lobanov, “Core level photoelectron spectroscopy of LiGaS2 and Ga–S bonding in com- plex sulfides,” J. Alloys Compounds, vol. 497, nos. 1–2, pp. 244–248, May 2010.

[40] Y. Luo, D. Zhang, and X. Fan, “Hydrothermal fabrication of ag-decorated MoSe2/reduced graphene oxide ternary hybrid for H2S gas sensing,” IEEE Sensors J., vol. 20, no. 22, pp. 13262–13268, Nov. 2020.

[41] K. Reineke, A. Mathys, and D. Knorr, “Shift of pH-value during thermal treatments in buffer solutions and selected foods,” Int. J. Food Properties, vol. 14, no. 4, pp. 870–881, Jul. 2011.

[42] A. V. Kolonov and J. Tominaga, Two-Dimensional Transition-Metal Dichalcogenides (Springer Series in Materials Science), vol. 239. Berlin, Germany: Springer, 2016.

[43] S. Lei et al., “Surface functionalization of two-dimensional metal chalco- genides by Lewis acid–base chemistry,” Nature Nanotechnol., vol. 11, no. 5, pp. 465–471, May 2016.

[44] A. Nigam, N. Sharma, D. Lobanov, A. Novikov, and M. Kumar, “Ultra- sensitive detection of mercury ions under UV illumination of MoS2 functionalized AlGaN/GaN transistor,” IEEE Trans. Electron Devices, vol. 67, no. 12, pp. 5693–5700, Dec. 2020.

[45] C. Patel et al., “Large and uniform single crystals of MoS2 monolayers for ppb-level NO2 sensing,” ACS Appl. Nano Mater., vol. 5, no. 7, pp. 9415–9426, Jun. 2022.

[46] A. Nigam, T. N. Bhat, V. S. Bhati, S. B. Dolmanan, S. Tripathy, and M. Kumar, “MPA-GSH functionalized AlGaN/GaN high-electron mobility transistor-based sensor for cadmium ion detection,” IEEE Sensors J., vol. 19, no. 8, pp. 2863–2870, Apr. 2019.

[47] A. Nigam et al., “Real time detection of Hg2+ ions using MoS2 functionalized AlGaN/GaN high electron mobility transistor

for water quality monitoring," Sens. Actuators B, Chem., vol. 309, Apr. 2020, Art. no. 127832.

[48] N. Vasimalai and S. A. John, "Spectrofluorimetric determination of picogram level Pb (II) using a dimercaptothiadiazole fluorophore," Spec- trochimica Acta A, Mol. Biomolecular Spectrosc., vol. 82, no. 1, pp. 153–158, Nov. 2011.

[49] Y. Wu, N. Bing Li, and H. Qun Luo, "Electrochemical determination of Pb(II) at a gold electrode modified with a self-assembled mono- layer of 2,5-dimercapto-1,3,4-thiadiazole," Microchimica Acta, vol. 160, pp. 185–190, Jan. 2008.

[50] M. Jamaluddin Ahmed, "Spectrophotometric determination of lead in industrial, environmental, biological and soil samples using 2,5- dimercapto-1,3,4-thiadiazole," Talanta, vol. 55, no. 1, pp. 43–54, Aug. 2001.

[51] R. T. Kachoosangi, C. E. Banks, X. Ji, and R. G. Compton, "Electro- analytical determination of Cadmium (II) and Lead (II) using an in-situ bismuth film modified edge plane pyrolytic graphite electrode," Anal. Sci., vol. 23, no. 3, pp. 283–289, Mar. 2007.

[52] S. Legeai and O. Vittori, "A Cu/Nafion/Bi electrode for on-site moni- toring of trace heavy metals in natural waters using anodic stripping voltammetry: An alternative to mercury-based electrodes," Analytica Chim. Acta, vol. 560, nos. 1–2, pp. 184–190, Feb. 2006.

[53] C. Zhao, G. Zhong, D.-E. Kim, J. Liu, and X. Liu, "A portable lab-on-a-chip system for gold-nanoparticle-based colorimetric detection of metal ions in water," Biomicrofluidics, vol. 8, no. 5, Art. no. 052107, Sep. 2014.

[54] C.-C. Yeh and Y.-J. Yang, "A portable miniaturized Pb^{2+} detector using ion-responsive hydrogel with wireless interrogation capability," in Proc. IEEE 30th Int. Conf. Micro Electro Mech. Syst. (MEMS), Jan. 2017, pp. 1056–1059.

Chapter 4

CVD-grown MoS_2 Monolayer based Ultrasensitive Hg^{2+} Ion Sensing in Water

4.1. Introduction

Water is a fundamental necessity for human existence, and the ecological importance of freshwater is steadily growing due to its scarcity and ongoing pollution. Among the array of water pollutants, heavy metal ions emerge as potent carcinogens, posing significant health hazards to humans due to their extreme toxicity. The urgent need for the advancement of sensors which can detect heavy metal ions (HMIs) in environmental systems is undeniable. Notably, mercury (Hg) garners attention as one of the most notorious toxic metals, even in trace amounts [1]. It is infamous for its ability to cause both chronic and acute poisoning. Prolonged or excessive exposure to mercury can lead to serious health complications, including, but not limited to, irreversible neurological damage, cancer, and debilitating movement disorders, all of which can potentially be life-threatening [1, 2]. To mitigate the risks of Hg^{2+} ions, it is crucial to maintain their concentrations below the recommended thresholds established by the World Health Organization (1 ppb) and the Environmental Protection Agency (2 ppb) [3, 4].

Substantial efforts have been made to detect trace levels of mercury using various analytical approaches. Among these approaches are optical analyses such as colorimetry and spectroscopy [3, 5], as well as electrochemical methods like voltammetry and amperometry [6, 7]. While these methods exhibit commendable sensitivity, they are often costly, time-consuming, complex, and dependent on laboratory settings, requiring specialized operators for analysis [8].

The sensing material affects the efficiency of detecting the targeted analyte and the performance of the electrochemical sensor. Numerous nanomaterials, including boron nitrides, carbon-based materials (like graphene and its oxides), MXenes, and layered double hydroxides, have been explored for HMI detection because of their distinctive properties [9-12]. Nevertheless, these materials face several drawbacks, such as lower stability, fewer adsorption sites, poor dispersibility, limited biocompatibility, reduced surface area, lower chemical reactivity, small particle size, and substandard durability [9-14]. Consequently, there is a pressing need for an effective electrochemical sensing device that can detect Hg^{2+} ions with excellent sensitivity.

Recently, two-dimensional transition metal dichalcogenides (TMDs) have gained significant research attention due to their outstanding optical and electronic properties [15]. There are many MoS_2-based mercury (Hg^{2+}) ion sensors that have been reported in the literature [16, 17, 18, 19, 20]. Different research groups have synthesized MoS_2 using different techniques, such as the hydrothermal process, exfoliation method, and chemical vapor deposition (CVD), for various sensing applications. For instance, D. S. Rana et al. [16] reported flower like MoS_2-rGO nanostructures with a limit of detection (LoD) of 320.94 ppb, and Mishra et al. [17] synthesized MoS_2 submicron flowers, reporting an improved LoD of 40.12 ppb. Further, P. Maiti et al. [18] synthesized MoS_2 nanoflakes and achieved a LoD of 0.126 ppb. Furthermore, A. Nigam et al. [19] functionalized AlGaN/GaN HEMT by hydrothermally grown MoS_2 to enhance the LoD up to 11.5 ppt and a sensitivity of 0.64 µA/ppb. Additionally, other research groups have also reported Hg^{2+} ion sensing using exfoliated MoS_2. For example, J. J. Luo et al. [20] and P. Li et al. [21] have demonstrated Hg^{2+} ion sensors using exfoliated MoS_2 with LoDs of 0.254 ppb and 5 ppb, respectively, with the later study reporting a response time of 8 seconds. The sensors fabricated with exfoliated and hydrothermally synthesized MoS_2-based sensors offer a low LoD, poor sensitivity and has large response time as discussed. The MoS_2 synthesized using both methods suffer from drawbacks such as low yield, inconsistent layer numbers, and small sized MoS_2 films or flakes [22, 23]. Furthermore, impurities introduced during the exfoliation process can degrade sensor performance, and, as with the both methods, controlling the number of layers and size of flakes/layers is challenging, resulting in limited reproducibility [24]. To overcome these limitations, we developed a Hg^{2+} ion sensor based on CVD-grown monolayer MoS_2. The CVD method provides significant advantages, including better uniformity, higher crystal quality, larger crystal sizes, controlled number of layers, and a greater surface-to-volume ratio [25]. The monolayer MoS_2 exposes a sulfur-rich surface with numerous active adsorption sites, making it highly sensitive for Hg^{2+} ion detection [26]. As a result, our fabricated sensor demonstrates exceptional sensitivity (957 µA/ppb), a fast response time of less than 4 seconds, and a remarkably low detection limit of 27.9 ppt, well below the WHO's 1 ppb limit for drinking water. The device also shows excellent recovery, achieving 99.25%.

4.2. Experimental

4.2.1. Materials

All the precursors and chemicals were procured from Alfa Aesar, with a 99.999% purity. They were used directly in the synthesis process without any additional modifications. The materials utilized in this research include molybdenum trioxide (MoO_3), ammonium hydroxide (NH_4OH, 25% solution), and NaCl for the synthesis of MoS_2. Na_2HPO_4 and NaH_2PO_4 were employed to prepare the phosphate buffer solution (PBS). Additionally, chemical precursors including $Hg(NO_3)_2 \cdot H_2O$, $Cr(NO_3)_3 \cdot 9H_2O$, $CuSO_4$, $Cd(NO_3)_2 \cdot 4H_2O$, $Zn(NO_3)_2 \cdot 6H_2O$, and $Pb(NO_3)_2$ were utilized to prepare ionic solutions containing the corresponding metal ions for sensing analysis.

4.2.2. Synthesis of Sensing Material

Using an atmospheric pressure CVD system (Quazar Technologies Pvt. Ltd.) equipped with individually controlled heating zones, a large and uniform MoS_2 layer is deposited onto SiO_2/Si substrates. Before the MoS_2 deposition, the SiO_2/Si substrate is prepared by cleaning it using ultrasonication in acetone $(CH_3)_2CO$, isopropanol (C_3H_8O), and deionized water for 15 minutes. The substrate is then dried with nitrogen (N_2) gas. To synthesize MoS_2, a solution process is utilized wherein MoO_3 powder is mixed in a 25% solution of ammonium hydroxide (NH_4OH). Initially, 0.2 g of MoO_3 precursor is dissolved in 10 mL of NH_4OH solvent. Subsequently, 0.05 g of NaCl is mixed into the NH_4OH-MoO_3 solution under constant magnetic stirring. To create a uniform layer of MoO_3, 0.5 microliters of a 20 milligram/milliliter solution are spin-coated onto a 1×1.5 cm^2 SiO_2/Si substrate at 3000 revolutions per minute for 1 minute. To remove any remaining solvent and ensure the MoO_3 seeds are evenly spread, the MoO_3-coated SiO_2/Si sample is heated in an oxygen atmosphere at 250 °C for 15 minutes. Additionally, the bare SiO_2/Si substrate is placed at the top, and the MoO_3-coated SiO_2/Si substrate (1×1.5 cm^2) is positioned in the bottom of the alumina boat, respectively, as shown in figure 4.1. In a separate alumina boat, 0.6 grams of sulfur is placed, also illustrated in figure 4.1. The alumina boat with sulfur is situated in upstream flow (i.e., the inlet side) of the Argon (Ar) carrier gas, while other boat containing both MoO_3-coated and uncoated SiO_2/Si sample is located in the downstream (i.e., the outlet side) flow of the Ar gas. After positioning the boats in different heating zones, the zone containing the SiO_2/Si substrate is heated to 300°C at a ramp rate of 30 °C/min, and then held at this temperature for 15 minutes while Ar flow rate is maintained at 1000 sccm. Next, the temperature of this heating zone is gradually increased to 800°C at a reduced ramp rate of 15°C/min to mitigate temperature overshooting, while a carrier gas (Ar) flow rate of 150 sccm is maintained. During the growth, oxygen gas is introduced at a flow rate of 2 sccm for a 10-minute dwell time. The temperature of the zone containing boat with sulfur is maintained at 180 °C throughout the growth period.

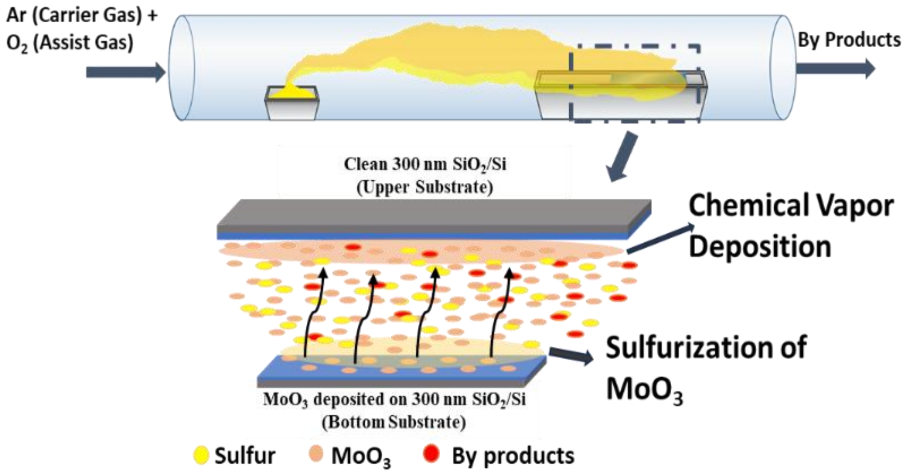

Figure 4.1: *Schematic illustrating the process of synthesizing* MoS_2 *by CVD system.*

4.2.3. Sensing Material Characterization

Before examining the diverse characteristics of the synthesized MoS_2, the samples are stored in glovebox having argon environment with silica gel to eliminate any moisture. The surface morphology of the MoS_2 layer following synthesis is examined using a Leica upright metallurgical microscope (DM2700M). To quantify the number of layers of the deposited MoS_2 sample, Raman spectroscopy (Horiba, LabRAM HR Evolution) was used.

4.2.4. Device Fabrication and Transfer Process of the MoS_2

The device comprises a glass substrate with dimensions of 0.7 cm × 0.7 cm × 0.2 cm and a set of IDEs consisting of a Ti/Pt (20/10 nm) stack positioned atop the glass substrate. The MoS_2 layer is placed on top of the IDE. The electrodes have a width of 50 µm and a spacing of 25 µm. The Pt electrode is connected to a contact pad measuring 0.1 cm × 0.1 cm.

The successful synthesis of MoS_2 is confirmed by optical microscopy and Raman spectra of the layer. Figure 4.2(a) shows the optical image of the MoS_2 layer after deposition on the Si/SiO_2 substrate, obtained with a Leica DM2700M upright metallurgical microscope. The deposited MoS_2 features large-sized monolayer crystals. Figure 4.2(b) depicts the Raman spectra of the synthesized layer. From the spectra, it can be observed that the E^1_{2g} (in-plane) and A_{1g} (out-of-plane) peaks are at 383.5 and 404.4 cm^{-1}, respectively. The variation in the position and intensity ratio of the E^1_{2g} and A_{1g} peaks is approximately 21 cm^{-1} and about 1, respectively. This confirms that the deposited MoS_2 is a monolayer with a exposed basal plane surface morphology, consistent with findings reported in the literature [27, 28].

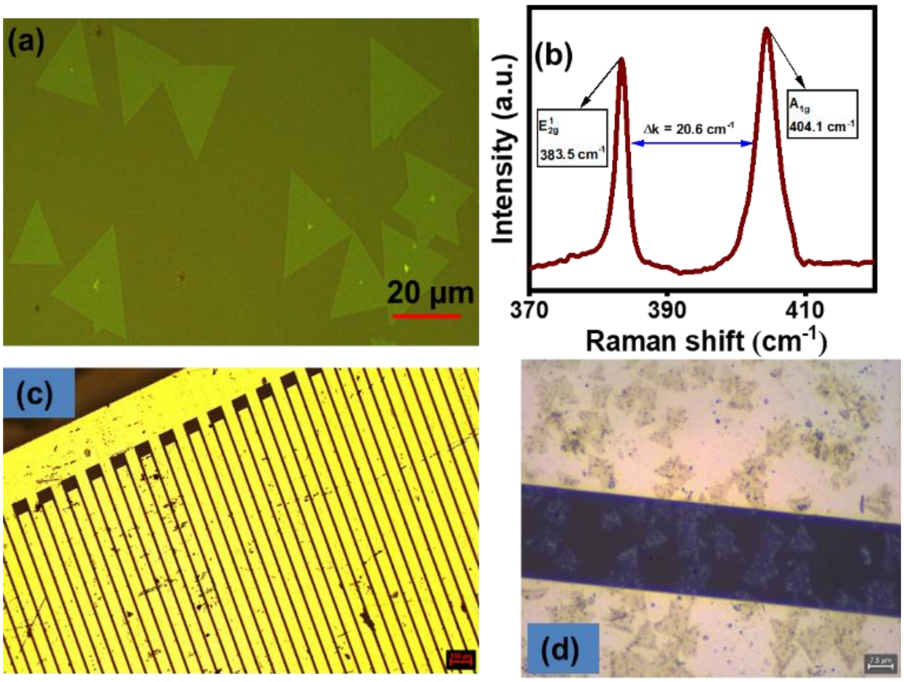

Figure 4.2: *(a) Optical microscopy Image of MoS_2, (b) Raman spectra of MoS_2, Optical microscopy image of IDE device (c) before and (d) after MoS_2 transfer.*

Following the successful fabrication of the interdigitated device and MoS_2, the energy-assisted wet transfer method is used to transfer the MoS_2 layer onto the device. The transfer procedure for the deposited MoS_2 monolayer begins by blending 10 grams of cubic polystyrene (PS) pellets in a 100 mL toluene solution. The blend undergoes ultrasonication for 30 minutes and simultaneous manual stirring with a spatula until the PS pellets are fully dissolved. Subsequently, 600 μL of the resulting solution is coated onto $MoS_2/SiO_2/Si$ for 60 s at 3000 rpm using a spin coater. The coated substrate is then heated at 80 °C in a forced air circulating oven for 40 minutes to improve adhesion between the polymer coating and the MoS_2 layer. Moreover, to enhance water diffusion between the PS–MoS_2 layer and SiO_2/Si substrate, gentle etching of the PS film occurs along the substrate edges. PDMS is placed atop the PS film for convenient handling. Repeatedly immersing the PDMS–PS–MoS_2-coated SiO_2/Si substrate in deionized water causes the PDMS–PS–MoS_2 assembly to detach from the SiO2/Si substrate. Using tweezers, the separated assembly is carefully lifted and placed onto the IDE devices. To isolate the MoS_2 on the IDEs, the PDMS film is removed by heating at 80 °C, and the PS film is removed through repeated immersion in a toluene solution. This process leaves behind a clean, crack-free monolayer of MoS_2 on the IDEs. The interdigitated device is shown in figure 4.2(c) before the MoS_2 layer is transferred and in figure 4.2(d) after the transfer.

4.3. Results and Discussion

4.3.1. AFM and Energy Dispersive X-ray (EDX) Analysis

Figure 4.3 (a) illustrates the topological features and thickness assessment of the MoS_2 monolayer on the SiO_2/Si substrate. The inset of figure 4.3 (a) presents a depth profile of the deposited MoS_2 crystal, revealing a thickness of approximately 0.7 nm, which confirms the monolayer deposition of MoS_2 [29]. Further, to confirm stoichiometric verification, X-ray photoelectron spectroscopy (XPS) analysis was conducted. The complete XPS spectrum of MoS_2 is illustrated in figure 4.3(b). The deconvoluted XPS spectra for Mo in MoS_2 reveal peaks for Mo $3d_{5/2}$ and Mo $3d_{3/2}$ at binding energies of 229.68 eV and 232.88 eV, respectively, as shown in figure 4.3(c). The high-resolution spectrum of S, presented in figure 4.3(d), exhibits deconvoluted peaks at 161.38

eV and 162.48 eV, corresponding to the S 2p3/2 and S 2p1/2 components, respectively, which align with reported binding energy values [29].

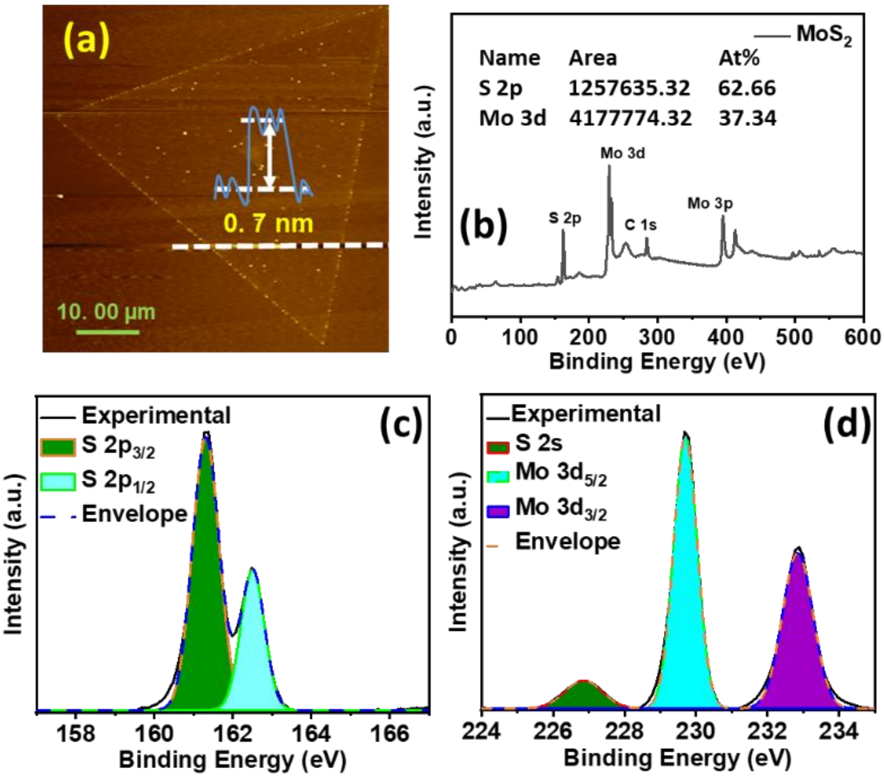

Figure 4.3: *(a) AFM, (b) XPS survey spectrum of* MoS_2 *(c) deconvoluted S 2p peaks (d) Deconvoluted Mo 3d peaks.*

4.3.1. Sensing Performance Analysis

To facilitate the Hg^{2+} ion detection across a range of concentrations, a 100 ppm standard solution of mercury ions was made by dissolving 2.56 mg of $Hg(NO_3)_2{\cdot}H_2O$ in 15 mL of PBS solution. Throughout the measurement process, the pH of ion solution was maintained at a constant level of 7. To get lower concentrations of Hg, standard solution was diluted according to the equation $M_1V_1= M_2V_2$, in this formula, M_1 represents the concentration and V_1 represents the volume of the standard solution, whereas M_2 and V_2 specify the desired concentration and volume of the diluted solution. Using this equation, solutions with various Hg^{2+} ion concentrations ranging from 1 part per trillion (ppt) to 10 ppm were prepared for sensing performance analysis.

The performance of the developed interdigitated sensor as a potential candidate for monitoring Hg^{2+} ions was evaluated by observing the response when Hg^{2+} ions and other HMIs interact with the active region of the device. The corresponding changes in the current were detected for various HMIs at 10 ppb, as well as for the PBS solution, as illustrated in figure 4.4(a). The response was assessed for 1 minute for each ion by monitoring the device's current change at a constant voltage of +4 V. The current showed minimal change for different heavy metal ions except Hg^{2+} ions. The current decreased significantly when the active region (MoS$_2$-functionalized region) is exposed to a 10 ppb Hg^{2+} ion solution, as depicted in figure 4.4(a).

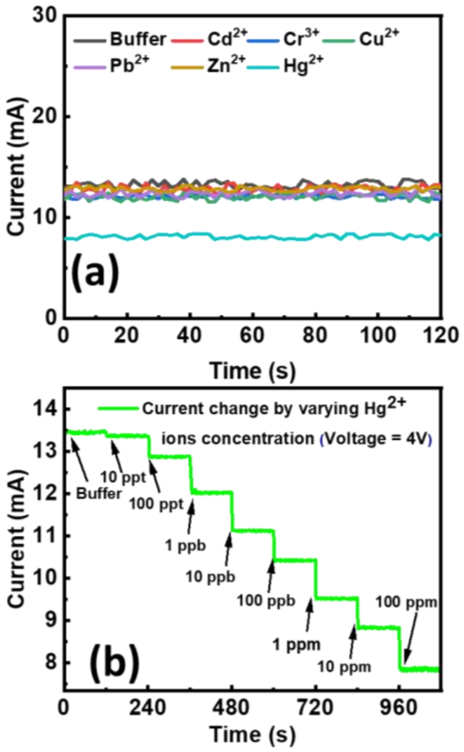

Figure 4.4: *(a) Sensor response to various heavy metal ions (b) Real-time detection Hg^{2+} ions.*

Figure 4.4(b) illustrates the response of MoS$_2$-functionalized IDEs when exposed to Hg^{2+} ions. During the sensing process, Hg^{2+} ion solutions with concentrations ranging from 1 ppt to 100 ppm are introduced to the MoS$_2$-functionalized surface. The response is monitored for 1 minute at each Hg^{2+} ion concentration, revealing a visible change in current, indicative of successful Hg^{2+} ion detection.

The sensing mechanism of the MoS_2-based Hg^{2+} sensor is shown in Fig. 5, illustrating interactions before and after exposure to Hg^{2+} ions. Upon exposure to an Hg^{2+} ion solution, S^{2-} present in the MoS_2 layer reduces Hg^{2+} to Hg^0 on its surface. This phenomenon is intriguing and is believed to occur because of the strong oxidizing and electrophilic properties of Hg^{2+} ions at room temperature (RT), combined with the natural reducing properties of S^{2-} present in MoS_2. Consequently, the S^{2-} group present in MoS_2 transfers electrons to the adsorbed Hg^{2+} ions, forming Hg-S complexes, as depicted in Fig. 5.

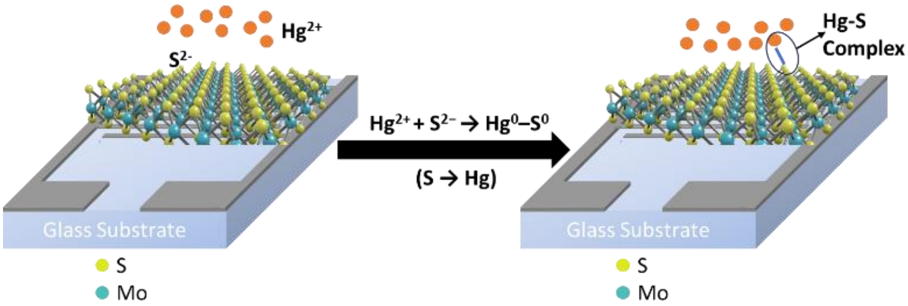

Figure 4.5: *Mechanism of Hg^{2+} ion detection on the MoS_2 functionalized surface.*

As defined above, the sensing mechanism for Hg^{2+} involves its spontaneous reduction over MoS_2 because Hg^{2+} ions have a greater reduction potential than S^{2-} ions, which function as a natural reducing agent. This mechanism explains why the sensor is more sensitive to Hg^{2+} than to other ions like Pb^{2+} and Cu^{2+}. When two heavy metal ions, such as Hg^{2+} and Pb^{2+}, which exhibit an affinity for S^{2-} ions, are present, Hg^{2+} is preferred for reduction by MoS_2 due to the standard reduction potential of Hg^{2+} ions are higher (0.85 V) compared to Pb^{2+} (-0.13 V) [30]. Hence, the MoS_2 shows higher selectivity towards Hg^{2+} because its reduction potential is greater in comparison to Pb^{2+}. Therefore, thermodynamically, when Hg^{2+}, Cu^{2+}, and Pb^{2+} (and other HMIs with less reduction potential) are present, Hg^{2+} is favoured for reduction.

Separate solution method has been employed to evaluate the selectivity of MoS_2 based IDE for Hg^{2+} ions and other HMIs. In this approach, the selectivity coefficient (response ratio) $R_{Hg^{2+}, j}$ is determined by equation (1) [31].

$$R_{Hg^{2+},j} = \frac{(|I_b - I_j|)C_{Hg^{2+}}}{(|I_b - I_{Hg^{2+}}|)C_j} \ldots\ldots\ldots\ldots\ldots \text{(1)}$$

Here, I_b represents the response current when the MoS_2 functionalized IDE device is immersed in a PBS solution, I_j represents the current corresponding to meddling ions at a concentration of C_j, and $I_{Hg^{2+}}$ denotes the current at a concentration of $C_{Hg^{2+}}$.

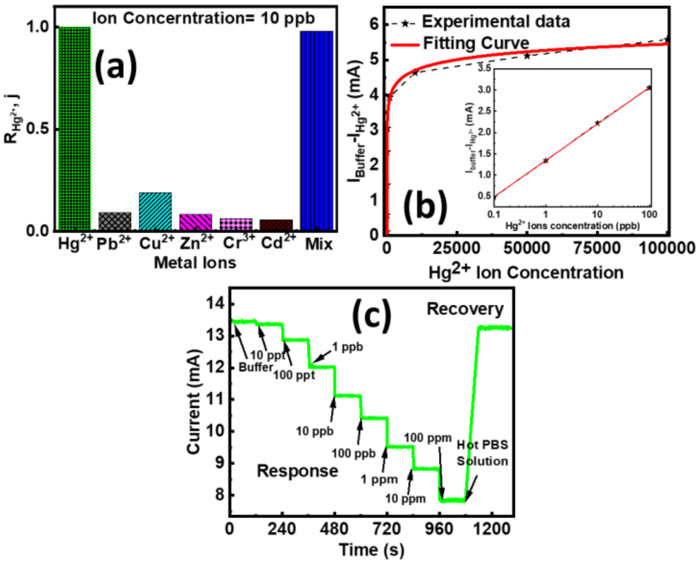

Figure 4.6: *(a) Response ratio for* Hg^{2+} *ions and other interfering HMIs for selectivity analysis, (b) calibration curve to calculate limit of detection and for* Hg^{2+} *ions and, (c) response-recovery characteristics.*

The sensing responses to Hg^{2+} ions and interfering HMIs are assessed at an equivalent concentration of 10 ppb. The response ratio at a concentration of 10 ppb is depicted in figure 4.6(a) based on equation (1). A lower $R_{Hg^{2+}, j}$ value signifies greater selectivity and reduced interference from other HMIs. Figure 4.6(a) shows that the sensor is highly selective for Hg^{2+} ions, mainly due to strong interactions between sulfur ions and Hg^{2+}. There is little interference detected from Pb^{2+} ions and Cu^{2+} ions.

The sensitivity and detection limit (LoD), are determined by analyzing the relationship between current (I) and Hg^{2+} ion concentration, as shown in figure 4.6(b). Equation (2) is employed for the standard 3-sigma method, which is used to calculate the LoD. (2) [32]:

$$LoD = \frac{3\sigma}{m} \ldots\ldots\ldots\ldots\ldots\ldots \ (2)$$

The sensitivity (m) of the proposed sensor is computed as the slope of the calibration curve, which is determined to be 957 μA/ppb.

The σ (standard deviation) and the linear regression coefficient, are extracted from figure 4.6(b) as 0.00894 and 0.9998, respectively. Consequently, the limit of detection is calculated as 27.96 ppt by using equation 2. The LoD of the sensor is lower than the WHO standard limit for Hg^{2+} ions in drinking water.

Figure 4.6(c) displays the recovery and response of sensor. When the sensor is exposed to mercury ions, these ions bond strongly with the surface of the MoS_2. This makes it difficult to remove the mercury ions from the surface, which requires a higher activation energy to detach mercury ions from the sensor surface [32, 19]. To achieve this, the sensor is dipped in heated PBS at 150 °C for 90 s to facilitate recovery from the bound Hg^{2+} ions. Remarkably, the recovery rate reaches as high as 99.25% during this process.

The repeatability of the sensor is demonstrated in figure 4.7(a), where the sensor consistently produced the same response under identical conditions. Furthermore, the reproducibility of the sensor was verified by fabricating five devices and conducting sensing tests under the same conditions, as shown in figure 4.7(b). The slight difference in response between the two devices may be attributed to variations in their internal resistance [33]. These results confirm that the sensor is highly reproducible. Additionally, the sensor's response was monitored over 60 days, with a response variation of less than 3%, as shown in figure 4.7(c), indicating its suitability for long-term applications.

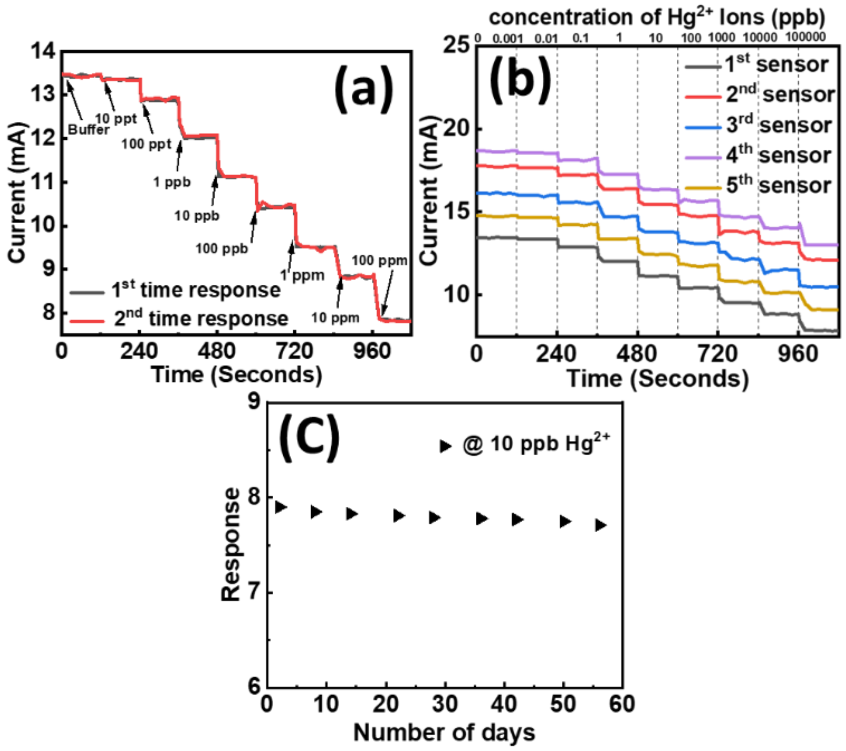

Figure 4.7: *(a) Repeatability of the sensor, (b) sensor reproducibility, and (c) the* Hg^{2+} *sensor stability over time.*

The proposed MoS_2-based sensor was compared with the existing Hg^{2+} ion sensors. The results of this comparison are presented in Table 4.1. The comparison focuses on metrics such as sensitivity, limit of detection (LoD), and response time for Hg^{2+} ion detection. It was found that the MoS_2-functionalized IDE sensor exhibited superior LoD, higher sensitivity, and faster response times compared to previously reported Hg^{2+} ion sensors.

Table 4.1: *Performance comparison of* Hg^{2+} *ion sensors.*

S. No.	Functionalized Material	Process	Sensitivity (μA/ppb)	LoD (ppb)	Response time	Ref.
1.	rGO/TGA-AuNP	ISFET	0.3	5	< 10 s	[34]

2.	Glucose-AgNP	LSPR on Fibre	…..	2	……	[35]
3.	Au-nanoparticles	Colorimetry	…..	3.4	……	[36]
4.	L-cysteine	Electrochemical	0.2031	0.995	---	[37]
5.	TGA/Au	AlGaN/GaN HEMT	-----	27; 3	5 s; 15-20 s	[38, 39]
6.	AgNW/MoS_2 nanocomposite	AlGaN/GaN HEMT	1640	0.058	-----	[49]
7.	MoS_2 nanosheets	Colorimetry	-----	100.25	-----	[41]
8.	MoS_2-Au	Colorimetry	-----	1.005	-----	[42]
9.	**MoS_2**	**Electrochemical**	**957**	**0.0279**	**< 4 s**	**Our work**

Glossary: LSPR- localized surface plasmon resonance, TGA-Thioglycolic acid

4.4. Conclusion

In this chapter, we successfully synthesized a monolayer of MoS_2 using a CVD system. The MoS_2 layer was then transferred to IDEs via a surface energy-assisted wet transfer method. The electrical response of the proposed sensor shows high selectivity toward Hg^{2+} ions across the entire test range. The device demonstrated remarkable performance, with a rapid response time of less than four seconds and an exceptional detection limit of 27.9 ppt for Hg^{2+} ions, exhibiting high selectivity. The exceptional sensing capabilities of the MoS_2 sensor are attributed to the formation of multiple binding sites where Hg^{2+} ions form strong complexes with the sulfur atoms in MoS_2. Moreover, the device demonstrated a high recovery rate of 99.25%, making it a highly reusable and robust solution for detecting Hg^{2+} ions in water. Given its outstanding performance, the sensor holds great promise for real-world applications in detecting toxic metals in water.

4.5. References

[1] Y. Chen, L. Wu, Y. Chen, N. Bi, X. Zheng, H. Qi, et al., “Determination of mercury(II) by surface-enhanced Raman scattering spectroscopy based on thiol-functionalized silver nanoparticles”, Microchimica Acta, Vol.177, pp. 341-348, 2012.

[2] S.M. Sayyah, M. Shaban, M. Rabia, “A high-sensitivity potentiometric mercuric ion sensor based on m-Toluidine films”, IEEE Sens. J., Vol. 16 , pp. 1541-1548, 2016

[3] Y. Cho, S.S. Lee, J.H. Jung, “Recyclable fluorimetric and colorimetric mercury-specific sensor using porphyrin-functionalized Au@SiO2 core/shell nanoparticles” Analyst, Vol. 135, pp. 1551-1555, 2010.

[4] M.B. Gumpu, S. Sethuraman, U.M. Krishnan, J.B.B. Rayappan, “A review on detection of heavy metal ions in water – an electrochemical approach”, Sens. Actuators B Chem., Vol. 213, pp. 515-533, 2015.

[5] S. Bettini, R. Pagano, L. Valli, G. Giancane, “Spectroscopic investigation of the selective interaction of mercuric and cupric ions with a porphyrin active layer”, J. Phys. Chem. C, Vol. 118, pp. 12384-12390, 2014.

[6] F. Arduini, C. Majorani, A. Amine, D. Moscone, G. Palleschi, “Hg2+ detection by measuring thiol groups with a highly sensitive screen-printed electrode modified with a nanostructured carbon black film”, Electrochim. Acta, Vol. 56, pp. 4209-4215, 2011.

[7] J. Gong, T. Zhou, D. Song, L. Zhang, X. Hu, “Stripping voltammetric detection of mercury(II) based on a bimetallic Au−Pt inorganic−Organic hybrid nanocomposite modified glassy carbon electrode”, Anal. Chem., Vol. 82, pp. 567-573, 2010.

[8] X. Jia, D. Chen, L. Bin, H. Lu, R. Zhang, Y. Zheng, "Highly selective and sensitive phosphate anion sensors based on AlGaN/GaN high electron mobility transistors functionalized by ion imprinted polymer", Sci. Rep., Vol. 6, pp. 1-7, 2016.

[9] S. Li, Z. Xu, X. Cheng, Q. Zhang, "Dissolved trace elements and heavy metals in the Danjiangkou Reservoir", China. Environ. Geol. Vol. 55, PP. 977–983, 2016.

[10] L. Kong, , L. Yan, Z. Qu, N. Yan, L. Li, "β-Cyclodextrin stabilized magnetic Fe3S4 nanoparticles for efficient removal of Pb(ii)", J. Mater. Chem. A, Vol.3, no. 30, pp. 15755-15763, 2015.

[11] S. Bian, C. Shen,H. Hua, L. Zhou, H. Zhu, F. Xi, J. Liu, X. Dong, "One-pot synthesis of sulfur-doped graphene quantum dots as a novel fluorescent probe for highly selective and sensitive detection of lead(ii)", RSC Adv. Vol. 6, pp. 69977−69983, 2016.

[12] B. Zhang, J. Chen, H. Zhu, T. Yang, T. Zou, M. Zhang, M. Du,"Facile and green fabrication of size-controlled AuNPs/CNFs hybrids for the highly sensitive simultaneous detection of heavy metal ions", Electrochim. Acta, Vol. 196, pp. 422−430, 2016.

[13] X. Ma, S.M. Armas, M. Soliman, D.A. Lytle, K. Chumbimuni-Torres, L. Tetard, W.H. Lee, "In situ monitoring of Pb2+ leaching from the galvanic joint surface in a prepared chlorinated drinking water", Environ. Sci. Technol., Vol. 52, pp. 2126–2133, 2018.

[14] V.K. Gupta, Imran Ali, Tawfik A. Saleh, Arunima Nayak, and Shilpi Agarwal, "Chemical treatment technologies for waste-water recycling—an overview", RSC Adv., Vol.2, No.16, pp. 6380-3688, 2012.

[15] D. Akinwande, C. Huyghebaert, C.H. Wang, M. I. Serna, S. Goossens, L. J. Li, H. S. P. Wong, F. H. L. Koppens, "Graphene and Two-Dimensional Materials for Silicon Technology", Nature Vol. 573, pp. 507– 518, 2019.

[16] D. S. Rana , R. Sharma, S. Kumar, N. Gupta, S. Thakur, K. K. Thakur, D. Singh, "Molybdenum disulfide (MoS_2) and reduced

graphene oxide (rGO) nanocomposite based electrochemical sensor for detecting mercury(II) ions", Nano-Structures & Nano-Objects, vol. 36, 101041, 2023.

[17] J. Mishra, N. Sharma, S. Kumar, C. Das, A. Kumar, M. Kwoka, S. Sahu, and M. Kumar, "MoS_2@MWCNT modified glassy carbon electrode for electrochemical mercury(II) ion sensors" , J. Mater. Chem. C, 2024.

[18] P. Maiti, S. Das, J. Panda, D. Karmakar, A. Pal, S. Guha, A. Sengupta, S. Paul, P. K. Paul, "Spectrofluorometric detection of mercury ions in aqueous medium and cellular milieu using MoS_2 nanoflakes", Journal of Physics and Chemistry of Solids, vol. 184, 111680, 2024.

[19] A. Nigam et al., " Real time detection of Hg^{2+} ions using MoS 2 functionalized AlGaN/GaN high electron mobility transistor for water quality monitoring ", Sens. Actuators B Chem., vol. 309, Apr. 2020.

[20] Jun Jiang Luo, Ling Yun Qin, Xiao Juan Du, Hong Qun Luo, Nian Bing Li, and Bang Lin Li, "Mercury ion-engineering Au plasmonics on MoS2 layers for absorption-shifted optical sensors", Anal. Methods, vol. 13, pp. 5436-5440, 2021.

[21] P. Li, D. Zhang, Z. Wu, "Flexible MoS2 sensor arrays for high performance label-free ion sensing", Sensors and Actuators A: Physical, vol. 286, pp. 51-58, 2019.

[22] M. O'Brien, N. McEvoy, D. Hanlon, et al., "Mapping of Low-Frequency Raman Modes in CVD-Grown Transition Metal Dichalcogenides: Layer Number, Stacking Orientation and Resonant Effects", Sci Rep, vol. 6, 19476, 2016.

[23] A. Singh, M. Moun, R. Singh, "Effect of different precursors on CVD growth of molybdenum disulfide", Journal of Alloys and Compounds, vol. 782, pp. 772-779, 2019.

[24] W. Zhang, P. Zhang, Z. Su, and G. Wei, “Synthesis and sensor applications of MoS2-based nanocomposites”, Nanoscale, vol. 7, pp. 18364-18378, 2015.

[25] E. Vinoth, N. Gopalakrishnan, “Fabrication of interdigitated electrode (IDE) based ZnO sensors for room temperature ammonia detection”, Journal of Alloys and Compounds, vol. 824, 153900, 2020.

[26] Chang Liu, Shilin Zeng, Bingqiao Yang, Feifei Jia, Shaoxian Song, “Simultaneous removal of Hg^{2+}, Pb^{2+} and Cd^{2+} from aqueous solutions on multifunctional MoS_2”, Journal of Molecular Liquids, vol. 296, 111987, 2019.

[27] R. Aswathia, K. Y. Sandhya, “Ultrasensitive and selective electrochemical sensing of Hg(ii) ions in normal and sea water using solvent exfoliated MoS_2: affinity matters”, J. Mater. Chem. A, vol. 6, pp. 14602-14613, 2018.

[28] C. Lee, H. Yan, L. E. Brus, T. F. Heinz, J. Hone, S. Ryu, “Anomalous Lattice Vibrations of Single- and Few-Layer MoS2”, ACS Nano, Vol. 4, pp. 2695– 2700, 2010.

[29] C. Patel et al., " Large and uniform single crystals of MoS_2 monolayers for ppb-level NO_2 sensing ", ACS Appl. Nano Mater., vol. 5, no. 7, pp. 9415-9426, Jun. 2022.

[30] S.-Y Cho, S. J. Kim, Y. Lee, J.-S Kim, W.-B Jung, H.-W. Yoo, J. Kim, H.-T. Jung, “Highly Enhanced Gas Adsorption Properties in Vertically Aligned MoS2 Layers”, ACS Nano, Vol. 9, pp. 9314– 9321, 2015.

[31] A. Nigam, N. Sharma, D. Lobanov, A. Novikov and M. Kumar, "Ultrasensitive Detection of Mercury Ions Under UV Illumination of MoS2 Functionalized AlGaN/GaN Transistor," in IEEE Transactions on Electron Devices, vol. 67, no. 12, pp. 5693-5700, 2020.

[32] S. Chaudhary et al., "Ag-Loaded WS_2-Based Pb^{2+} Ion Detection in Water," in IEEE Sensors Journal, vol. 24, no. 3, pp. 2421-2428, 2024.

[33] A. Nigam, T. N. Bhat, V. S. Bhati, S. B. Dolmanan, S. Tripathy and M. Kumar, "MPA-GSH functionalized AlGaN/GaN high-electron mobility transistor-based sensor for cadmium ion detection", IEEE Sensors J., vol. 19, no. 8, pp. 2863-2870, Apr. 2019.

[34] K. Chen, et al., “Hg(II) Ion Detection Using Thermally Reduced Graphene Oxide Decorated with Functionalized Gold Nanoparticles”Anal. Chem. Vol. 84, No. 9, pp. 4057–4062, 2012.

[35] G. M. Shukla, et al., “Optimization of Plasmonic U-Shaped Optical Fiber Sensor for Mercury Ions Detection Using Glucose Capped Silver Nanoparticles”, IEEE Sensors Journal, vol. 19, no. 9, pp. 3224-3231, 2019.

[36] N. Sidana, et al., “A Simple and Highly Selective Colorimetric Sensing of Hg2+ Ions Based on Anti-Aggregation of Gold Nanoparticles”, IEEE Sensors Journal, vol. 22, no. 23, pp. 22549-22556, 2022.

[37] S. Muralikrishna, et. al., “In situ reduction and functionalization of graphene oxide with l-cysteine for simultaneous electrochemical determination of cadmium(II), lead(II), copper(II), and mercury(II) ions, Anal. Methods 6 (2014) 8698–8705.

[38] K.H. Chen, et al., “Low Hg (II) ion concentration electrical detection with AlGaN/GaN high electron mobility transistors”, Sens. Actuators B Chem. 134 (2008) 386–389.

[39] H.-T. Wang, et al., “Fast electrical detection of Hg(II) ions with AlGaN⁄GaN high electron mobility transistors”, Appl. Phys. Lett. 91 (2007) 042114.

[40] N. Sharma, A. Nigam, D. Lobanov, A. Gupta, A. Novikov and M. Kumar, "Mercury (II) Ion Detection Using AgNWs-MoS$_2$ Nanocomposite on GaN HEMT for IoT-Enabled Smart Water Quality Analysis," in IEEE Internet of Things Journal, vol. 9, no. 16, pp. 14317-14324, 15 Aug.15, 2022.

[41] Y. Lu, et al., “Spectrophotometric determination of mercury(II) ions based on their stimulation effect on the peroxidase-like activity of

molybdenum disulfide nanosheets", Microchim. Acta, vol. 183, pp. 2481-2489, 2016.

[42] Chunmeng Ma, et al., "Colorimetric determination of Hg^{2+} in environmental water based on the Hg^{2+} stimulated peroxidase mimetic activity of MoS_2-Au composites", Journal of Colloid and Interface Science, vol. 537, pp. 554-561, 2019.

Chapter 5

Ultrasensitive Detection of Hg^{2+} Ions with CVD Grown MoS_2-Functionalized MgZnO/CdZnO HEMT

5.1. Introduction

Heavy metals naturally occur in the crust of Earth and pose a risk to human health due to their tendency to accumulate in our bodies. Among various heavy metal ions (HMIs), the mercury (II) (Hg^{2+}) ion is of particular interest from an environmental perspective. Its noxiousness has been acknowledged as a persistent environmental issue [1-3]. Mercury enters the in water and soil through various sources, including fossil fuel combustion, volcanic emissions, mining, and solid waste burning. Worldwide, there is growing concern about impact of mercury on human health and wildlife ecology. Certain bacteria transform inorganic Hg^{2+} ions into organic compounds that are neurotoxic, which subsequently accumulate in animals, plants, and enter in the food chain, impacting the whole ecosystem [4-6].

Even trace amount of mercury ions accumulating in human body might result in hazardous conditions. Exposure of excessive mercury leads to severe chronic health conditions, including neurodegenerative diseases, cancer, nephrotic syndrome, pulmonary edema, and respiratory failure [7]. Despite these risks, mercury continues to be widely used in domestic commercial and applications. The WHO (World Health Organization) and the EPA (Environmental Protection Agency) set acceptable limits of 1 part per billion (ppb) and 2 ppb, respectively, for mercury ions in drinking water [3, 8]. Therefore, in order to address the health dangers, it is imperative that we identify these ions using a highly selective and sensitive technique. Various methods have been explored for detecting Hg^{2+} ions, including electrochemical techniques, optical analysis, Fluorometry, inductively coupled plasma-atomic emission spectrometry (ICP-AES), and atomic absorption spectroscopy (AAS), [9-15]. Although these detecting approaches exhibit good sensitivity, their limitations include expensive laboratory setups, extended response times, and the need for well-trained manpower for the sophisticated instruments' operation [16]. Ion-sensitive field-effect transistors based on silicon are commonly used for ion detection nevertheless, their viability for on-site HMI detection is limited by their dependency on reference electrodes and instability in harsh environmental conditions.

The high-electron-mobility transistors (HEMTs) offer an appealing solution for detecting mercury (Hg^{2+}) ions. To achieve high sensitivity and quick response times, these transistors have a high electron sheet carrier concentration channel, electrical and chemical stability in an ionic medium, and surface charges [16, 17]. The existing AlGaN/GaN HEMT-based biosensors suffer from gate-induced leakage current [18, 19]. This leakage can lead to inaccuracies in the output device parameters, making it difficult to reliably predict the sensitivity. Therefore, suppressing this leakage is essential. Recent research has focused on ZnO-based nano electronic devices, with their favourable material features like bulk growth capability, higher energy bandgap, lower lattice mismatch, higher saturation velocity, and greater sensitivity. ZnO-based heterostructure exhibits strong piezoelectric and spontaneous polarization, which induces the two-dimensional electron gas (2DEG) at the heterointerface [20]. Devices with 2DEG channel is highly sensitive because the channel is near to the surface, so due to absorption of analytes the stress directly effects the conduction of current in the channel. which enhances their overall sensitivity.

The sensing material effect the efficiency to detect the targeted analyte and the performance of electrochemical sensor. Numerous nanomaterials, like carbon-based materials (such as graphene oxides), MXenes, BODIPY, and layered double hydroxides have been explored for HMIs detection due to their exclusive properties [21-24]. Nevertheless, these materials face several drawbacks, such as lower stability, fewer adsorption sites, poor dispersibility, limited biocompatibility, reduced surface area, lower chemical reactivity, small particle size, and substandard durability [21, 22]. Consequently, there is a pressing need for an effective electrochemical sensing device that can detect Hg^{2+} ions with excellent sensitivity.

Recently, there has been a significant increase in the study of atomically thin two-dimensional transition metal dichalcogenides (2D-TMDs) because of their intriguing electrical and optical characteristics, which make them promising contenders for several applications including sensors [25], optoelectronics, spintronics, and valleytronics [26]. Among the various options, molybdenum disulfide (MoS_2) poses semiconductor characteristics with a tuneable band gap, making it the highlight of the existing TMDs. The bandgap depends on the thickness of the MoS_2 with monolayer having a direct bandgap of 1.2 eV to a multilayer (bulk) having an indirect bandgap of 1.8 eV [27, 28]. The 2D MoS_2 has distinct advantage over its bulk equivalents owing to the large binding energy excitons and the absence of lattice inversion symmetry [29].

This chapter discusses MgZnO/CdZnO (MCO) HEMT simulation using Silvaco-TCAD and its validation against established literature. An oxide-based high electron mobility transistor sensor is fabricated using optical lithography and a dual ion beam sputtering (DIBS) system, designed to detect trace amount of Hg^{2+} ions in water. MoS_2, synthesized via chemical vapor deposition, was transferred to the MCO HEMT gate using an energy-assisted wet transfer method, functionalizing the gate region specifically for Hg^{2+} ion detection.

5.2. Simulation of Oxide HEMT

Before fabricating MgZnO/CdZnO HEMT, the HEMT structure is simulated using Silvaco-TCAD. The ATLAS two-dimensional drift-diffusion simulator [30] is used to model the device response. As shown in figure 5.1(a), the MZO HEMT structure consists of a 50 nm HfO_2 dielectric layer at the gate terminal, 2 nm MgZnO barrier layer, 10 nm ZnO channel layer, 200 nm MgZnO buffer layer, and a 15 nm thick ZnO nucleation layer on the substrate. The 1 µm gate length (L_g), 50 µm channel width (W_g), 1 µm source-to-gate length (L_{sg}) and 1 µm gate-to-drain length (L_{gd}) have been used for the simulation. In the MZO-based HEMT, a 1 nm thin layer of MgO, as in figure 5.1(b), is sandwiched between MgZnO and ZnO layer, and as shown in figure 5.1(c), the ZnO layer is replaced by CdZnO layer to simulate the MgZnO/CdZnO (MCO) HEMT to study the confinement of 2DEG, which plays an important role in the sensing application. The material parameters used in the simulation are shown in Table 5.1. The parameters for $Mg_xZn_{1-x}O$ and $Cd_xZn_{1-x}O$ are obtained from linear combinations of the parameters for ZnO, MgO and CdO [31].

Table 5.1: *Parameters of MgZnO and CdZnO calculated from mole fraction (x) at room temperature*

Parameters	Description	$Mg_xZn_{1-x}O$	$Cd_yZn_{1-y}O$	References
C_{13}	Elastic stiffness constant (GPa)	$84 + 4x$	$105.1 + 44.1y$	[32], [33]
C_{33}	Elastic stiffness constant (GPa)	$176 - 9x + 55x^2$	$210.9 - 105.9y$	[32], [33]
E_{31}	Piezoelectric constant (C/m^2)	$-0.55 - 0.23x$	$-0.62 + 0.14y$	[32], [33]
E_{33}	Piezoelectric constant (C/m^2)	$1.24 - 1.1x$	$0.96 + 0.71y$	[32], [33]

a	Lattice constant (nm)	$0.3246 + 0.0016x + 0.0109x^2$	$0.3246 + 0.428y$	[33]
P_{SP}	Spontaneous polarization (C/m^2)	$-0.057 - 0.066x$	$-0.15y$	[33]

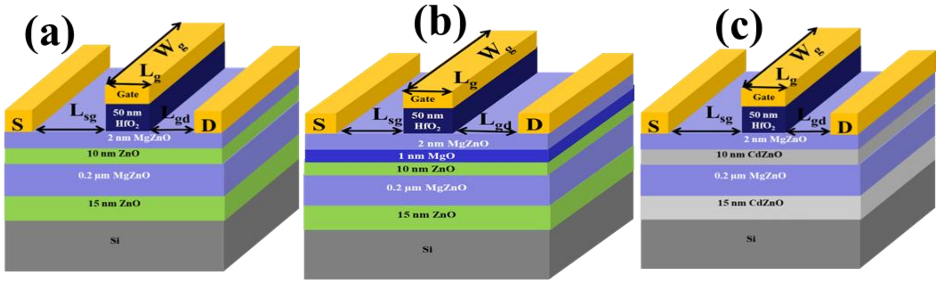

Figure 5.1: *Schematic of (a) MZO HEMT, (b)MZO HEMT with MgO layer, (c) MCO HEMT.*

The simulated transfer characteristics are in good agreement with the experimental results reported for MZO HEMT [34] as shown in figure 5.2(a, b). Once, the appropriate model is determined, the simulations for the MZO HEMT with MgO spacer layer and MCO HEMT are carried out. The threshold voltage (V_{th}) for the MZO HEMT with MgO spacer layer is -2 V and -3.7 V for MCO HEMT, as shown in figure 5.2(d, e). For MZO HEMT, the value of V_{th} is -1.7 V. The shift of V_{th} with the insertion of MgO interfacial layer and in MCO HEMT is due to the increase in the electron density of the channel induced by the enhanced polarization charge [35]. A maximum drain current ($I_{\mathrm{ds,max}}$) of 190 mA/mm, 284 mA/mm and a maximum transconductance ($g_{\mathrm{m,max}}$) of 91 mS/mm and 103 mS/mm is observed for MZO HEMT with MgO spacer layer and MCO HEMT, respectively, which are higher as compared to those for the conventional MZO HEMT ($I_{\mathrm{ds,max}}$ = 162 mA/mm, $g_{\mathrm{m,max}}$ = 73 mS/mm).

Figure 5.2(c, d) shows the simulated output DC characteristics which are in good agreement with the experimentally reported results for MZO HEMT [36]. For the conventional MZO HEMT structure, and MZO HEMT with MgO layer the saturation drain current (I_{DS}) is 181 mA/mm and 182 mA/mm at V_{GS} = 1 V and V_{DS} = 5 V. While the MCO HEMT structure, the saturation drain current increases to I_{DS} = 281 mA/mm at V_{GS} = 1 V and V_{DS} = 5 V. This is due to the increment in the channel's electron density induced by the enhanced polarization charge. The 2DEG density of MCO HEMT is high as compared to GaN HEMT but it has lower current density than GaN HEMT because of less mobility of MCO HEMT compared to GaN HEMT.

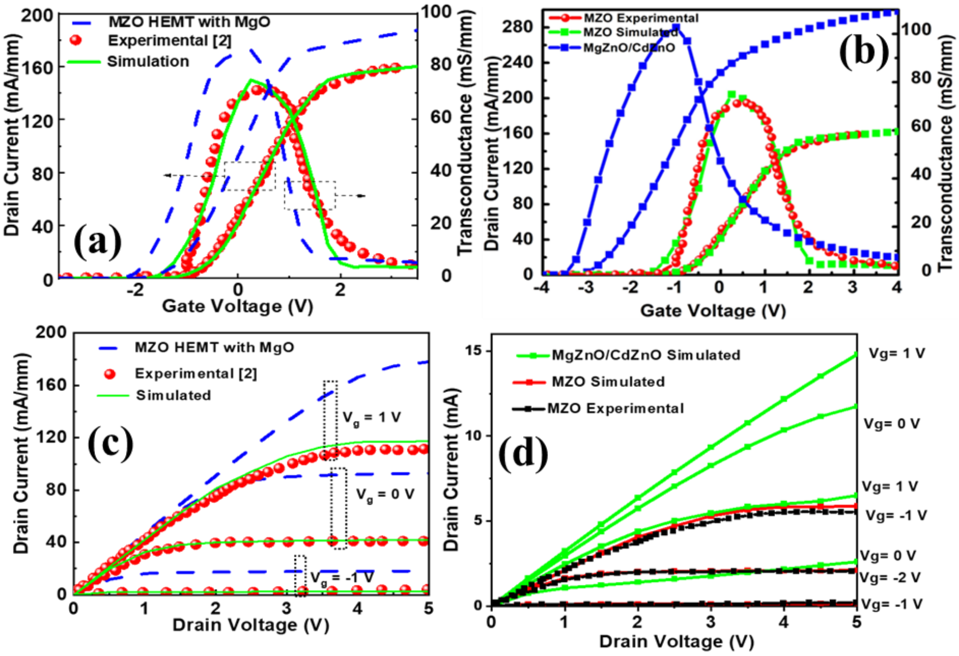

Figure 5.2: *Transfer characteristics and transconductance of (a) MZO HEMT and MZO HEMT with MgO layer (b) MZO HEMT and MCO HEMT at* V_{DS} *= 4 V, Transfer characteristics of (c) MZO HEMT and MZO HEMT with MgO layer (d) MZO HEMT and MCO HEMT.*

The high performance of MCO HEMT seems to be attributed to their high 2DEG density and mobility. The room-temperature 2DEG electron density of MCO HEMT is 9.2×10^{13} cm^{-2} whereas that for the conventional MZO HEMT is 2.5×10^{13} cm^{-2} and for MZO HEMT with MgO layer is 7.2×10^{13} cm^{-2}. The maximum transconductance is the ratio of the current change at the output port (I_{DS}) to the voltage change at the input port (V_{gs}) and for the MCO HEMT the drain current is increase significantly which results in improved transconductance. From above results, it can be concluded that the MCO HEMT has better performance.

5.3. MgZnO/CdZnO HEMT based Hg^{2+} Ion Detection

5.3.1. Materials

The chemicals used in this work are obtained from Alfa Aesar, ensuring a 99.999% purity level, and are employed without alteration. In this work, the materials utilized include molybdenum trioxide (MoO_3), ammonium hydroxide (NH_4OH, 25% solution), and NaCl for the synthesis of MoS_2. Disodium hydrogen phosphate (Na_2HPO_4) and sodium dihydrogen phosphate (NaH_2PO_4) are used to make the phosphate buffer solution (PBS). Further, chemicals like $Hg(NO_3)_2.H_2O$, $Cr(NO_3)_3.9H_2O$, $CuSO_4$, $Cd(NO_3)_2.4H_2O$, $Zn(NO_3)_2.6H_2O$, and $Pb(NO_3)_2$, $AgNO_3$, $Fe(NO_3)_3.(H_2O)_9$, $Sn(NO_3)_2$ were utilized to prepare ionic solutions containing the corresponding metal ions for sensing analysis.

5.3.2. MgZnO/CdZnO HEMT Fabriaction

The heterostructure consists of a 30 nm $Mg_{0.05}Zn_{0.95}O$ barrier layer on top of a 400 nm $Cd_{0.15}Zn_{0.85}O$ buffer layer, which is placed over a 200 nm Y_2O_3 spacer layer. These layers are deposited onto a silicon substrate utilizing the DIBS system, as shown in figure 5.3(a). Before depositing the heterostructure, the Si substrate undergoes a cleaning process as described in our earlier in chapter 2. Following the cleaning procedure of the Si substrate, the spacer layer of Y_2O_3 is deposited in pure Ar environment and a temperature of 100 °C. Subsequently, the MCO heterostructure is grown on top of Y_2O_3 using the DIBS system. This deposition carried out at an $Ar:O_2$ ratio of 2:3, a beam voltage (800 V), ion beam power (44 W), temperature (300 °C), and a working pressure (2.43×10^{-4} mbar). After the growth of the MCO heterostructure, the surface morphological analysis has been conducted with atomic force microscopy (AFM). AFM image of the MCO heterostructure, measuring 5 µm x 5 µm, is displayed in figure 5.3(b). The surface levels are clearly observable regarding the surface morphology. For the sample, the root mean square roughness values are 0.70 nm. This indicates the quality growth of MCO heterostructure over the silicon substrate.

The drain, source contacts of the MCO HEMT were fabricated using a metal stack comprising Al (150 nm), Cr (30 nm), and Au (200 nm), deposited via a thermal evaporation technique. This stack of metals was patterned using MJB4 mask aligner photolithography to define the drain and source mask of ~1.4 microns S1813 photoresist Following etching, rapid thermal annealing was performed at 850°C for 50 s under a constant nitrogen (N_2) flow to delineate the source and drain metal connections.

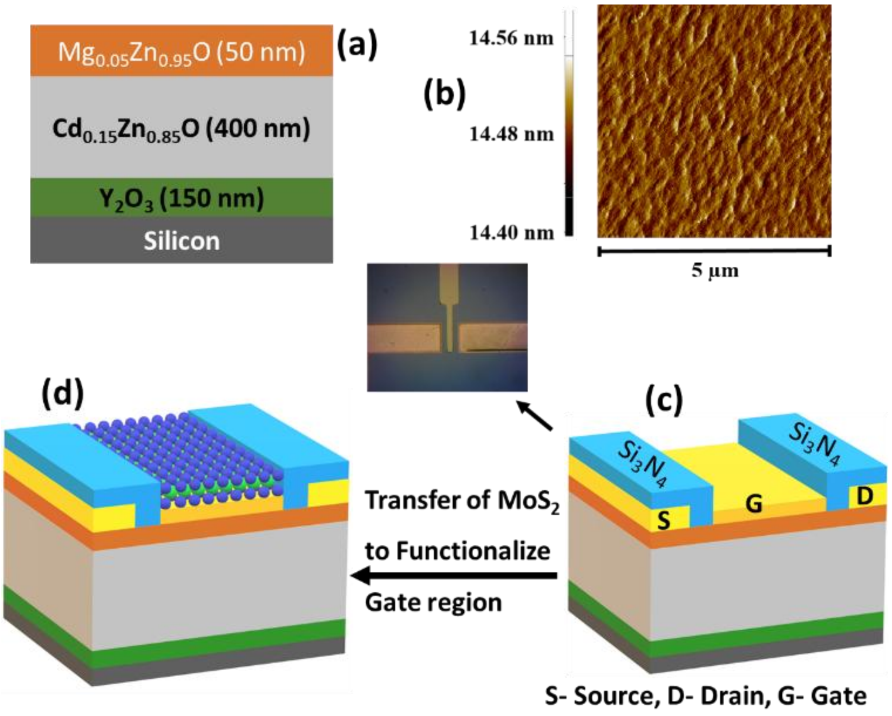

Figure. 5.3: *Details of the of MoS_2 functionalized MCO HEMT. (a) Diagram illustrating the sputtering deposition of MCO heterostructure on a silicon wafer. (b) AFM image of MCO heterostructure on silicon wafer. (c) Schematic representation of the constructed MCO HEMT (inset: optical microscopic picture of the completed device). (d) Schematic representation of the MoS_2 functionalized MCO HEMT sensor following the transfer of MoS_2.*

The separation between these contacts is 100 µm. A 250 nm Si_3N_4 layer was formed using sputtering to passivate the source and drain contacts, and subsequently patterned through lithography to expose the contact pads and gate area. A Ni (10 nm) and Au (50 nm) layer was deposited for gate contact fabrication using thermal evaporation and subsequently patterned using standard photolithography, yielding a 50 µm long gate. Figure 5.3 (c) presents a schematic depiction of the MCO HEMT layered structure.

5.3.3. MoS_2 Functionalization of Gate Region

The MoS_2 layer of uniform and substantial size is synthesized onto SiO_2/Si substrates is synthesized using an atmospheric pressure chemical vapor deposition (CVD) system (Quazar Technologies Pvt. Ltd.). Following the successful synthesis of the MoS_2, the layer is transferred on the gate region of MCO HEMT using the energy-assisted wet transfer method.

The transfer procedure for the deposited MoS_2 monolayer begins by blending 10 grams of cubic polystyrene (PS) pellets in a 100 mL toluene solution. The blend undergoes ultrasonication for 30 minutes and simultaneous manual stirring with a spatula until the PS pellets are fully dissolved. Subsequently, 600 µL of the resulting solution is coated onto MoS_2/SiO_2/Si for 60 s at 3000 rpm using a spin coater. The coated substrate is then heated at 80 °C in a forced air circulating oven for 40 minutes to enhance the adherence between the polymer coating and the MoS_2 layer. Moreover, to enhance water diffusion between the PS–MoS_2 layer and SiO_2/Si substrate, gentle etching of the PS film occurs along the substrate edges. PDMS is placed atop the PS film for convenient handling. Repeatedly immersing the PDMS–PS–MoS_2-coated SiO_2/Si substrate in deionized water causes the PDMS–PS–MoS_2 assembly to detach from the SiO_2/Si substrate. Using tweezers, the separated assembly is carefully lifted and placed onto the gate of MCO HEMT. To isolate the MoS_2 on gate of MCO HEMT, the PDMS film is removed by heating at 80 °C, and the PS film is removed through repeated immersion in a toluene solution. This process leaves behind a clean, crack-free layer of MoS_2 on the MCO HEMT as shown in figure 5.3(d).

5.3.4. Device Measurements and Characterization

The electrical characterization and analysis of the fabricated MCO HEMT based mercury ion sensor was conducted using the Keithley-4200 semiconductor parameter analyzer (SPA). For this analysis, the gate area was left exposed to facilitate MoS_2 functionalization and interaction with aqueous solution. For measurement, the SPA system was connected to the source and drain contacts. During the sensing analysis, a constant drain-to-source voltage (V_{DS}) of 2 V was applied throughout. Additionally, for elemental analysis X-ray photoelectron spectroscopy (XPS) has been performed using AlKα source at 1486.6 eV (ULVAC-PHI Quantra II system).

5.4. Results and discussion

To facilitate the Hg^{2+} ion detection across a range of concentrations, a 100 ppm standard solution of mercury ions was made by dissolving 2.56 mg of $Hg(NO_3)_2{\cdot}H_2O$ in 15 mL of PBS solution. Throughout the measurement process, the pH of ion solution was maintained at a constant level of 7. To get lower concentrations of Hg, standard solution was diluted according to the equation $M_1V_1= M_2V_2$, in this formula, M_1 represents the concentration and V_1 represents the volume of the standard solution, whereas V_2 and M_2 specify the final volume and concentration of the diluted solution. Using this equation, solutions with various concentrations of Hg^{2+} ions spanning from 1 part per trillion (ppt) to 10 ppm were prepared for sensing performance analysis.

Figure 5.4(a) illustrates the change in drain to source current (I_{DS}) when the MoS_2 functionalized gate region of the device is immerged in a solution without metal ions and in a 10 ppb Hg^{2+} ion solution. The drain-source voltage (V_{DS}) varies from 0 to 3V and I_{DS} was measured for both the 10 ppb Hg^{2+} ion solution the and blank solution interacting with the gate region of MCO HEMT functionalized with MoS_2. This illustrates the decrease in I_{DS} resulting from the effect of Hg^{2+} ions on the functionalized MCO HEMT gate area.

The selectivity of the MCO HEMT functionalized by MoS_2 sensor is assessed by observing its response to solutions containing Hg^{2+} ions and other HMIs. The corresponding I_{DS} changes are recorded for various HMIs at 10 ppb, as well as for a PBS solution, as illustrated in figure 5.4(b). The response of MCO HEMT sensor is observed for each over 60 s by measuring the variation in I_{DS} at a constant V_{DS} of +2 V. The current showed minimal variation for different HMIs, except for Hg^{2+} ions. A notable decrease in current was observed when the sensor's functionalized region interacted with a 10 ppb Hg^{2+} ion solution, as depicted in figure 5.4(b).

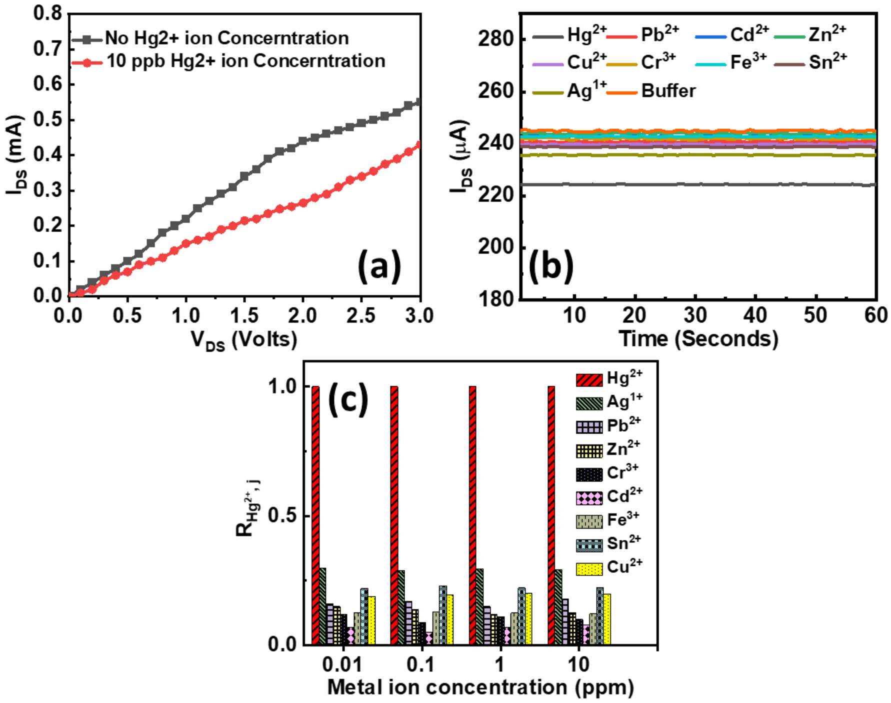

Figure 5.4: *(a) I_{DS}-V_{DS} characteristics of MCO HEMT sensor subjected to a 10-ppb Hg^{2+} ion concentration and to Hg^{2+} free water, respectively. (b) Sensing response of the device for different heavy metal ions. (c) Response ratio of the sensor for Hg^{2+} ions and other interfering HMIs for selectivity assessment.*

Further, separate solution method has been employed to evaluate the selectivity of MCO HEMT based sensor for Hg^{2+} and other HMIs at different concentrations. In figure 5.4(c) results are displayed. In this approach, the response ratio (selectivity coefficient) $R_{Hg^{2+},\ j}$ is determined by equation (1) [37].

$$R_{Hg^{2+},j} = \frac{(|I_b - I_j|)C_{Hg^{2+}}}{(|I_b - I_{Hg^{2+}}|)C_j} \ldots\ldots\ldots\ldots\ldots (1)$$

Here, I_b represents the response current when the MoS_2 functionalized MCO HEMT is immersed in a PBS solution, I_j represents the current corresponding to meddling ions at a concentration of C_j, and $I_{Hg^{2+}}$ denotes the current at concentration of $C_{Hg^{2+}}$.

The sensing responses to Hg^{2+} ions and interfering HMIs are assessed at different concentrations of 10 ppm, 1 ppm, 100 ppb and 10 ppb. The response ratios are depicted in figure 5.4(c) based on equation (1). A lower $R_{Hg^{2+},j}$ value signifies greater selectivity and reduced interfering from other HMIs. The strong interaction between Hg^{2+} and S^{2-} ions are the primary cause of the high selectivity for Hg^{2+} ions, as seen by figure 5.4(c). There is little interference detected from Pb^{2+} ions and Cu^{2+} ions.

The MoS_2 functionalized gate surface was exposed to varying concentrations of mercury ions, spanning from 1 ppt to 100 ppm, to assess real-time responsiveness of the proposed MCO HEMT based sensor. Figure 5.5(a) shows the real-time sensing response of Hg^{2+} ions, where solution of each concentration is exposed for 60 seconds. The distinct level of I_{DS} for each Hg^{2+} ion concentration indicates the efficient detection of Hg^{2+} ions. Interestingly, I_{DS} initially increased as the Hg^{2+} ion concentration rose from buffer to 10 ppt but began to decrease when the concentration exceeded 100 ppt, continuing up to 10 ppm. Figure 5.5(b) illustrates the sensor device in which the solutions interact with the MoS_2 sensing layer. The initial rise in drain current can be attributed to transfer of electrons from MoS_2 to mercury ions (Hg^{2+}) as a result of chemical adsorption. Because Hg^{2+} ions have strong affinity for sulfur, they are adsorbed onto the active sites of the MoS_2 surface, creating Hg–S complexes. Mercury ions (Hg^{2+}) bind to the MoS_2 surface until all available sites are occupied. During this process, the sulfur atoms in MoS_2 donate electrons to reduce the mercury ions, forming a Hg-S complex, this results from the strong oxidizing properties of Hg^{2+} ions and sulfur acting as a natural reducer [38, 39] as depicted in figure 5.5(c). This process reduces the negative surface charge, thereby increasing V_G, which leads to the initial increase in I_{DS}, as explained by the following equation:

$$I_{DS} = \frac{\varepsilon_n \mu W}{2dL}[2(V_G - V_T)V_{DS} - V_{DS}^2] \text{ ----------- } (2)$$

where ε_n is the MgZnO barrier layer permittivity. μ is the mobility of electrons in the 2DEG channel, L is length and W is width of the gate, respectively, the distance, denoted by d, between the device's surface and the 2DEG and V_T is the threshold voltage. Here, parameters ε_n, d, V_T, W, and L are constant.

When exposed to higher Hg^{2+} ion concentration, the remaining binding sites of the top layer gets occupied by Hg^{2+} ions, potentially forming a second layer. This can be explained by the n-type behavior of MoS_2 and retention of negative charge owing to the presence of high amount of sulfur, it results in further Hg^{2+} ion adsorption through electrostatic interactions, as shown in figure 5.5(d). These electrostatic interactions draw additional negative charges toward the MoS_2 surface. Negative charges build up proportionately on MoS_2 surface when additional Hg^{2+} ions are added, lowering the gate potential and, in turn, the I_{DS}. Studies have indicated that the MoS_2 layer maintains a negative charge during the sensing process, which changes based on the amount of mercury ions present [40, 41].

The electronic transport capabilities and high surface-to-volume ratio of MoS_2 layer in addition to the significant affinity of Hg^{2+} ions for sulfur ions in it, are responsible for electrostatic interaction enhancement at gate terminal. Which accelerates Hg-S complex formation. Consequently, the MoS_2 functionalized MCO HEMT offers a rapid response for detecting Hg^{2+} ions in water.

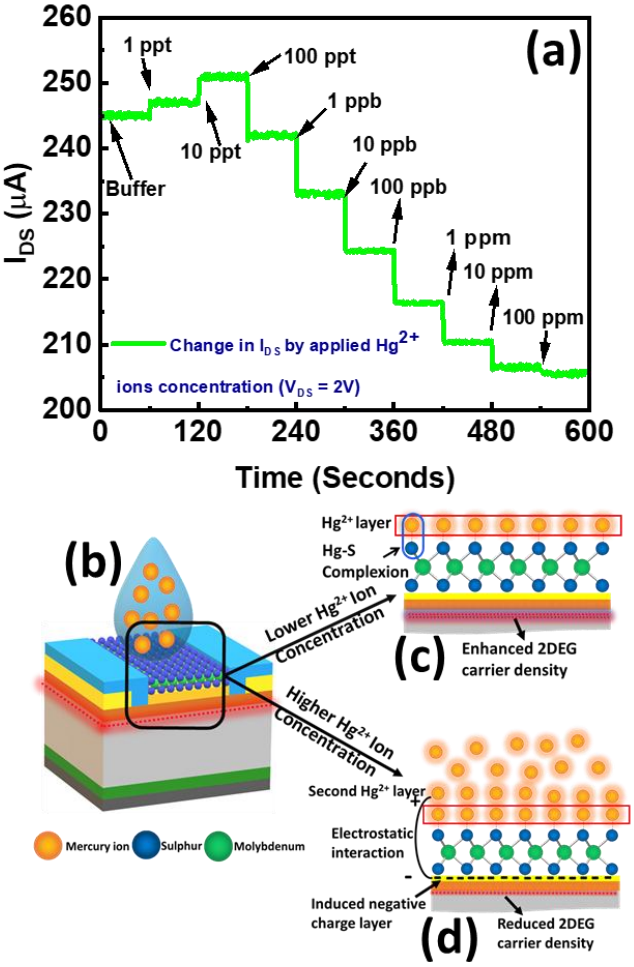

Figure 5.5: *(a) Real-time Hg^{2+} ion sensing. Sensing mechanism of MoS_2 functionalized MCO HEMT for Hg^{2+} ion detection (b) MoS_2 functionalized MCO HEMT (c) At lower concentration of Hg^{2+} ions, Hg-S complex formation at gate (d) Hg^{2+} ion-MoS_2 layer electrostatic interaction at high Hg^{2+} ion concentration.*

Further, to confirm the absorption of Hg^{2+} ions on the gate of MCO HEMT the X-ray photoelectron spectrometer (XPS) analysis has been performed before and after exposing the MoS_2 functionalized gate region to solution containing Hg^{2+} ions. The XPS spectra of Mo in MoS_2 have deconvoluted peaks of Mo $3d_{5/2}$ and Mo $3d_{3/2}$ at 229.68 and 232.88 eV, respectively, which are shifted to 229.48 and 232.68 when exposed to Hg^{2+} as depicted in the figure 5.6(a, b). The high-resolution spectrum of S before exposure to Hg^{2+} solutions is shown in figure

5.6(c) have deconvoluted peaks at 161.38 and 162.48 eV which are corresponding to the S 2p$_{3/2}$ and S 2p$_{1/2}$ components, respectively, while after exposure to Hg^{2+} ion solution the peaks are shifted at higher binding energies (BE) at162.58 and 163.68 eV as shown in figure 5.6(d).

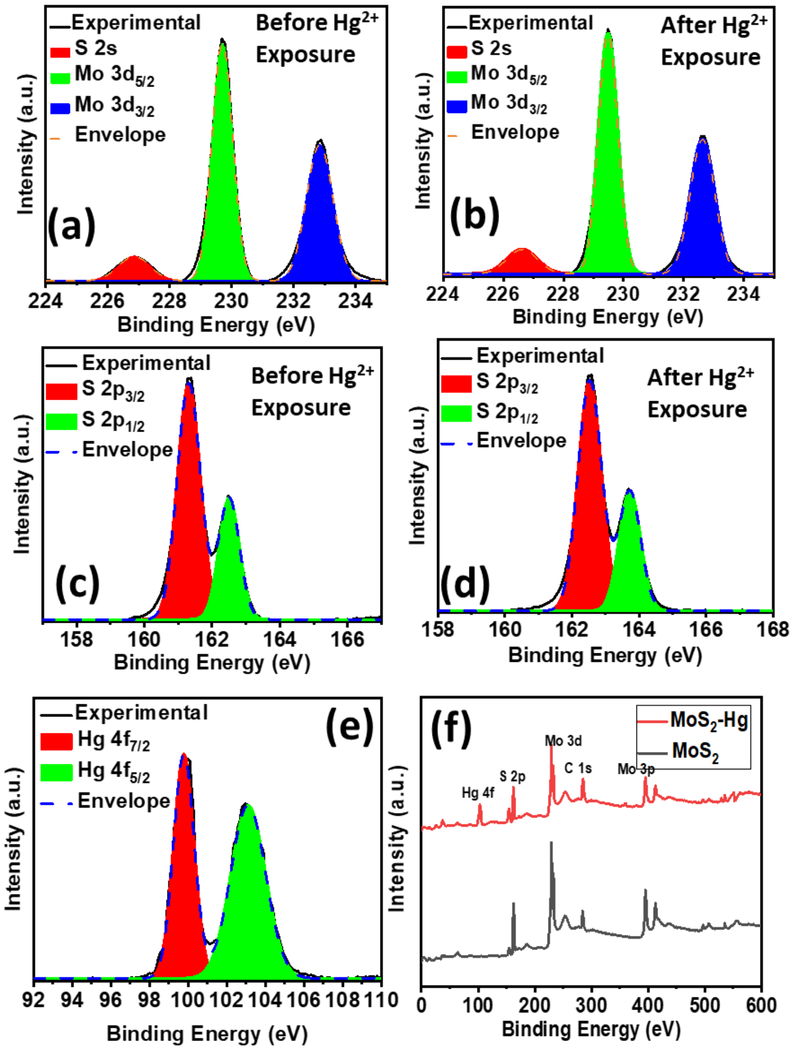

Figure 5.6: *Deconvoluted Mo 3d peaks of* MoS_2 *(a) before* Hg^{2+} *ion exposure, (b) After* Hg^{2+} *ion exposure. Deconvoluted S 2p peaks (c) before* Hg^{2+} *ion exposure, (d) After* Hg^{2+} *ion exposure. (e) Hg 4f in* MoS_2*–Hg. (f) XPS survey spectrum of* MoS_2 *before adsorption and after* Hg^{2+} *adsorption.*

Elevated BE levels indicate a higher oxidation number of sulfur species [26], the peaks above 163.2 eV corresponds to S^0 while peaks below 163.2 eV attributed to S^{2-} , so the peak of S 2p at 163.68 eV in MoS_2-Hg is therefore ascribed to the presence of S^0 species. [26, 42].

These findings indicate that sulfur in MoS_2-Hg has a higher oxidation state than in MoS_2. The presence of Hg^0 is also indicated by the distinctive Hg 4f peaks in the MoS_2-Hg spectra, which are located at 103.1 and 99.78 eV as shown in figure 5.6(e) and correspond to the Hg $4f_{5/2}$ and $4f_{7/2}$, respectively [43]. The peaks of S, Hg, and Mo are shown in figure 5.6(f). The Hg peak corresponding to Hg 4f, which is absent from the MoS_2 spectra prior to exposure to the Hg^{2+} ion solution confirms the absorption of Hg^{2+} ions.

The sensitivity and detection limit (LoD), are determined by analyzing the relationship between current (I) and Hg^{2+} ion concentration, as shown in figure 5.7(a). Equation (3) is employed for the standard 3-sigma method, which is used to calculate the LoD [37]:

$$LoD = \frac{3\sigma}{m} \ldots\ldots\ldots\ldots\ldots\ldots\ldots (3)$$

Sensitivity (m) of the fabricated MCO HEMT based sensor is computed as the slope of the calibration curve, which is determined to be 9.55 μA/ppb.

The σ (standard deviation) and the coefficient of linear regression, are extracted from figure 5.7(a) as 0.02078 and 0.9998, respectively. Consequently, the detection limit is calculated as 6.52 ppt by using equation 3. The LoD of the sensor is lower than the WHO guidelines for Hg^{2+} ions in drinkable water. The 10% and 90% I_{DS} decrements were recorded at 300.41 and 304.17 seconds, respectively, according to computation of the response time at a 10-ppb concentration. As a result, the sensor response time at a concentration of 10 ppb is calculated to 3.76 (~4) s. Furthermore, When the sensor is exposed to mercury ions, these ions bond strongly with the surface of the MoS_2. This makes it difficult to remove the mercury ions from the surface, which requires a higher activation energy to detach mercury ions from the sensor surface [26]. To achieve this, the sensor is dipped in heated PBS at 150 °C for 90 s to facilitate recovery from the bound Hg^{2+} ions. Remarkably, the recovery rate reaches as high as 99.25% during this process.

The repeatability of the sensor is demonstrated in figure 5.7(b), where the MCO HEMT based sensor consistently produced the same response under identical conditions. Furthermore, the reproducibility of the sensor was verified by fabricating a 2nd device and conducting sensing tests in similar environment, as shown in figure 5.7(c). The small difference in response between two devices may be due to variations in their internal resistance [16]. These results confirm that the sensor is highly reproducible.

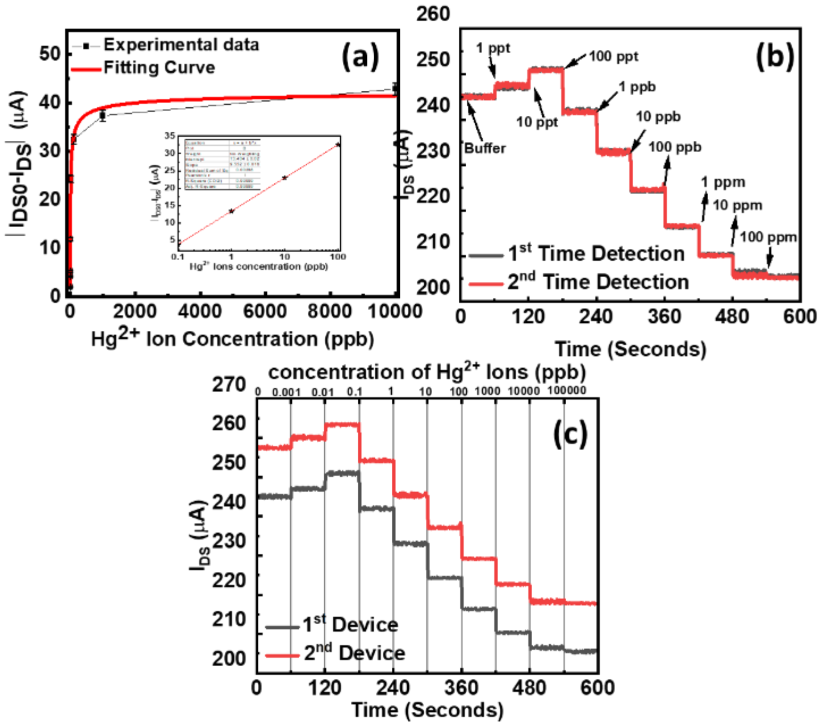

Figure 5.7: *(a) Calibration curve for* Hg^{2+} *ion sensing. (b) Repeatability, and (c) Reproducibility, of* Hg^{2+} *sensor.*

The proposed MCO HEMT based sensor functionalized with MoS_2 is compared with the existing Hg^{2+} ion sensors. The results of this comparison are presented in Table 5.2. The comparison focuses on metrics such as sensitivity, LoD, and response time. It was found that the MCO HEMT based sensor exhibited superior LoD, good sensitivity, and faster response time compared to previously reported Hg^{2+} ion sensors.

***Table 5.2:** Performance comparison of Hg^{2+} ion sensors.*

S. No.	Functionalized Material	Process	Sensitivity (µA/ppb)	LoD (ppb)	Response time	Ref.
1.	rGO/TGA-AuNP	ISFET	0.3	5	< 10 s	[44]
2.	Glucose-AgNP	LSPR on Fibre	-----	2	-----	[45]
3.	Au-nanoparticles	Colorimetry	-----	3.4	-----	[46]
4.	L-cysteine	Electrochemical	0.2031	0.995	---	[47]
5.	TGA/Au	AlGaN/GaN HEMT	-----	27; 3	5 s; 15-20 s	[48, 49]
6.	AgNW/MoS_2 nanocomposite	AlGaN/GaN HEMT	1640	0.058	-----	[50]
7.	MoS_2 nanosheets	Colorimetry	-----	100.25	-----	[51]
8.	MoS_2-Au	Colorimetry	-----	1.005	-----	[52]
9.	**MoS_2**	**Electrochemical**	**957**	**0.0279**	**< 4 s**	**Our work**

Glossary: LSPR- localized surface plasmon resonance, TGA-Thioglycolic acid

5.5. Conclusion

In this chapter, first the TCAD simulation of oxide HEMT has been carried out, the MCO HEMT has high performance as compared to MZO and MZO HEMT with MgO layer because of high 2DEG density of MCO HEMT. Further, the MgZnO/CdZnO HEMT has been fabricated via optical lithography and DIBS system. Then the synthesized MoS_2 via CVD is transferred over gate region of MgZnO/CdZnO HEMT via the surface energy-assisted wet transfer method to functionalized the HEMT for heavy metal ion sensing. The electrical response demonstrates the selectivity of the MoS_2 based MCO HEMT sensor toward the Hg^{2+} ions across the entire test range. Notably, the MCO HEMT sensor exhibited a rapid response time of less than 4 s and an exceptional detection limit of 6.5 ppt. The development of the Hg-S complex as a result of interactions among the S^{2-} of MoS_2 at lower concentrations of Hg^{2+} ions and the electrostatic interaction among MoS_2 and Hg^{2+} ions at higher concentrations of Hg^{2+} ions were the potential causes of the exceptional sensitivity. Moreover, the proposed device demonstrated high sensitivity of 9.55 µA/ppb and a recovery rate of 99.36 %, making it highly reusable and robust solution for detecting Hg^{2+} ions in water. Overall, The MCO HEMT based sensor have remarkable performance which renders it a plausible contender for real-world implementations in environmental quality surveillance and waterborne toxic metal identification.

5.6. References

[1] Renzoni, F. Zino, E. Franchi, “Mercury Levels along the Food Chain and Risk for Exposed Populations”, Environmental Research, vol. 77, no. 2, pp. 68-72, 1998.

[2] J. M. Llobet, G. Falcó, C. Casas, A. Teixidó, and J. L. Domingo, “Concentrations of Arsenic, Cadmium, Mercury, and Lead in Common Foods and Estimated Daily Intake by Children, Adolescents, Adults, and Seniors of Catalonia, Spain”, J. Agric. Food Chem., vol. 51, no. 3, pp. 838–842, 2003.

[3] M. B. Gumpu, S. Sethuraman, U. M. Krishnan, and J. B. B. Rayappan, “A review on detection of heavy metal ions in water—An electrochemical approach,” Sens. Actuators B, Chem., vol. 213, pp. 515–533, Jul. 2015.

[4] J. Mutter, J. Naumann, R. Schneider, H. Walach, and B. Haley,” Mercury and autism: Accelerating Evidence?” Neuroendocrinol. Lett., Vol. 26, pp. 439, 2005.

[5] Wei Zheng, Michael Aschner, Jean-Francois Ghersi-Egea, “Brain barrier systems: a new frontier in metal neurotoxicological research,” Toxicology and Applied Pharmacology, Vol. 192, no. 1, pp. 1-11, 2003.

[6] I. Hoyle, R.D. Handy, “Dose-dependent inorganic mercury absorption by isolated perfused intestine of rainbow trout, Oncorhynchus mykiss, involves both amiloride-sensitive and energy-dependent pathways,” Aquatic Toxicology, Vol. 72, no. 1–2, pp. 147-159, 2005.

[7] M. Aschner and S. J. Walker, “The neuropathogenesis of mercury toxicity,” Mol. Psychiatry, vol. 7, no. S2, pp. S40–S41, Aug. 2002.

[8] R. Beauvais-Flück, V. I. Slaveykova, and C. Cosio, “Cellular toxicity pathways of inorganic and methyl mercury in the green microalga chlamydomonas reinhardtii,” Sci. Rep., vol. 7, no. 1, p. 8034, Dec. 2017.

[9] Y. Cho, S. S. Lee, and J. H. Jung, “Recyclable fluorimetric and colorimetric mercury-specific sensor using porphyrin-functionalized Au@SiO2 core/shell nanoparticles,” Analyst, vol. 135, no. 7, pp. 1551–1555, 2010.

[10] S. Bettini, R. Pagano, L. Valli, and G. Giancane, “Spectroscopic investigation of the selective interaction of mercuric and cupric ions with a porphyrin active layer,” J. Phys. Chem. C, vol. 118, no. 23, pp. 12384–12390, 2014.

[11] F. Arduini, C. Majorani, A. Amine, D. Moscone, and G. Palleschi, “Hg^{2+} detection by measuring thiol groups with a highly sensitive screen-printed electrode modified with a nanostructured carbon black film,” Electrochim. Acta, vol. 56, no. 11, pp. 4209–4215, 2011.

[12] J. Gong, T. Zhou, D. Song, L. Zhang, and X. Hu, “Stripping voltammetric detection of Mercury (II) based on a bimetallic Au-Pt inorganic-organic hybrid nanocomposite modified glassy carbon electrode,” Anal. Chem., vol. 82, no. 2, pp. 567–573, 2010.

[13] S. K. Patil and D. Das, “A novel rhodamine-based optical probe for mercury (II) ion in aqueous medium: A nanomolar detection, wide pH range and real water sample application,” Spectrochim. Acta A, Mol. Biomol. Spectrosc., vol. 225, Art. no. 117504, Jan. 2020.

[14] Mehmet Oguz, Alev Gul, Ahmed Nuri Kursunlu, Mustafa Yilmaz, “A bifunctional and multi-responsive fluorescent sensor for toxic analytes in the aqueous medium: Easy synthesis, NIR-visible effect, imaging in living cells”, Journal of Molecular Liquids, vol. 336, 116861, 2015.

[15] Bilge Taner, Ahmed Nuri Kursunlu, Ersin Güler, “The example of calix[4]pyrrole derivative containing Bodipy unit: Fluorometric and colorimetric sensor for F− ion”, Spectrochimica Acta Part A: Molecular and Biomolecular Spectroscopy, vol. 118, pp. 903-907, 2014.

[16] A. Nigam et al., “Real time detection of Hg^{2+} ions using MoS_2 functionalized AlGaN/GaN high electron mobility transistor for water quality monitoring,” Sens. Actuators B, Chem., vol. 309, Art. no. 127832, Apr. 2020.

[17] M. S. Makowski, S. Kim, M. Gaillard, D. Janes, M. J. Manfra, I. Bryan, Z. Sitar, C. Arellano, J. Xie, R. Collazo, and A. Ivanisevic, “Physisorption of functionalized gold nanoparticles on AlGaN/GaN high electron mobility transistors for sensing applications,” Appl. Phys. Lett., vol. 102, no. 7, 2013, Art. no. 074102.

[18] Y.K. Verma, V. Mishra, S.K. Gupta, “A physics-based analytical model for MgZnO/ZnO HEMT,” J. Circ. Syst. Comput., vol. 29, p. 2050009, 2020.

[19] S.H. Park, D. Ahn, “Spontaneous and piezoelectric polarization effects in wurtzite ZnO/MgZnO quantum well lasers,” Appl. Phys. Lett., vol. 87, pp. 1-3, 2005.

[20] V. Pandey, A. Kumar, A. S. Razeen, A. Gupta, S. Tripathy and M. Kumar, "Pd/AlGaN/GaN HEMT-based room temperature hydrogen gas sensor," in *IEEE Sensors Journal*, doi: 10.1109/JSEN.2024.3487877.

[21] S. Bian, C. Shen,H. Hua, L. Zhou, H. Zhu, F. Xi, J. Liu, X. Dong, “One-pot synthesis of sulfur-doped graphene quantum dots as a novel fluorescent probe for highly selective and sensitive detection of lead(ii)”, RSC Adv. Vol. 6, pp. 69977−69983, 2016.

[22] B. Zhang, J. Chen, H. Zhu, T. Yang, T. Zou, M. Zhang, M. Du,“Facile and green fabrication of size-controlled AuNPs/CNFs hybrids for the highly sensitive simultaneous detection of heavy metal ions”, Electrochim. Acta, Vol. 196, pp. 422−430, 2016.

[23] A. N. Kursunlu, M. Oguz and M. Yilmaz, "On/Off Rhodamine-BODIPY-Based Fluorimetric/Colorimetric Sensor for Detection of Mercury (II) in Half-Aqueous Medium," in IEEE Sensors Journal, vol. 19, no. 6, pp. 2009-2015, 2019.

[24] Ali Bilgic, Aysel Cimen, Elif Bastug, Ahmed Nuri Kursunlu, “Fluorescent sporopollenin microcapsule modified by BODIPY for sensitive&selective recognition and efficient removal of Cu (II) from aqueous solution”, Chemical Engineering Research and Design, vol. 178, pp. 61-72, 2022.

[25] F.K. Perkins, A. L. Friedman, E. Cobas, P. M. Campbell, G. G. Jernigan, B. T. Jonker, “Chemical Vapor Sensing with Monolayer MoS_2” Nano Lett., Vol. 13, pp. 668– 673, 2013.

[26] H. Zeng, J. Dai, W. Yao, D. Xiao, X. Cui, “Valley Polarization in MoS_2 Monolayers by Optical Pumping”, Nat. Nanotechnol., Vol. 7, pp. 490– 493, 2012.

[27] K. F. Mak, C. Lee, J. Hone, J. Shan, T.F. Heinz, "Atomically Thin MoS_2: A New Direct-Gap Semiconductor" Phys. Rev. Lett, Vol. 105, pp. 136805, 2010.

[28] D. J. Late, Y. K. Huang, B. Liu, J. Acharya, S. N. Shirodkar, J. Luo, A. Yan, D. Charles, U. V. Waghmare, V. P. Dravid, C. N. R. Rao, "Sensing Behavior of Atomically Thin-Layered MoS_2 Transistors", ACS Nano, Vol. 7, pp. 4879– 4891,2013.

[29] Q. H. Wang, K. Kalantar-Zadeh, A. Kis, J. N. Coleman, M.S. Strano, "Electronics and Optoelectronics of Two-Dimensional Transition Metal Dichalcogenides", Nat. Nanotechnol. Vol. 7, pp. 699–712, 2012.

[30] ATLAS User's Manual, Silvaco Int., Santa Clara, CA, USA, Apr. 20, 2010.

[31] M. A. Khan, P. Kumar, G. Siddharth, M. Das, and S. Mukherjee, "Analysis of drain current in polycrystalline MgZnO/ZnO and MgZnO/CdZnO HFET," IEEE Trans. Electron Devices, vol. 66, no. 12. p. 5097-5102, 2019.

[32] S.-H. Jang and S. F. Chichibu, "Structural, elastic, and polarization parameters and band structures of wurtzite ZnO and MgO," J. Appl. Phys., vol. 112, p. 073503, 2012.

[33] F. Benharrats, K. Zitouni, A. Kadri, B. Gil, "Determination of piezoelectric and spontaneous polarization fields in $Cd_xZn_{1-x}O$/ZnO quantum wells grown along the polar 〈0001〉 direction", Superlattices and Microstructures, vol. 47, p. 592-596, 2010.

[34] S. Sasa, T. Hayafuji, M. Kawasaki, K. Koike, M. Yano, and M. Inoue, "Improved stability of high-performance ZnO/ZnMgO hetero-MISFETs," IEEE Electron Device Lett., vol. 28, no. 7, p. 543–545, 2007.

[35] M. A. Khan, P. Kumar, M. Das, M. T. Htay, A. Agarwal and S. Mukherjee, "Drain Current Optimization in DIBS-Grown MgZnO/CdZnO HFET," in IEEE Transactions on Electron Devices, vol. 67, no. 6, pp. 2276-2281, June 2020.

[36] M. Yano, et al., “Polarization-induced two-dimensional electron gas at $Zn_{1-x}Mg_xO$/ZnOheterointerface,” *J. Crystal Growth*, vol. 301–302,p.353–35, 2007. DOI: 10.1063/1.3028338.

[37] S. Chaudhary et al., "Ag-Loaded WS2-Based Pb2+ Ion Detection in Water," in IEEE Sensors Journal, vol. 24, no. 3, pp. 2421-2428, 1 Feb.1, 2024.

[38] R. Aswathi, K.Y. Sandhya, “Ultrasensitive and selective electrochemical sensing of Hg(II) ions in normal and sea water using solvent exfoliated MoS_2: affinity matters”, J. Mater. Chem. A, Vol. 6 , pp. 14602-14613, 2018.

[39] F. Jia, X. Zhang, S. Song, “AFM study on the adsorption of Hg^{2+}on natural molybdenum disulfide in aqueous solutions, Physical Chemistry Chemical Physics, vol. 19, pp. 3837-3844, 2017.

[40] F. Jia, Q. Wang, J. Wu, Y. Li, S. Song, “Two-dimensional molybdenum disulfide as a superb adsorbent for removing Hg^{2+} from water,” ACS Sustain. Chem. Eng., vol. 5, pp. 7410-7419, 2017.

[41] R. G. Chaudhuria, S. Paria, “Visible light induced photocatalytic activity of sulfur doped hollow TiO_2 nanoparticles, synthesized via a novel route,” Dalton Trans., vol. 43, pp. 5526-5534, 2014.

[42] R.S.C. smart, W.M. Skinner, and A.R. Gerson, “XPS of sulphide mineral surfaces: metal-deficient, polysulphides, defects and elemental sulphur,” Surf. Interface Anal., vol. 28, pp. 101-105, 1999.

[43] L. Zhi, W. Zuo, F. Chen, and B. Wang, “3D MoS_2 Composition Aerogels as Chemosensors and Adsorbents for Colorimetric Detection and High-Capacity Adsorption of Hg^{2+},” ACS Sustainable Chemistry & Engineering, vol. 4, pp. 3398, 2016.

[44] K. Chen, et al., “Hg(II) Ion Detection Using Thermally Reduced Graphene Oxide Decorated with Functionalized Gold Nanoparticles”Anal. Chem. Vol. 84, No. 9, pp. 4057–4062, 2012.

[45] G. M. Shukla, et al., “Optimization of Plasmonic U-Shaped Optical Fiber Sensor for Mercury Ions Detection Using Glucose

Capped Silver Nanoparticles”, IEEE Sensors Journal, vol. 19, no. 9, pp. 3224-3231, 2019.

[46] N. Sidana, et al., “A Simple and Highly Selective Colorimetric Sensing of Hg^{2+} Ions Based on Anti-Aggregation of Gold Nanoparticles”, IEEE Sensors Journal, vol. 22, no. 23, pp. 22549-22556, 2022.

[47] S. Muralikrishna, et. al., “In situ reduction and functionalization of graphene oxide with l-cysteine for simultaneous electrochemical determination of cadmium(II), lead(II), copper(II), and mercury(II) ions, Anal. Methods 6 (2014) 8698–8705.

[48] K.H. Chen, et al., “Low Hg (II) ion concentration electrical detection with AlGaN/GaN high electron mobility transistors”, Sens. Actuators B Chem. 134 (2008) 386–389.

[49] H.-T. Wang, et al., “Fast electrical detection of Hg(II) ions with AlGaN⁄GaN high electron mobility transistors”, Appl. Phys. Lett. 91 (2007) 042114.

[50] N. Sharma, A. Nigam, D. Lobanov, A. Gupta, A. Novikov and M. Kumar, "Mercury (II) Ion Detection Using AgNWs-MoS_2 Nanocomposite on GaN HEMT for IoT-Enabled Smart Water Quality Analysis," in IEEE Internet of Things Journal, vol. 9, no. 16, pp. 14317-14324, 15 Aug.15, 2022.

[51] Y. Lu, et al., “Spectrophotometric determination of mercury(II) ions based on their stimulation effect on the peroxidase-like activity of molybdenum disulfide nanosheets”, Microchim. Acta, vol. 183, pp. 2481-2489, 2016.

[52] Chunmeng Ma, et al., “Colorimetric determination of Hg^{2+} in environmental water based on the Hg^{2+}-stimulated peroxidase mimetic activity of MoS_2-Au composites”, Journal of Colloid and Interface Science, vol. 537, pp. 554-561, 2019.

Chapter 6

Conclusion and Future Scope

6.1. Conclusions

The principal achievement of this thesis lies in the advancement of sensing materials and the development of heavy metal ion detector using these material on different transducers like interdigitated electrode and MgZnO/CdZnO HEMT, for environmental monitoring and sustainability. The major outcomes of thesis are outlined below:

1. A highly sensitive, selective, and fast sensor for detecting trace amounts of toxic Pb^{2+} ions was successfully developed using tungsten disulfide (WS_2)-functionalized interdigitated electrodes (IDEs). Pristine and silver (Ag)-loaded WS_2 were synthesized via a simple hydrothermal method. Comprehensive characterizations were conducted to analyze the crystal structure, surface morphology, and elemental composition of the synthesized materials. Upon exposure to a 10 ppb Pb^{2+} ion solution, pristine WS_2 nanorods demonstrated a 1.31 mA current change, with further enhancements in sensitivity observed at 1% and 2% Ag loading. However, increasing the Ag loading to 4 wt% resulted in a diminished sensing response. The developed sensor exhibited outstanding sensitivity of 819 μA/ppb and an impressive detection limit of 75 ppt, along with a rapid response time of under 5 seconds, making it highly suitable for real-time heavy metal ion detection applications.
2. This study introduces an interdigitated electrode-based sensor utilizing molybdenum disulfide (MoS_2) as the sensing layer for detecting trace amounts of toxic Hg^{2+} ions. The MoS_2 layer was synthesized via a chemical vapor deposition system and transferred onto the interdigitated device using an energy-assisted wet transfer

method. Extensive characterizations confirmed the successful synthesis and integration of MoS_2 onto the IDE device. The fabricated sensor demonstrated outstanding performance, including excellent selectivity for Hg^{2+} ions, an impressive detection limit of 27.9 ppt, exceptional sensitivity of 957 µA/ppb, and a rapid response time of under 4 seconds.

3. TCAD simulations of oxide HEMTs were conducted, revealing that the MCO HEMT outperforms MZO and MZO HEMTs with an MgO layer due to its higher 2DEG density. Following this, the MgZnO/CdZnO HEMT was fabricated using optical lithography and a dual ion beam sputtering (DIBS) system. Additionally, molybdenum disulfide (MoS_2) was synthesized via a chemical vapor deposition system and transferred onto the gate of the MgZnO/CdZnO HEMT through an energy-assisted wet transfer method, functionalizing the gate for Hg^{2+} ion detection. The resulting sensor demonstrated outstanding performance, including excellent selectivity for Hg^{2+} ions, a remarkable detection limit of 6.5 ppt, a rapid response time of under 4 seconds, and high sensitivity of 9.55 µA/ppb.

6.2. Future Scope

The research presented in this thesis provides insights for the development of heavy metal ion sensor using advanced TMD materials and MgZnO/CdZnO HEMT. However, there are still uncovered aspects that could be explored in the future. These are outlined below:

- Doping of TMD materials via Noble metals and non-metals to improve the selectivity and sensitivity.
- Functionalization of gate region of MgZnO/CdZnO HEMT with other materials for the sensing of other heavy metal ions.
- Integration of developed sensor with current readout circuit to develop a portable sensor.